EFFECT OF PORE WATER IN ROCK FORMATION ON THE BEHAVIOR OF CRYOGENIC FRACTURING

A Thesis

by

CAITLIN RENAE CARTER

Submitted to the Office of Graduate and Professional Studies of
Texas A&M University
in partial fulfillment of the requirements for the degree of

MASTER OF SCIENCE

Chair of Committee,	Minsu Cha
Committee Members,	Hisham Nasr-El-Din
	Marcelo Sanchez
Head of Department,	Efstratios N. Pistikopoulos

August 2018

Major Subject: Energy

ABSTRACT

Hydraulic fracturing has revolutionized the oil and gas industry by increasing hydrocarbon production from unconventional sources. However, waterless or reduced-water fracturing technologies have been researched due to rising concerns on the heavy use of water for hydraulic fracturing. Cryogenic fracturing is implemented by subjecting cryogenic fluid on rock formation. The idea is that a large thermal gradient, perhaps caused by evaporation of a liquified gas can induce fractures when brought into contact with a much warmer rock under downhole conditions. Rapid cooling of the rock at warm reservoir temperature will induce contraction and subsequent tensile fractures are created. Fractures created in the rocks surrounding the borehole can thus be achieved without the use of water.

Many unconventional gas formations have low water saturations, however near wellbore water saturation can be present from prior drilling and completion operations. This study investigates the effect of the presence of pore water in rock formation on the practice of cryogenic fracturing. Although we understand cryogenic fracturing can create fractures in reservoir rocks, the effect of water in the pore space of reservoir rocks has not been fully investigated. The freezing of water in formations can play a competing role with contraction of the rock, as the volume of water expands by 9% upon freezing.

This thesis reports results from a laboratory study of cryogenic fracturing in water-saturated specimens. Liquid nitrogen was utilized to create a strong thermal gradient generating local tensile stress in submersion tests and in the saturated rocks surrounding a borehole. We have developed experimental setups and procedures to conduct cryogenic fracturing tests without confining stress. Cubic blocks (8″×8″×8″) of Berea Upper Grey sandstone and concrete were

tested. Cryogen transport, measurements, and fracture characterization were integrated in experimental setups. Borehole pressure, liquid nitrogen, and temperature can be monitored during experiments. Acoustic signals were used to characterize fractures before and after the tests.

Cryogenic tests conducted on water-saturated specimens in boreholes in the absence of confining stress were able to create cracks on the outer surface of the specimens and alter rock properties. By comparing the results from the unstressed concrete and sandstone, we found the generation and geometry of fractures in water-saturated specimens is dependent on material properties such as permeability and pore distribution. The freezing of pore water in highly porous sandstones intensifies the damage done to the pore structure, to some extent, and favors the expansion of micro-fractures in the mineral skeleton to generate large fractures. Water in the formation expands as it freezes and can prevent cryogenic fracturing in strong, low-permeability reservoir rocks (concrete) by creating a barrier to nitrogen pressure permeation near the wellbore.

On the other hand, from submersion tests it is evident that weak rocks subjected to cryogenic fracturing, such as shale, can create fractures along bedding planes even though they have low permeability. This may be utilized to enhance gas recovery in shale reservoirs. Fractures were created by generating a strong thermal gradient in saturated sandstone and shale core specimens submerged in liquid nitrogen. Submersion time, cryogen amount, temperature, and fracture characterization were integrated in experiments. Acoustic signals were used to characterize fractures before and after tests. Saturated concrete blocks also fractured due to the strong thermal gradient generated by liquid nitrogen submersion.

ACKNOWLEDGEMENTS

I am sincerely grateful to my advisor, Dr. Minsu Cha, for his very generous support and guidance of my research. I would also like to express my gratitude to the other member of my thesis committee, Dr. Marcelo Sanchez, Dr. Hisham Nasr-El-Din, and Dr. Sam Noynaert who all provided excellent feedback on my research direction.

I would like to extend my sincere thanks and appreciation to the Head of Energy Department, Dr. Efstratios Pistikopoulos, and academic advisors Dr. Valentini Pappa and Mr. Jeff Sammons. Their constant support and invaluable advice throughout the Energy program was always positive and inspiring.

A special thank you goes to Joevan Beladi in the Harold Vance Petroleum Engineering Department for coring our specimens. Also, to Breanna Brocklesby, Staci Jessen, Anne-Marie Ginn and Don Conlee Jr. for assisting with CT-imaging of our specimens at the Harold Vance Petroleum Engineering Department and the Texas A&M Veterinary Medicine and Biomedical Sciences Department.

Furthermore, I would like to specially thank PhD. student Jungyeon Jang in Texas A&M Civil Engineering Department for his timely help and guidance in the lab. Finally, I could not have accomplished this program without my friends and family's continual support throughout my time here at Texas A&M. To all of them, I am extremely grateful.

CONTRIBUTORS AND FUNDING SOURCES

This work was supported by a dissertation committee consisting of Professor Minsu Cha [advisor] and Professor Marcelo Sanchez of the Department of Civil Engineering, and Professor Hisham Nasr-El-Din of the Department of Petroleum Engineering. Experimental materials and devices were supported by the Texas A&M Energy Institute and Dr. Cha's start-up funding from the Zachry Department of Civil Engineering. All work for the dissertation was completed independently by the student.

NOMENCLATURE

LN	Liquid nitrogen
SEM	Scanning Electron Microscopy
CT	X-ray computed tomography
Micro-CT	X-ray computed microtomography
TC	T-type thermocouples
P-wave	Compressional/primary acoustic wave
S-wave	Shear/secondary acoustic wave
MICP	Mercury intrusion porosimetry
XRD	X-ray diffraction
CTE	Coefficient of thermal expansion

TABLE OF CONTENTS

Page

LIST OF FIGURES

Page

LIST OF TABLES

Page

LIST OF EQUATIONS

Page

CHAPTER I

INTRODUCTION

Hydraulic fracturing, or the popular term “fracking”, of oil and gas reservoirs has enhanced hydrocarbon production in unconventional plays. In traditional fracking, a high-pressure fluid, typically water with chemical additives, is injected from a well to a target formation to create open fractures (Norris et al. 2016). The fractures are held open by proppants, usually sand, that are mixed into the high-pressure slickwater, to allow oil or gas to migrate back to the well for production. Modern fracking includes horizontal drilling for developing shale and tight reservoirs. This technique allows the well to produce over a larger area, however, it uses approximately 100 times as much water than a traditional fracking injection (Montgomery 2013). The increase in modern fracking in Texas has intensified discussion regarding water supply and usage, especially in arid regions. As an example, a typical well in the Eagle Ford play requires a median of 3.61×10^6 gallons of water for production (Kondash and Vengosh 2015). This is enough water to fill more than five Olympic sized swimming pools.

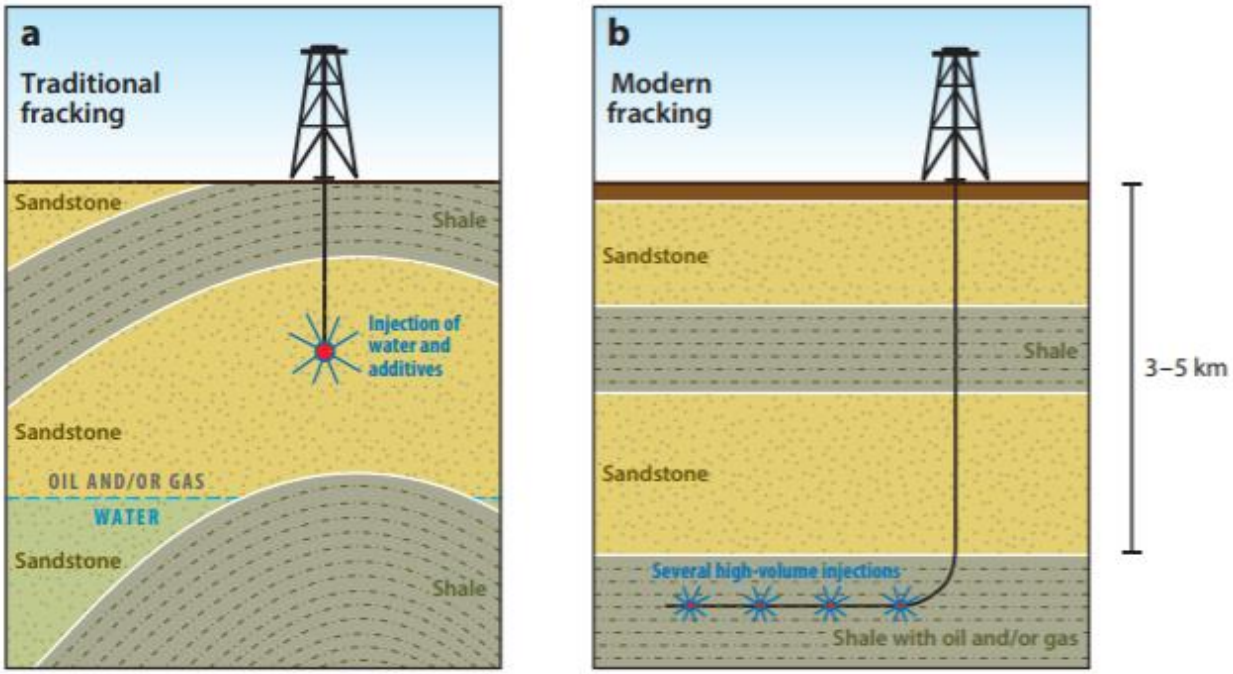

Figure 1: (a) Traditional fracking. (b) Modern (high-volume) fracking using directional drilling. Reprinted from Norris et al. 2016.

Besides water usage in massive quantities, there are other shortcomings with fracking as well. Clay-rich shale formations have the potential to absorb water and swell. This can have negative effects on fracking, as the fractures will narrow, and pore size will shrink (Cha et al. 2016). The capillary retention of water in pores has the possibility to impair the relative permeability of the shale, decreasing the production of hydrocarbons and the recovery efficiency. The toxicity of the chemical additives in the high-pressure injection fluids are also concerning to public health and the environment. After injection has ceased, only 20% to 40% of the injected water returns to the surface (Norris et al. 2016). The unrecovered water is typically undesirable because of formation damage and capillary retention, which decreases permeability. The water recovered is transported to storage ponds or reinjected into wastewater wells. This water left behind at the original well or reinjected at a new wastewater well has the potential to contaminate

shallow aquifers; storage ponds have the potential to leak and/or spill to contaminate surface water (Mrdjen and Lee 2016). In contrast with hydraulic fracturing, cryogenic fracturing using liquid nitrogen (LN) has the potential to offer fracturing capabilities without benefiting to any of these water-related concerns (Cha et al. 2016). Moreover, liquid nitrogen can be made on site in the field and injected into the formation directly using a specialized device, eliminating the need for transportation of fracturing fluids (Li et al. 2016).

1.1 Literature Review

Cryogenic fracturing is a relatively new method for a waterless, unconventional reservoir stimulation technology that is meant to supplement hydraulic fracturing practices. The concept rests on the idea that fractures can be created by a sharp thermal gradient (thermal shock) of an extremely cold liquid contacting a warm rock formation under downhole conditions (Grundmann et al. 1998). The thermal shock will cause the surface of the rock to contract due to the tensile stress. The contraction creates fractures orthogonal to the contact surface of the cryogenic fluid and the rock when the stress reaches the tensile strength of the rock.

McDaniel et al. (1997) researched cryogenic fluids in coal beds and found that the physical alteration of the fracture walls using liquid nitrogen prevented closure of thermally induced fractures. Therefore, it is understood that if the rock formation undergoes sufficient breakage into rubblized pieces at the cryogen contact surface, the formation will not have the ability to close the fracture. This could keep the fractures propped open against in-situ compressive stresses after injection of liquid nitrogen is ceased, eliminating the need for proppants in this fracking technique. However, if this mechanism does not work, the use of traditional or ultra-light weight proppants can fill the gap.

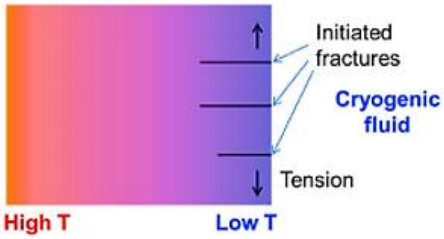

Figure 2: Basic concept of cryogenic fracturing.

Cryogen takes a liquid form at low temperatures and is transformed into the gaseous phase at standard temperature and pressure conditions. When the liquid nitrogen is put into contact with warm rock, the heat from the rock will transfer to the liquid nitrogen at boiling point (-195.8°C or -320.4°F) (Cha et al. 2016). This will result in the rapid cooling of the rock surface, which will cause it to contract and fracture orthogonal to the surface. The resulting fractures may be further induced by high pressure gas from LN vaporization (Cha et al. 2016). Past laboratory studies of liquid nitrogen fracturing by McDaniel et al. (1997) proved that immersing coal samples in LN would result in significant shrinkage and breaking of the coal into smaller cubic fragments. Immersing the fragments in more liquid nitrogen would result in further shrinking and cause the fragments to break up into smaller pieces. McDaniel et al. (1997) and Grundmann et al. (1998) performed field experiments of liquid nitrogen stimulation in coalbed methane and sandstone formations, and in Devonian shale formations, respectively. The treated wells were completed with steel casing. Fiberglass tubing protected the casing from thermal shock damage. Formations were shot with perforations to allow liquid nitrogen to contact the rock. McDaniel's results showed that three coalbed methane wells increased in production, one had no change in production, and one low permeability sandstone well, initially completed with slickwater fracturing, decreased in production rate. Grundmann's field stimulations resulted in an incremental production rate of 8%

in the Devonian shale bed. The increased production rates in these experiments displays the positive results of cryogenic fracturing using LN. Cha et al. (2014) conducted submersion tests and applied cryogen to boreholes in unconfined specimens to better understand the material behaviors with LN. The application of LN to boreholes in the center of concrete and sandstone specimens led to enhanced fractures by creating new cracks and widening existing cracks. Cha et al. (2016) investigated the effect of cryogenic stimulation on rock fracturing under true triaxial confining stresses (wellbore conditions). The specimens tested included concrete, sandstone and shale blocks. The treated specimens resulted in fractures clearly being generated by LN flow through a borehole under both low and high flow pressure, which increased the permeability of the specimens. Breakdown pressures were also significantly lowered by cryogenic stimulation. Although fractures were initiated by the cryogenic stimulations, Cha et al. (2016) concluded that borehole pressurization may be needed to induce further fracture penetration.

Liquid nitrogen has a liquid to gas expansion ratio of 1:694 at 20 °C. LN interaction causes tensile stress to occur on solid rock. When water becomes ice, the volume increases by approximately 9% (Cha et al. 2014); water in rock pores will expand when frozen. When dealing with rock samples that are saturated with water undergoing cryogenic fracturing, there is a conflicting effect of compressive vs. expansive stress. This complicates the result. There have been studies done on the effects of cryogenic fracturing on rock specimens, but the interaction between water in the rock and the cryogen have not been fully investigated.

Cha et al. (2014) performed a water-saturated block submersion test in LN using a concrete sample (8″×8″×8″) that had a water to cement ratio of 0.55, and a sand to cement ratio of 2.5. The outer layer of the sample expanded laterally, which resulted in shear fractures parallel to the tested surfaces. The ice expanded against the mineral matrix (in this case, sand and cement). However,

there were no obvious cracks formed from rock contraction, which would have formed away from and perpendicular to the edges of the sample. Cha et al. (2014) determined the overall volume change (%) of the sample to be 1.2% expansion. His research concluded that the presence of water can weaken the driving force of cryogenically induced tensile fractures; it may also lead to wellbore failure and stability issues. This has implications in the effectiveness of cryogenic fracturing for enhanced oil recovery techniques. If cryogenic fracturing is performed at formations that are water saturated, or at formations that have been exposed to previous water-based drilling and completion fluids, the integrity of the cracks will be questioned. Rocks exposed to LN that contain water in its pores will freeze and expand, damaging the pore structure.

Rocks, as porous media, contain fluids inside them. When the temperature of the rock drops below the water-freezing point, the fluid in its pores is frozen and expands. According to Chen, Yeung et al. (2004), under low thermal gradient rocks can be frozen and damaged in the following three ways: (i) the pore water freezes, expands, and causes large compressive stress; (ii) the ice lens formed by the pore water causes the rock to crack; and (iii) the unfrozen water is squeezed by ice causing additional pore pressure on the rocks.

Porous materials that contain water and experience freezing temperatures will begin to form ice lenses. Migration of water in the porous materials allows ice lens growth, leading to the persistent growth of a crystal large enough to disrupt rocks (Rempel 2007). The velocity of the freezing front effects the formation of ice lenses. When the freezing rate is high, ice lenses can be nucleated but they cannot grow large enough to be visible, as the supply of unfrozen water is cut off by the nucleation of subsequent lenses (Saruya et al. 2014). To achieve high thermal gradient for cryogenic fracturing, a rapid cooling rate must be achieved. Therefore, the formation of ice lenses in our experiments will not be a contributing factor to fracture propagation.

The volumetric expansion of water due to phase change from liquid to ice causes additional pore pressure within the unfrozen pores. A cryogenic suction gradient is developed at the ice/water interface in response to the temperature gradient at the ice/water interface (Thomas et al. 2009). The cryogenic suction draws pore water in the unfrozen pores towards the freezing pores. This in turn raises pore pressure and may leads to fracturing of the mineral skeleton. It is important to consider this phenomenon as a factor of fracture propagation for saturated specimens subjected to cryogenic temperatures.

Further investigation of the effects of water on cryogenic fracturing should be investigated to fully understand the opportunity that it offers in the oil and gas industry.

1.2 Research Scope and Objectives

The goal of this research is to conduct cryogenic stimulation lab experiments to investigate the effects of formation water on cryogenic (thermal) fracturing. Specific objectives include:

- Be able to observe and characterize fracturing patterns in small and large-scale submersion tests. This will include the analyses of photographs, acoustic waves, and SEM and micro-CT images.
- Submersion tests of cryogenic fracturing in dry and saturated specimen were performed to compare the effects of water on fracturing geometry and thermal expansion/contraction relationship. The temperature gradient of dry and saturated concrete specimens was investigated.
- Porous and tight sandstone core specimens were tested to observe the effect of porosity on the fracturing geometry. Dry and saturated specimens were subjected to liquid nitrogen

stimulation to observe pore water effects on fracturing. The overall volume change and changes in permeability for core specimens was determined.

- Submersion tests on small-scale shale core specimens were tested to observe fracturing geometry and the effects of water presence on shale specimens. Feasibility of cryogenic fracturing for enhanced oil recovery in shale formations is discussed.
- Be able to observe and characterize fracturing patterns in unconfined water-saturated blocks with wellbore. Water-saturated concrete and sandstone blocks were subjected to liquid nitrogen under no confining stress. This will include the analyses of photographs, acoustic waves, and CT images.

CHAPTER II

LIQUID NITROGEN SUBMERSION TESTS: SANDSTONE AND SHALE CORES

When water becomes ice, its volume increases by 9%. The magnitude of which is typically significantly larger than thermal expansion or shrinkage of mineral phases (Cha et al. 2014). In the study by Cai et al. (2014), cooling of both dry and saturated rock with LN leads to fracturing and changes in the pore structure. According to Cai et al. (2014), the changes in the rock's characteristics depended on the rock type, its physical and thermal properties, and water content. Rocks with a large water content resulted in the freezing of pore water and intense damage to the pore structure. To study cryogenic fracturing in water-saturated specimens vs. dry specimens, we first investigate small-scale submersion tests. While Cai et al. (2014) analyzed their specimens using scanning electron microscopy (SEM) and nuclear magnetic resonance, we will focus on micro-CT imaging and acoustic analysis to characterize fractures.

Specimens were submerged in a container with liquid nitrogen until approximate thermal equilibrium is reached. Submersion stimulation lasted 4-5 hours until all LN evaporated. Two types of sandstone cores of different permeabilities and porosities, and Mancos shale cores have been investigated. The permeability of the sandstone specimens is measured before and after LN submersion. Fractures are characterized and the effects of water in the pore space of the natural rocks is discussed.

2.1 Experimental Methods

2.1.1 Specimens

Our specimens include Mancos shale cores and two types of sandstone cores: Bentheimer (high porosity) and Colton (low porosity). The shale and sandstone cores were obtained from Kocurek Industries in Texas. All core specimens were 3-inch-tall by 1.5-inch diameter cylinders. In the submersion tests, the core specimens were fully submerged in a Styrofoam container filled with liquid nitrogen (LN). The specimen chosen to be saturated were submerged in 5 wt. % KCl brine until saturation is achieved by weight stabilization (Figure 3). We used brine to minimize the effect of clay swelling in the sandstone and shale cores.

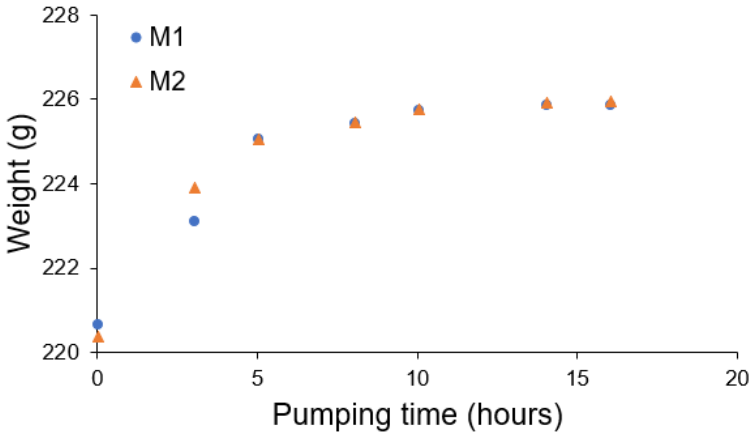

Figure 3: Weight stabilization of Mancos 1 and 2 in a vacuum chamber.

The low porosity Colton sandstone cores were named “Colton 1” for the dry specimen and “Colton 2” for the saturated specimen; shorted to “C1” and “C2” respectively. We followed the same naming for the high porosity Bentheimer sandstone cores, naming the dry specimen “Bentheimer 1” or “B1” and the saturated specimen “Bentheimer 2” or “B2”. The shale core specimens were named Mancos 1 (M1), Mancos 2 (M2), and Mancos 3 (M3). Mancos 1 and 2

were saturated and Mancos 3 was the dry specimen. Intact rock properties of all specimens are in Table 1 below.

Table 1: Mechanical properties of the intact sandstone and shale cores. All values are the average of 2-3 acoustic measurements per specimen. All measurements were taken under dry condition.

	Bentheimer 1 (dry)	Bentheimer 2 (saturated)	Colton 1 (dry)	Colton 2 (saturated)	Mancos 1 (dry)	Mancos 3 (saturated)
Average V_s [m/s]	2232	2090	2122	2169	2111	2256
Average V_p [m/s]	3270	3114	3195	3089	3906	3743
Elastic modulus [GPa]	21.58	19.21	24.17	25.96	29.25	32.37
Poisson's ratio	0.06	0.09	0.1	0.13	0.29	0.2
Shear modulus [GPa]	10.15	8.81	10.94	11.42	11.3	13.3
Constraint modulus [GPa]	21.76	19.55	24.78	27.13	38.72	36.7

2.1.2 Procedure

A dry specimen and a saturated specimen of each rock type was fully submerged in 10 liters of liquid nitrogen (Figure 4). All four of the sandstone specimens were submerged in the same Styrofoam container at one time, but specimens were moved away from each other for minimum interference. Specimens were left in the Styrofoam container and observed until all liquid nitrogen evaporated. After all LN had evaporated (~4-5 hours), specimens were observed for visible surface fractures.

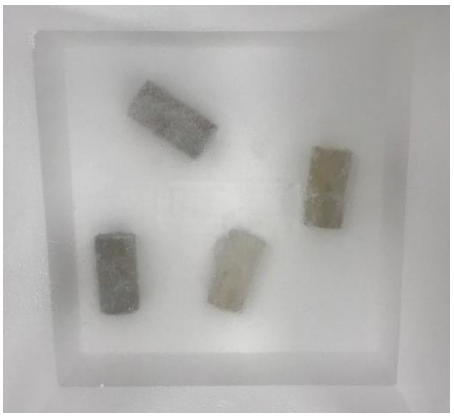

Figure 4: Submersion of sandstone cores in liquid nitrogen.

The permeability of the sandstone specimens was measured before LN submersion. Permeability was measured with a core-flood experimental setup, in which cores are initially saturated in a vacuum chamber for 4 hours with 5 wt. % KCl water (brine water) to achieve full saturation. Brine water was used to prevent swelling of clay particles in sandstone specimens, as swelling may lead to lower values of permeability and alter the properties. For the low porosity Colton specimens, the cores in the core-flood chamber are injected with brine at a flow rate of 0.2 cm^3/min until approximate steady state is reached. No backstop pressure is applied, and a confining pressure of 1500 psi is used. At steady state, the pressure drop across the core is recorded and brine saturation (permeability) is determined. For the high porosity Bentheimer specimens, the cores in the core-flood chamber are injected with brine at three different flow rates: 4, 6, and 8 cm^3/min. Given the flow rate equation, $Q = k \cdot \frac{A \cdot \Delta P}{\mu \cdot L}$ (where k is permeability [mD], A is area [m^2], ΔP is the applied pressure difference [Pa], μ is viscosity [Pa·s] and L is the length [m] of the core specimen), we let $x = \frac{A \cdot \Delta P}{\mu \cdot L}$ and graph x vs Q to find the slope of the line, k. There was no backstop pressure applied, and a confining pressure of 1500 psi was used.

Porosity was calculated by the following equations:

$$\text{Porosity } (\phi) = \frac{\text{Pore volume } (v_P)}{\text{Bulk volume } (v_B)} \quad \text{Equation 1}$$

and

$$\text{Pore volume } (v_P) = \frac{\text{saturated specimen weight - dry specimen weight}}{\gamma_{brine}} \quad \text{Equation 2}$$

where the unit weight of the brine, γ_{brine}, is assumed to be 1.0365 g/cm^3.

Table 2: Permeability test results.

	Bentheimer: Vender's measurements	Bentheimer 1	Bentheimer 2	Colton: Vender's measurements	Colton 1	Colton 2
Permeability (k)	1600-2500 mD	491 mD	430 mD	0.1-2 mD	0.033 mD	0.036 mD
Porosity (Φ)	24%	18%	19%	7-14%	8.8%	9.12%
KCl concentration	3 wt. %	5 wt. %	5 wt. %	3 wt. %	5 wt. %	5 wt. %

Our permeability values from the core-flood test had lower values than the values from Kocurek Industries' flow-perm tests, which used 3 wt. % KCl brine water and a confining pressure of 500 psi. The differences between our permeability results could be caused by the differences in the test conditions such as the level of confining pressure (1500 of our test vs 500 psi of Kocuerk's test) and KCl concentration (5 wt. % vs 3 wt. %).

Permeability measurements of the shale core specimens were not able to be obtained in our lab. These parameters for Mancos shale were investigated by Kalteyer (2017) by multiple tests, including mercury intrusion porosimetry (MICP), core plugs, and low-pressure gas physisorption; the ranges he found are in Table 3. Also found in this table is our value for porosity of the specimens, calculated by using Equation 1 on the saturated specimens.

Table 3: Porosity and permeability of Mancos shale.

	Kalteyer (2017)	Our calculations
Permeability (k)	1 to 5 μD	
Porosity (ϕ)	1-7%	6-6.43%

Table 4: Tensile strength used for the submersion tests. Reprinted from Cha et al. 2018.

	Sandstone	Shale	Concrete
Splitting tensile strength (MPa)	4.51	8.45	2.88

2.1.3 Fracture Characterization

Fracture development of all specimens are characterized using acoustic signatures and light microscopy with a Zeiss Axiophot microscope. In addition, shale and sandstone cores were imaged by micro-CT using an X-Tek Hawk CT. Bentheimer sandstone cores were also characterized using scanning electron microscopy (SEM). SEM images of the Colton sandstone and Mancos shale were attempted but the SEM chamber in the Tescan FERA-3 was not capable of degassing, due to the low porosity of the specimens.

The characteristics of acoustic waves propagating through a medium depend on the mechanical properties of the medium (Cha et al. 2009). The wave velocity in jointed rock masses is a function of the density of cracks, or joint spacing as modeled by:

$$V_s = \sqrt{\frac{G_{eq}}{\rho}} = \sqrt{\frac{1}{\rho}\left(\frac{k_S S G}{k_S S + G}\right)} \qquad \text{Equation 3}$$

where V_S is shear wave velocity, k_S is shear joint stiffness, G is shear modulus of intact part, ρ is rock mass density, and S is joint spacing. When intact rock properties, density, and joint stiffness

remain the same, the acoustic wave velocity can be used to characterize crack generation. Geomaterials allow acoustic waves to travel naturally due to inherent discontinuities such as granular discreteness and cracks. The high frequency content is filtered when acoustic waves propagate through cracked media (Cha et al. 2014). Acoustic measurements before and after tests were taken on specimens using P and S ultrasonic transducers. The differences in the acoustic signatures before and after cryogenic stimulation were then investigated, focusing on P and S wave velocities and amplitudes.

2.2 Observations and Results

2.2.1 Observations and results: Sandstone submersions

When the core specimens were placed in the liquid nitrogen, they began to rapidly boil due to the large difference in temperature. For the case of saturated specimens, liquid nitrogen boiled unevenly on their surface, compared to the more even distribution of boiling from the dry specimen, and had larger bubbles boiling off than dry specimens. Figure 5 displays a drawing of the LN bubbles formed on each specimen during LN submersion. The concentrated area of bubbles circled in red on Bentheimer 2 is a point of particularly rapid and prolonged boiling with large bubbles.

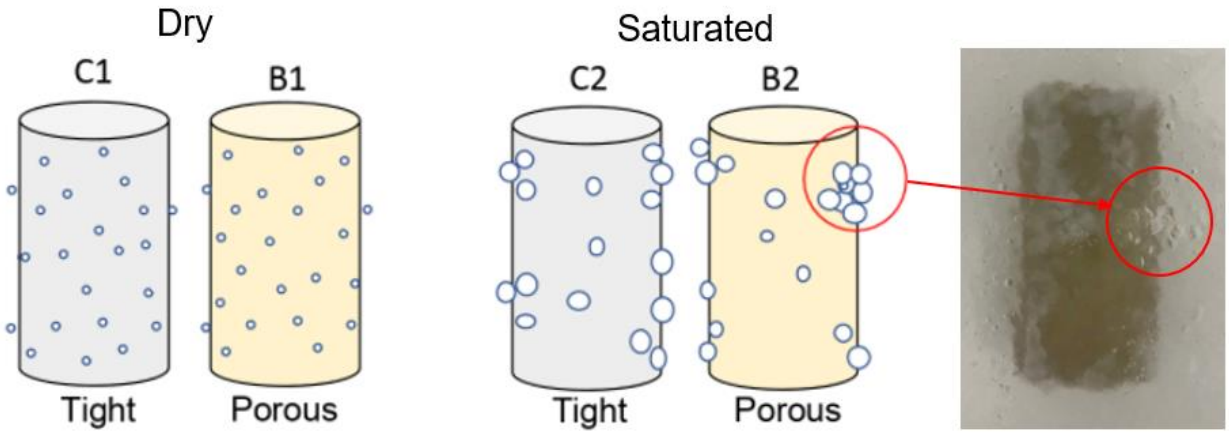

Figure 5: Liquid nitrogen boiling patterns on sandstone cores during submersion. Notice the area of concentrated boiling (red circled) and ice patch formation (whiter area on the core in the photo) on Bentheimer 2.

It was observed during liquid nitrogen submersion that the saturated specimens experienced a longer period of boiling than the dry. This observation correlates with the effective thermal diffusivity values we calculate in the discussion section, where the dry specimens have higher values and were assumed to reach thermal equilibrium quicker. However, it does not correlate with the effective thermal conductivity calculated for the specimens, where the saturated specimens had higher values.

All specimens experienced ice patches growing on their exposed surfaces when submerged, however, the saturated specimens had ice formation before the dry. After all LN had evaporated (~4-5 hours), specimens were observed for visible surface fractures. Before submersion, no specimens had any surface fractures or small cracks. Bentheimer 1 (dry) (Figure 7a) shows one visible fracture on the top of the core, but the interesting fracture that we notice is on Bentheimer 2 (saturated) (Figure 7b). B2 has a visible fracture, about 2 inches in length, circling the circumference of the core. The fracture created is located at the same area of rapid and

prolonged boiling that was circled in red in Figure 5. SEM images were not able to distinguish any micro fractures or internal fracturing in the Bentheimer specimens tested, therefore they are not included. As seen in Figure 7c. and 7d., neither Colton 1 or Colton 2 show visible surface fractures after treatment.

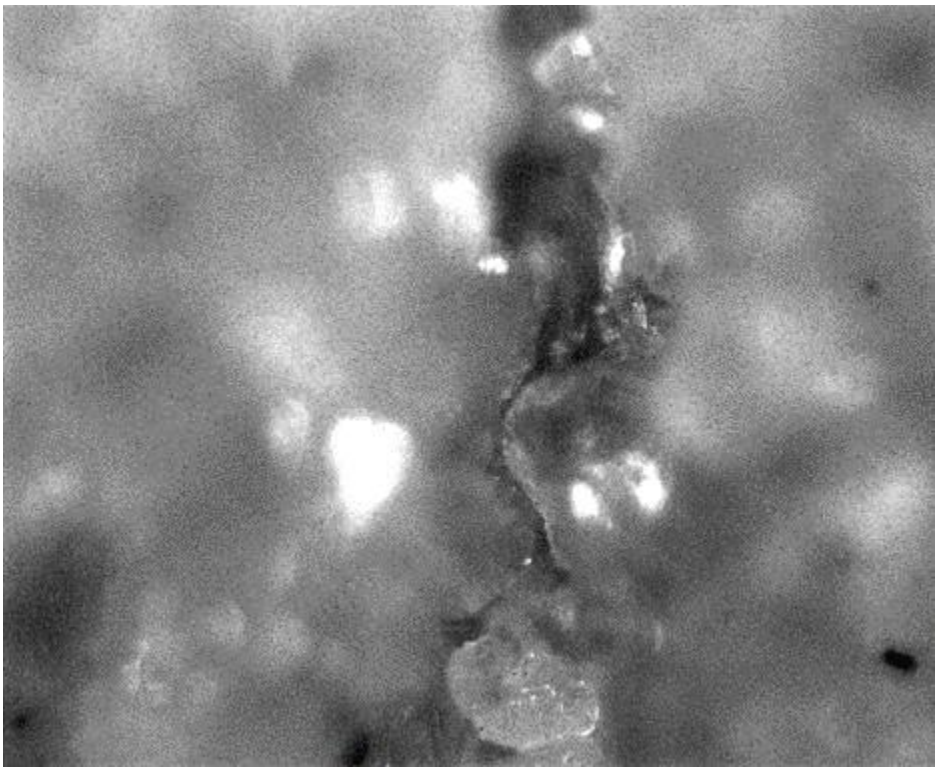

Figure 6: Light microscopy image (5×) of fracture on Bentheimer 2 (saturated).

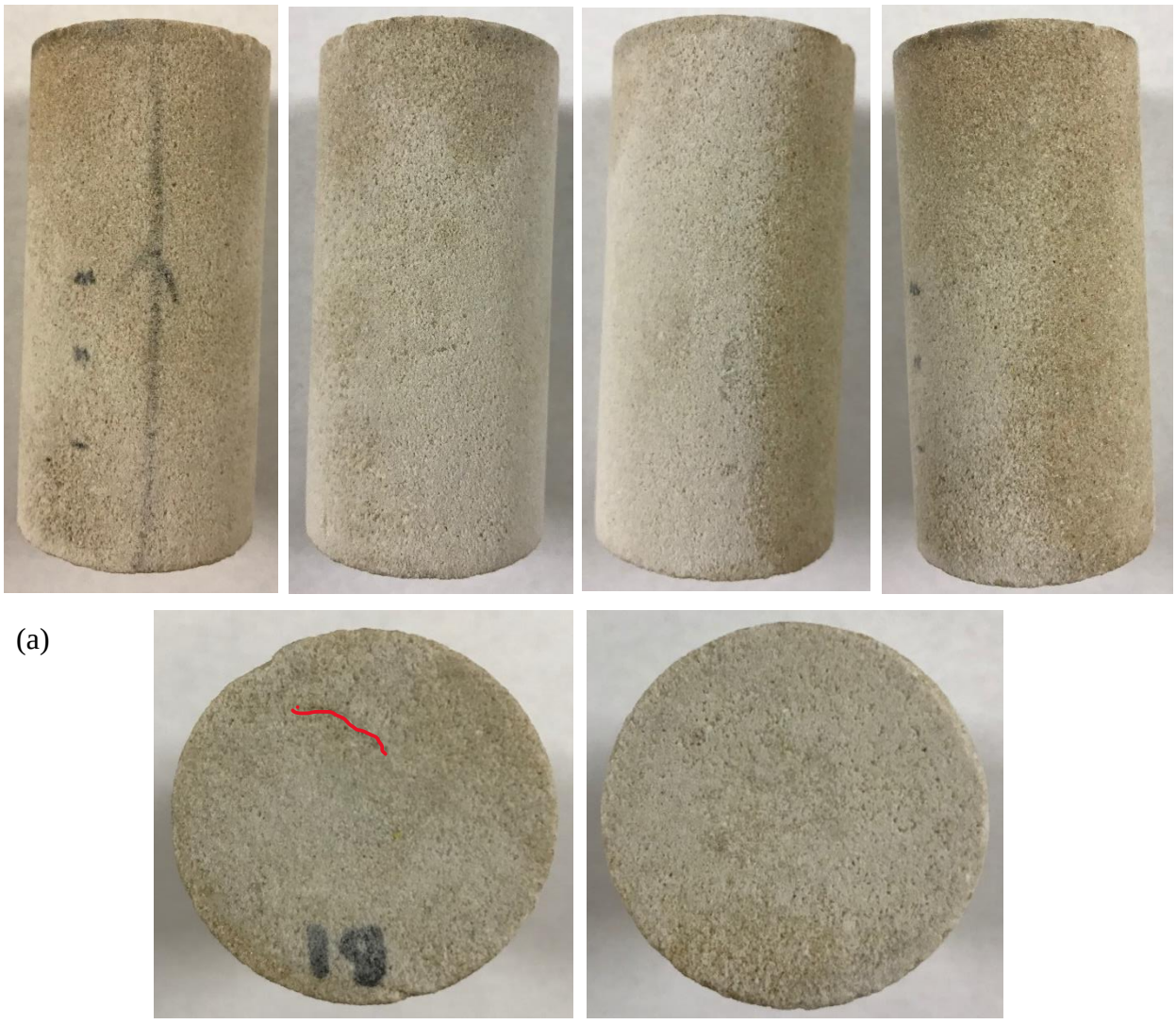

Figure 7: Sandstone cores after LN submersion test. (a) Bentheimer 1 (dry specimen). White parts on the surface are precipitated salts (KCl) during drying. (b) Bentheimer 2 (saturated specimen). Multiple fractures were seen on the surface. Red lines are superimposed on the surface for better visibility. (c) Colton 1 (dry specimen). No visible surface fractures. (d) Colton 2 (saturated specimen). No visible surface fractures.

(b)

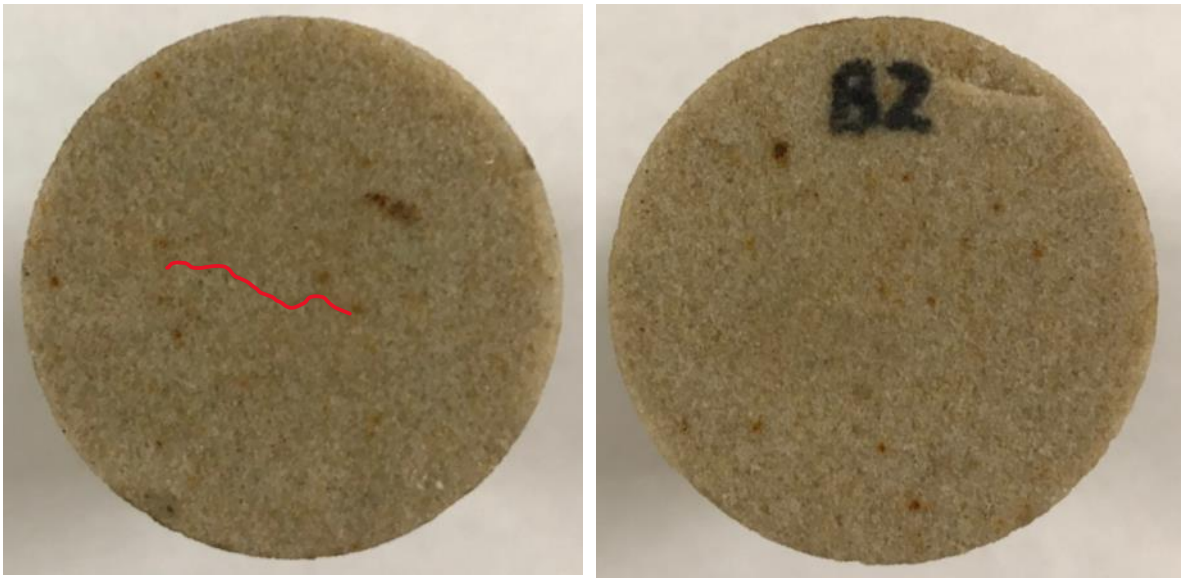

Figure 7: continued.

(c)

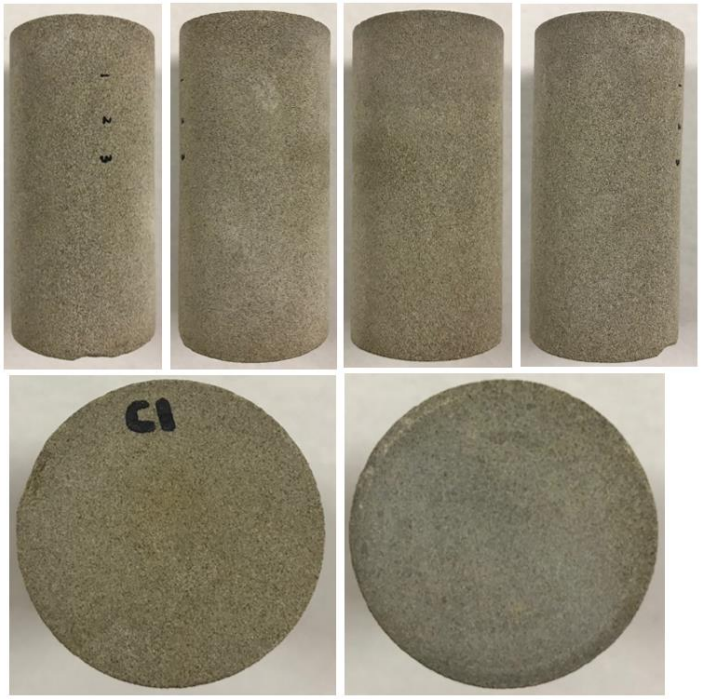

(d)

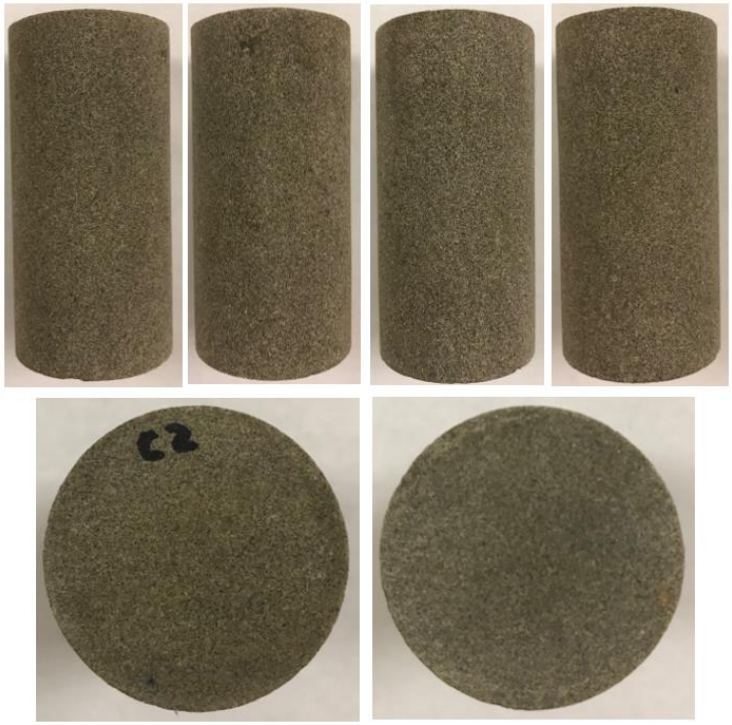

Figure 7: continued.

Micro-CT images were taken of the Bentheimer 2 specimen to investigate any internal fracturing that may have occurred. Only one small fracture is seen in the images. It is located approximately 1.5″ from the bottom of the specimen, where the large fracture is on the surface.

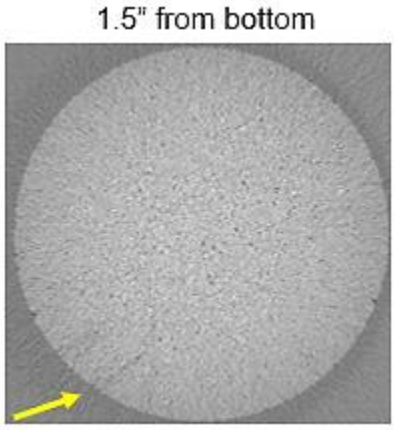

Figure 8: Micro-CT image of Bentheimer 2 after LN submersion. The yellow arrow is pointing to the internal fracture seen, which is located in the same spot as the large surface fracture.

Figure 9 and Figure 10 show S-wave and P-wave signals, respectively, for all four sandstone specimens before and after treatment. The characteristic of acoustic signatures corresponds to the density of the surface cracks. For example, the S and P-wave acoustic signals for Colton 1 were the least changed in terms of arrival time. For Bentheimer 2, the S-wave acoustic signals were the most changed. This corresponds with our observations, where Colton 1 had no surface cracks and Bentheimer 2 had the large surface cracks. The changes in P and S-wave velocities are summarized in Figure 11. The wave velocities of all specimens decreased after liquid nitrogen submersion. However, the saturated specimens' velocities decreased by 10-17%, while the wave velocities of the dry specimens decreased by 0.5-8%. Between the dry specimens, Bentheimer had a higher reduction of acoustic velocity. Conversely, between the saturated

specimens, Colton had a higher reduction of acoustic velocity. This means the saturated Colton specimen experienced damage by invisible micro-cracks.

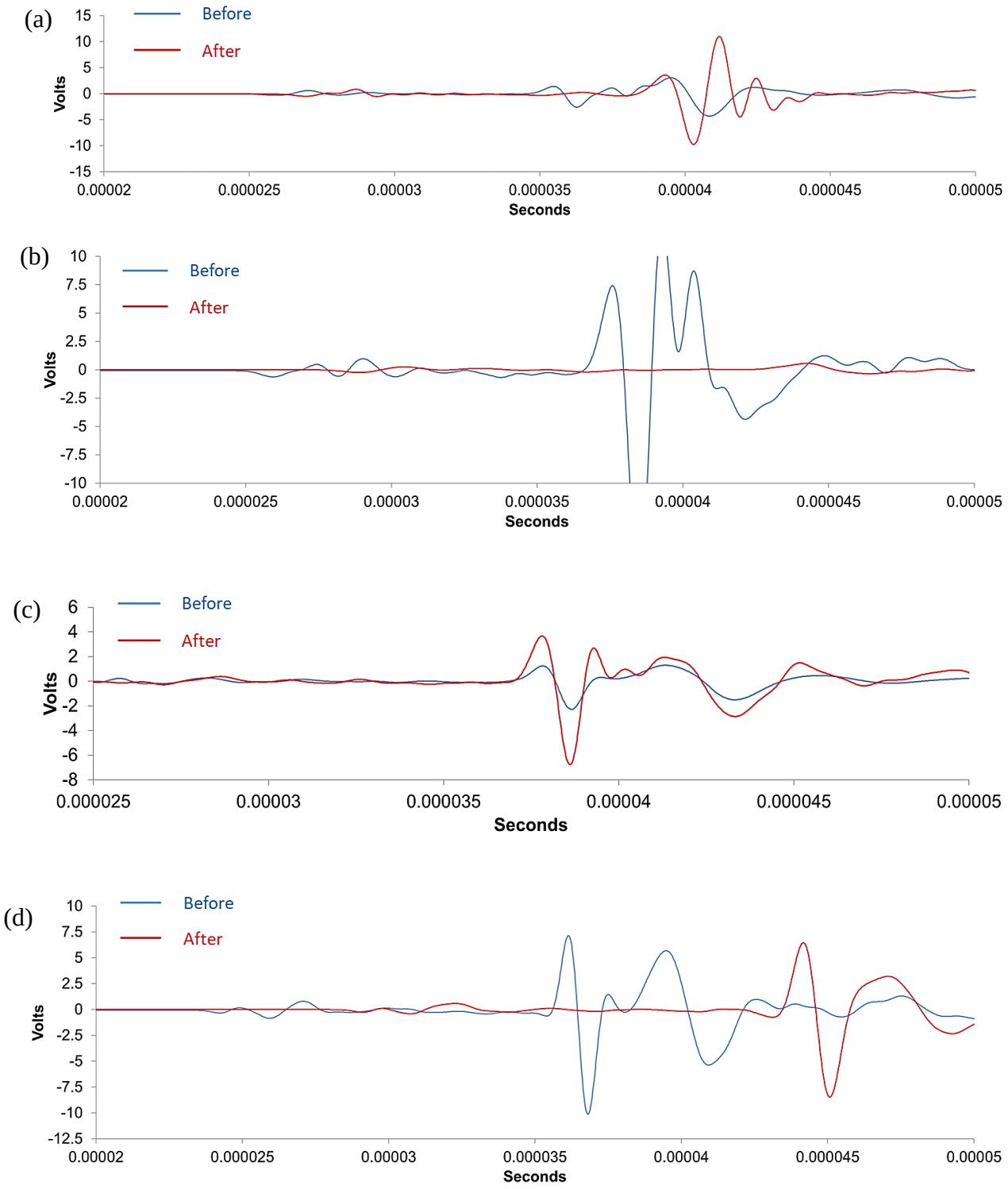

Figure 9: S-wave signals near arrivals between two ends of cores before and after LN submersion. (a) Bentheimer 1 - dry. (b) Bentheimer 2 - saturated. (c) Colton 1 - dry. (d) Colton 2 - saturated.

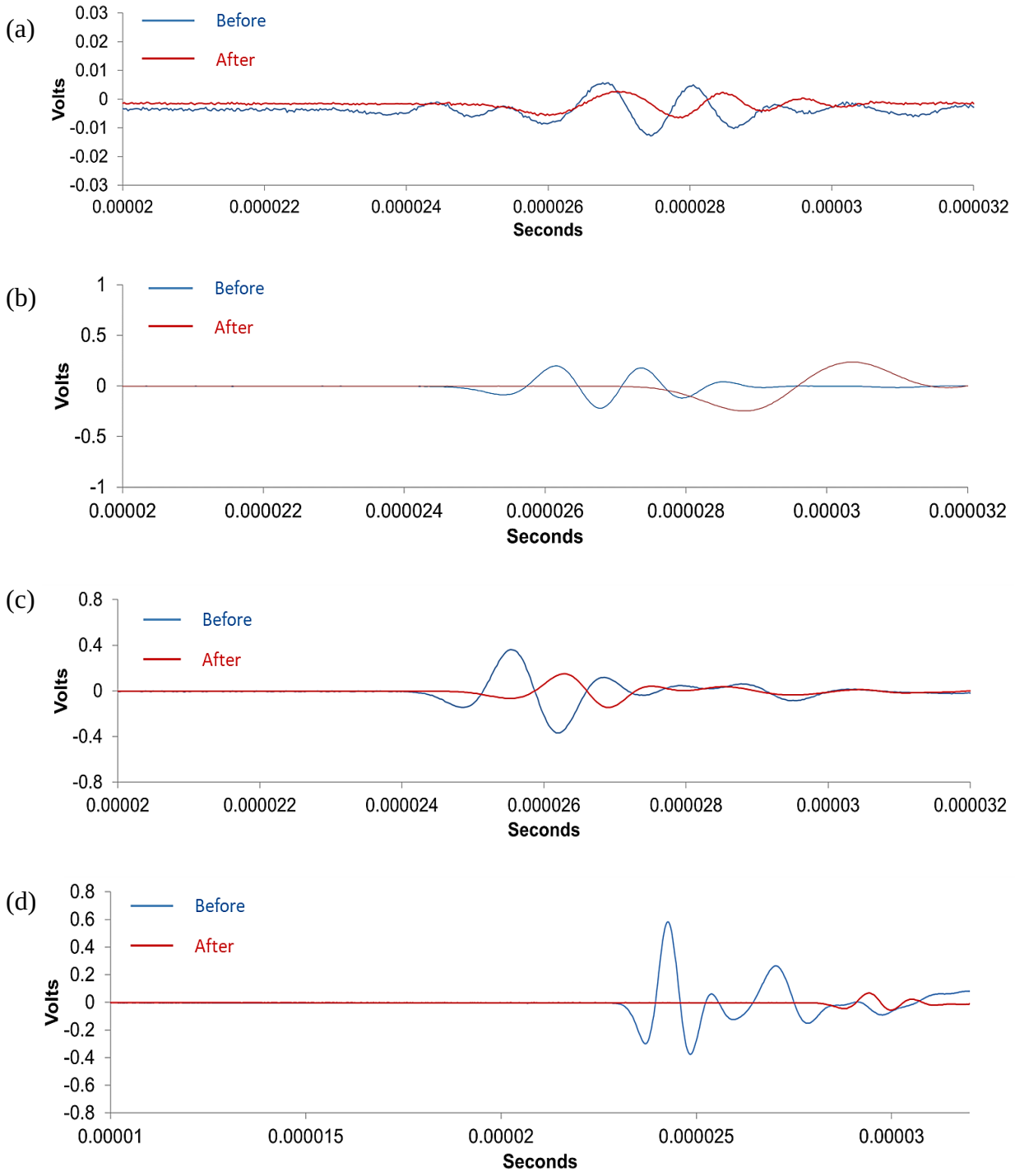

Figure 10: P-wave signals near arrivals between two ends of cores before and after LN submersion. (a) Bentheimer 1 - dry. (b) Bentheimer 2 – satuated. (c) Colton 1 - dry. (d) Colton 2 - saturated.

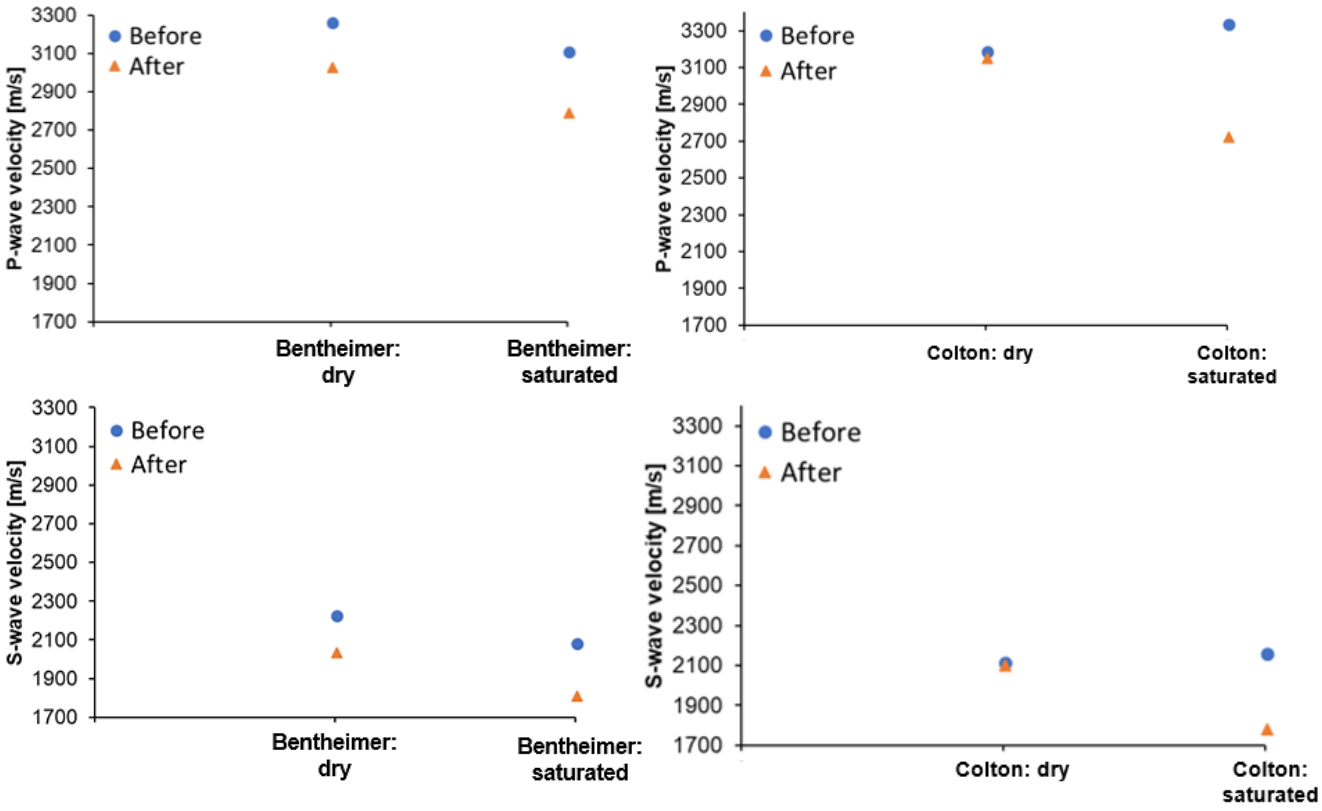

Figure 11: Changes in P- and S-wave velocities before and after LN submersion.

Permeability of all specimens were measured again after LN submersion. Results show that all specimens experienced an increase in permeability and porosity. Colton 1 and Colton 2 have particularly large increases in permeability, about 1000% increase. The pore structure of the saturated sandstones was assumed to be significantly damaged due to the expansion of the freezing water. This was reflected in the measurements we obtained after submersion. We assumed the porosity of the dry specimens would decrease due to the contraction of the mineral skeleton in contact with LN. However, this was not the case. Brine water from saturating all the specimens with 5 wt. % KCl for the permeability tests before LN submersion may have resided in the pore

space. Specimens were heated to elevated temperatures, but water can remain trapped in isolated micropores.

Table 5: Permeability and porosity of specimen before and after treatment.

	Bentheimer 1 (dry) before	Bentheimer 1 (dry) after	Bentheimer 2 (saturated) before	Bentheimer 2 (saturated) after	Colton 1 (dry) before	Colton 1 (dry) after	Colton 2 (saturated) before	Colton 2 (saturated) after
Permeability (k)	491 mD	658 mD	430 mD	673 mD	0.03 mD	0.35 mD	0.036 mD	0.37 mD
Porosity (ϕ)	18%	20.5%	19%	22.3%	8.8%	10%	9.12%	10.3%

2.2.2 Observations and results: Shale submersions

The saturated shale specimens had surface fractures from saturation procedure in the vacuum chamber before submersion tests. Upon placing the shale cores in the liquid nitrogen, rapid boiling started on the contact due to the large difference in temperature. Cracking was heard as specimens continue to be under LN. This rapid boiling continued in the saturated specimens for a longer time than the dry specimen, leading us to believe saturated specimens took longer to reach thermal equilibrium. The dry specimens experienced larger bubble formation from LN boiling compared to the saturated specimens, which experienced smaller bubbles. Boiling was unevenly distributed throughout surfaces for all the specimens (both dry and saturated). Figure 12 displays a drawing of the LN bubbles formed from each specimen during submersion. The concentrated area of bubbles circled in red on Mancos 3 (dry) is a point of particularly rapid and prolonged boiling with large bubbles.

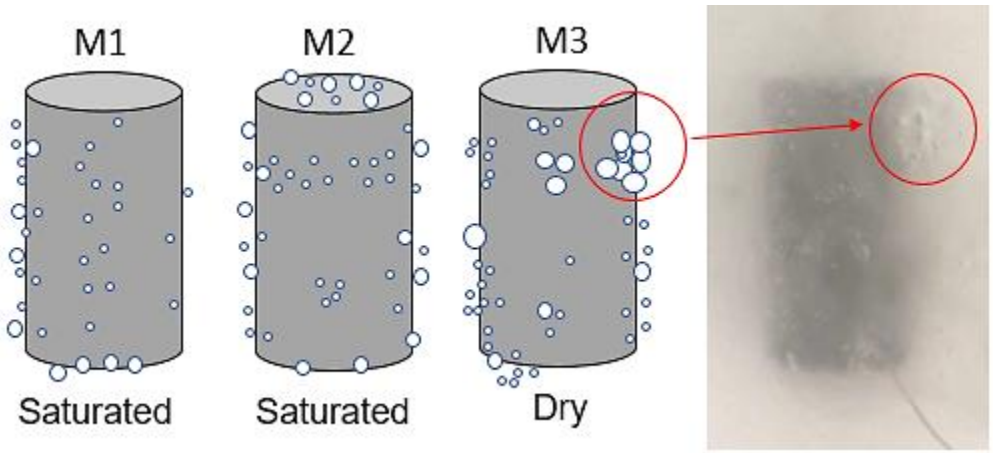

Figure 12: Liquid nitrogen boiling patterns on shale cores during submersion.

Thermocouples were placed on the surface of the dry and saturated specimens. From Figure 13, the surface of the saturated specimen took longer to reach the liquid nitrogen boiling point (-196 °C) than the dry specimen. During testing, it was observed that the boiling surrounding the dry specimen began to subside before the saturated specimens. The temperature changes reflects this observation, as the dry specimen reached -196 °C quicker than the saturated. From Table 6, we calculated the saturated specimen to have a higher effective thermal diffusivity value than the dry specimen, but this was not the case, based on our observations.

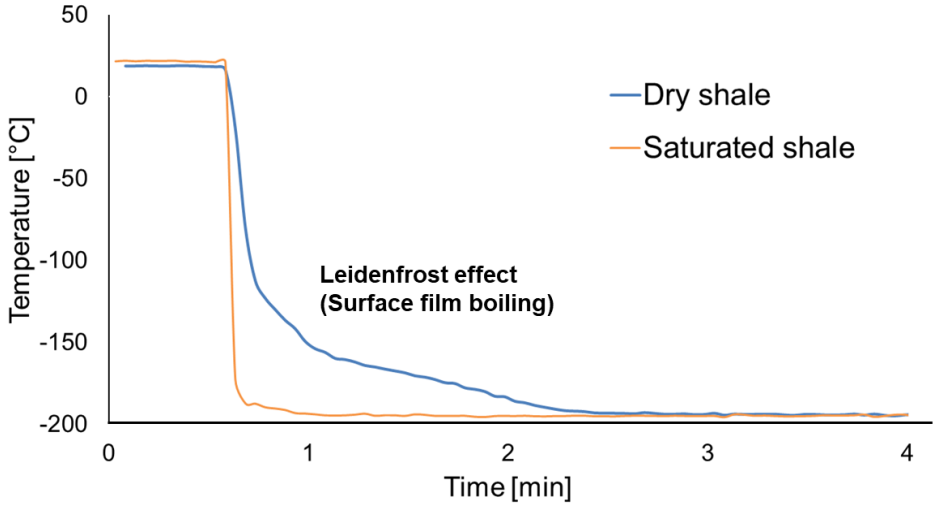

Figure 13: Temperatures on the surface of the shale cores during LN submersion.

When submerged, all specimens experienced ice growing on their exposed surfaces. However, the dry specimen had ice formation occurring before the saturated did. The dry specimen also had more ice growth than the saturated specimens (Figure 14). The Leidenfrost effect can be affected by the temperature and roughness of the solid surface submerged in the cryogen.

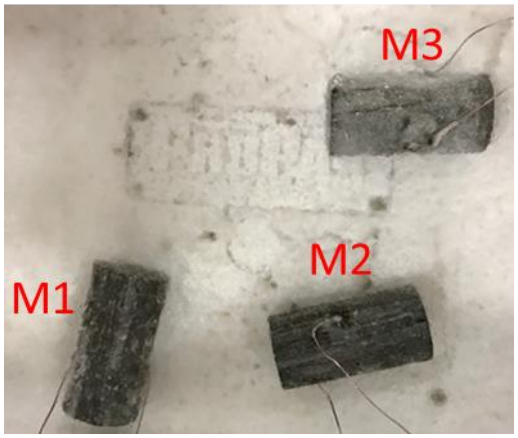

Figure 14: Shale cores approximately 5 minutes into LN submersion. Notice M3 (dry) specimen's surface is covered in ice (white area), whereas M1 and M2 are not.

After submersion tests, the initial cracks on saturated specimens (M1 and M2) became wider and new fractures extended from them. The dry specimen (M3) had no surface fractures before submersion. Afterwards, the dry specimen had a few large cracks on the surface. The large fracture on M3 is in the same place that rapid and prolonged boiling occurred (Figure 12). Overall, M1 and M2 experienced more fracturing than the dry specimen.

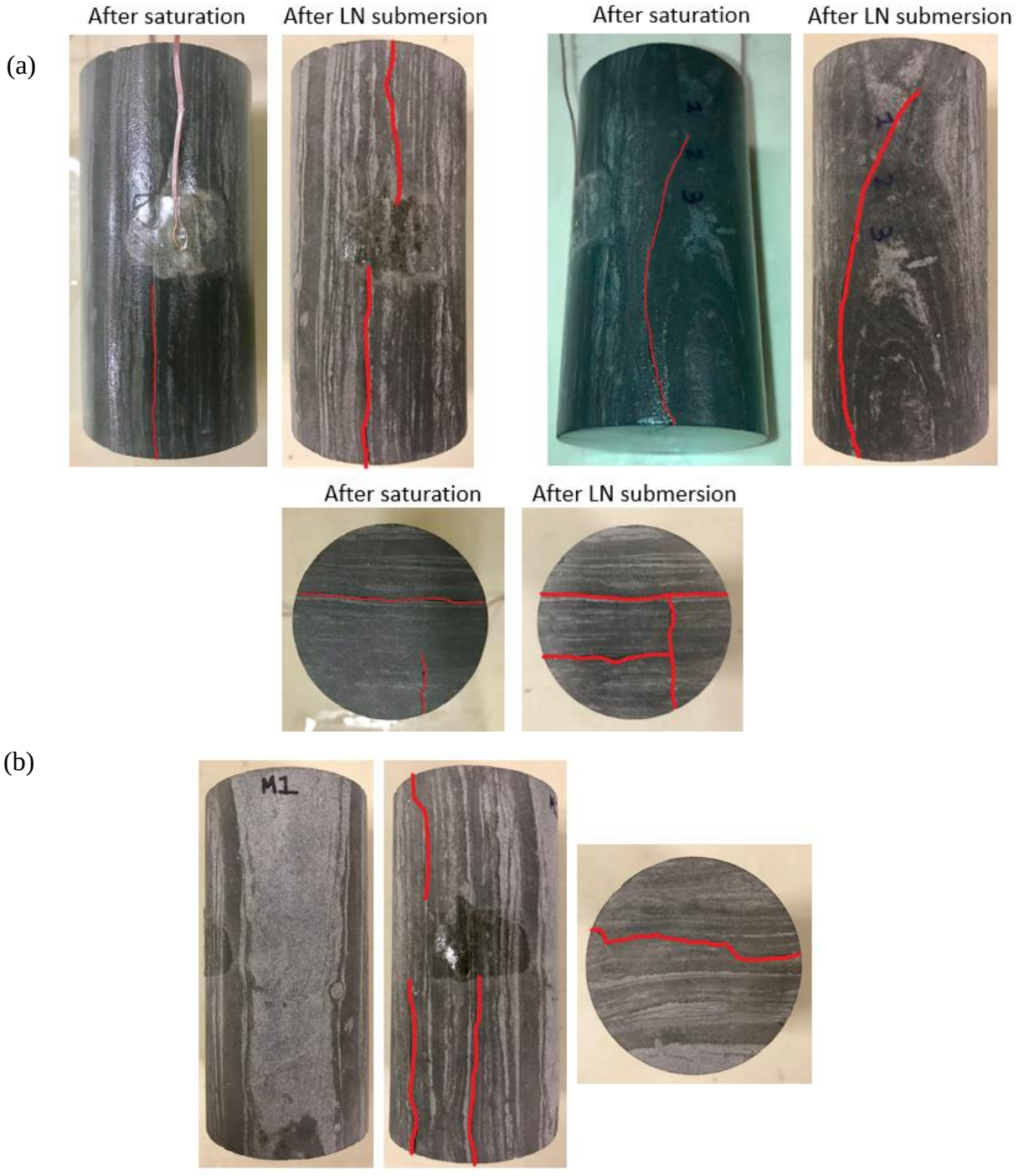

Figure 15: Mancos shale 1 (saturated). (a) A comparison of fractures caused from saturation before LN submersion and fractures after LN submersion. (b) New fractures formed on the specimen due to LN submersion (other sides). Red lines are drawn over fractures. Line thickness reflects fractures aperture.

(a)

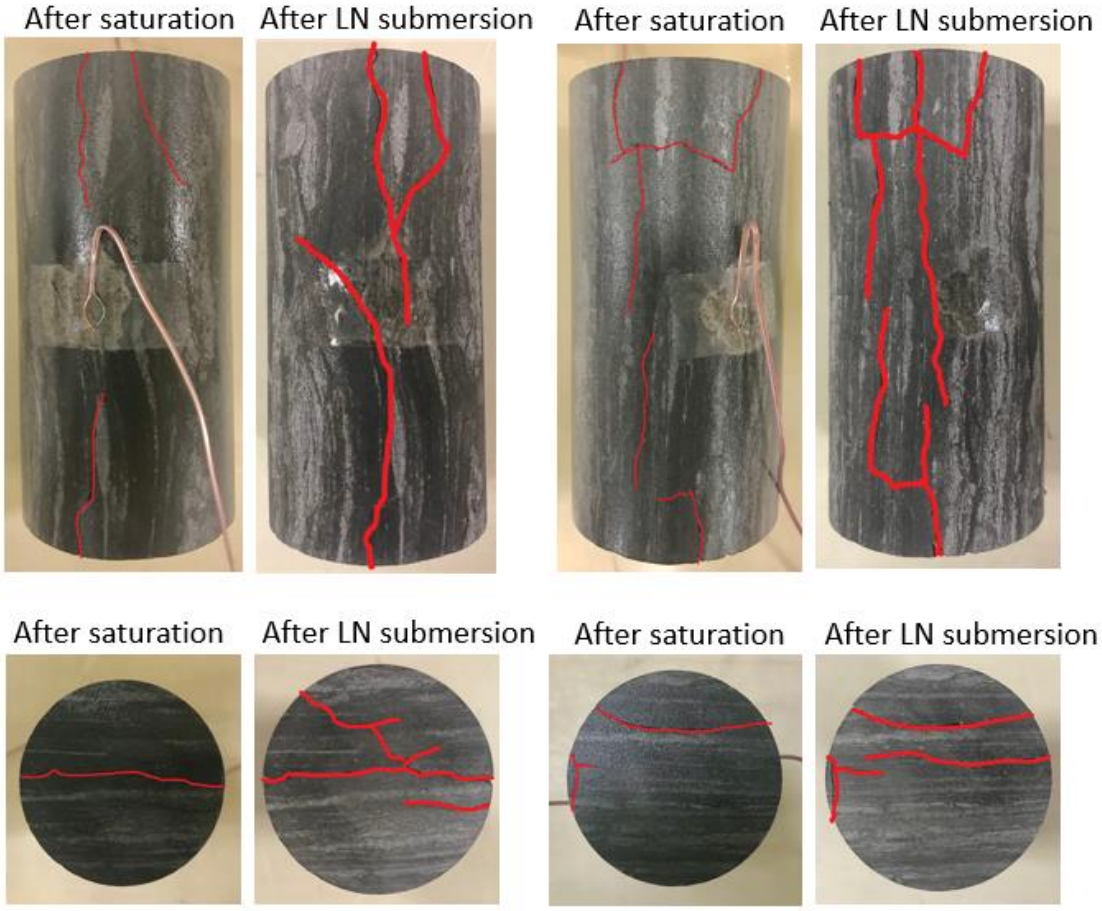

(b)

Figure 16: Mancos shale 2 (saturated). (a) A comparison of fractures caused from saturation before LN submersion and fractures after LN submersion. (b) New fractures formed on the specimen due to LN submersion (other sides). Red lines are drawn over fractures. Line thickness reflects fractures aperture.

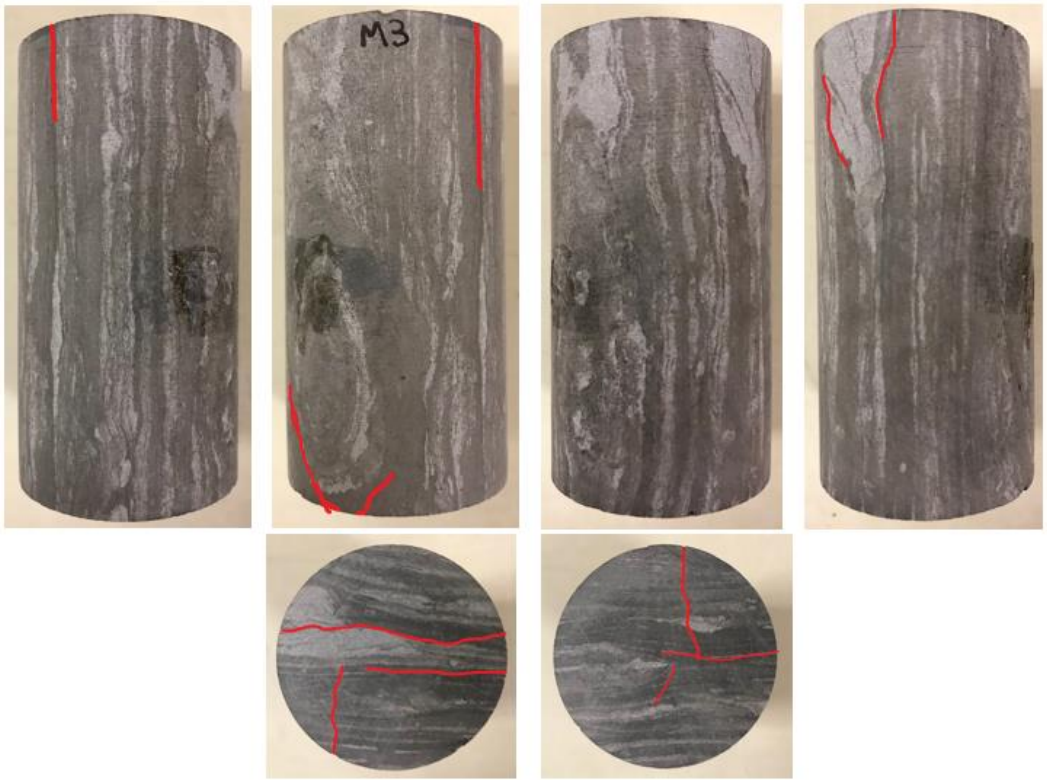

Figure 17: Mancos shale 3 (dry) after LN submersion. Notice fewer fractures than on the saturated specimens. Red lines are drawn over fractures. Line thickness reflects fractures aperture.

Acoustic measurements before and after tests were taken on the specimens using P and S ultrasonic transducers. The differences in the acoustic signatures before and after cryogenic stimulation were then examined, focusing on P and S wave velocities and amplitudes. Figure 18, 19, and 20 show S-wave and P-wave signals, respectively, for all four sandstone specimens before and after treatment. The characteristic of acoustic signatures corresponded to the spacing of the surface cracks. For example, the S and P-wave signals for Mancos 3 were the least changed in terms of arrival time. For Mancos 1 and 2, the S-wave acoustic signals had dramatic delays in arrival time. This corresponds with our observations, where Mancos 3 had few surface cracks and Mancos 1 and 2 had large surface fractures on many sides. The changes in P and S-wave velocities are summarized in Figure 21. The wave velocities of all specimens decreased after liquid nitrogen

submersion. However, the saturated specimens' S-wave velocities decreased by 16-20%, while the S-wave velocities of the dry specimen decreased by 4%. Something interesting we found was that the dry specimen's P-wave velocity decreased by 7.6%. On the other hand, the saturated specimen's P-wave velocity decreased by 4-4.5%.

The P and S wave velocity of all specimens decreased, caused by both internal and surface fractures. The saturated specimens decreased in S-wave velocity more than the dry specimen did. This means that the saturated experienced more fracturing than the dry specimens, which is obvious from observations.

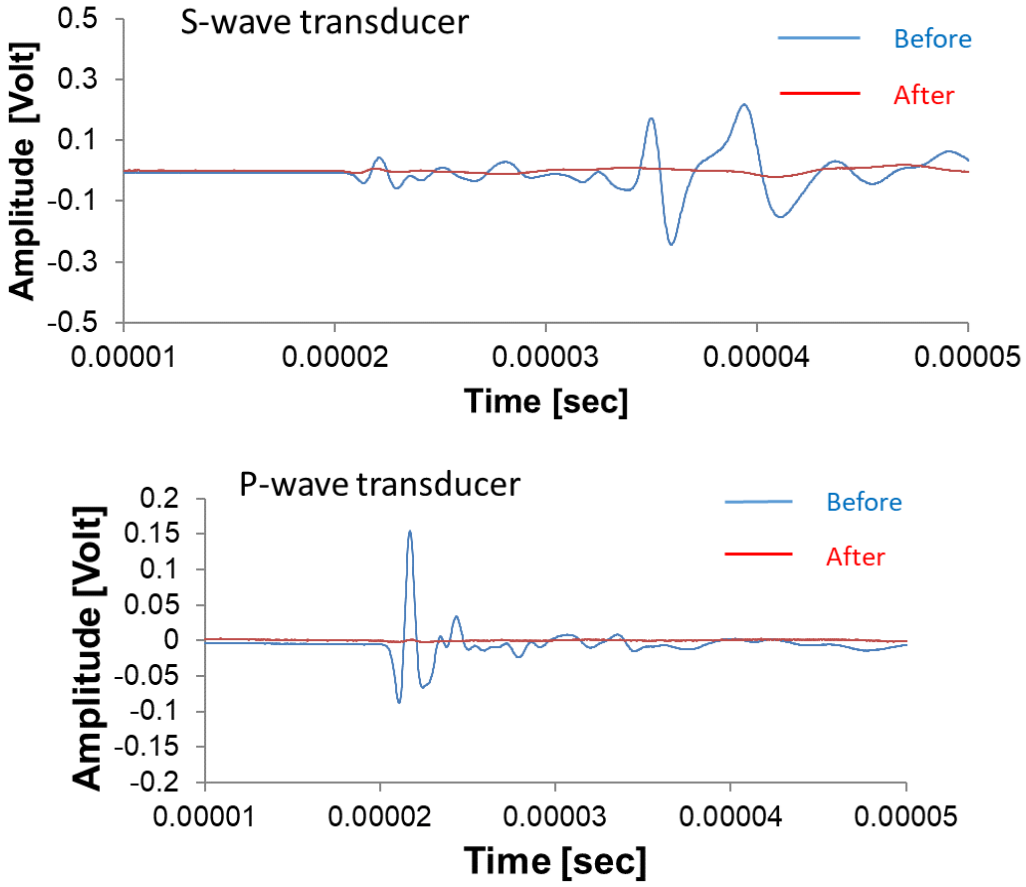

Figure 18: S- and P-wave signals near arrivals between top and bottom of Mancos 1 (saturated) core specimen before and after LN submersion.

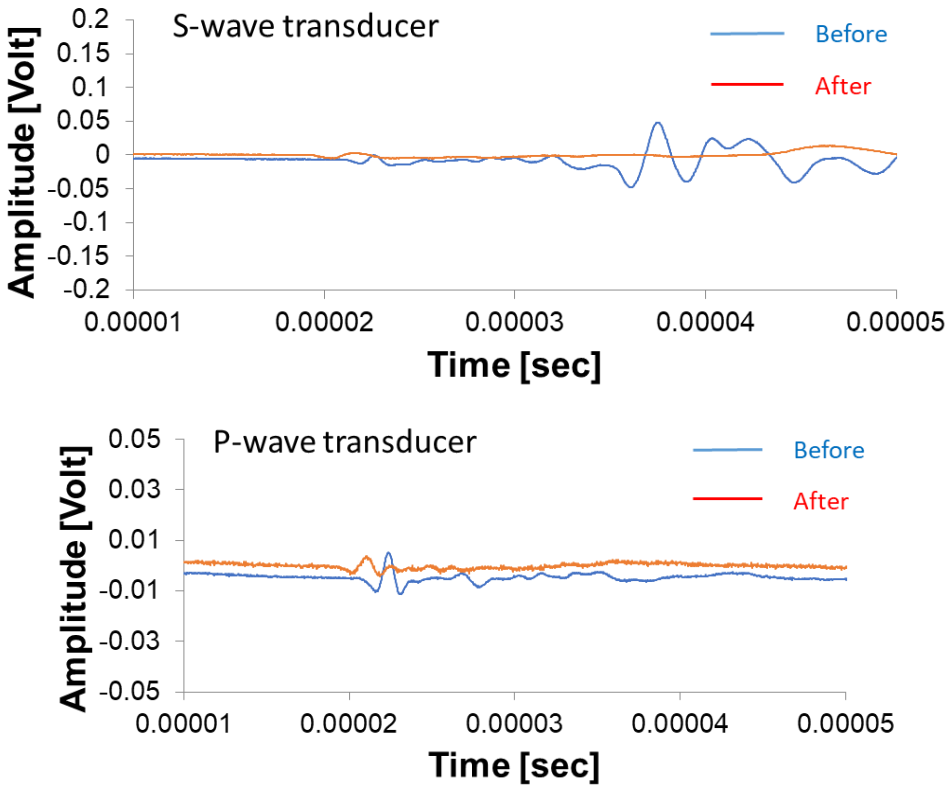

Figure 19: S- and P-wave signals near arrivals between top and bottom of Mancos 2 (saturated) core before and after LN submersion.

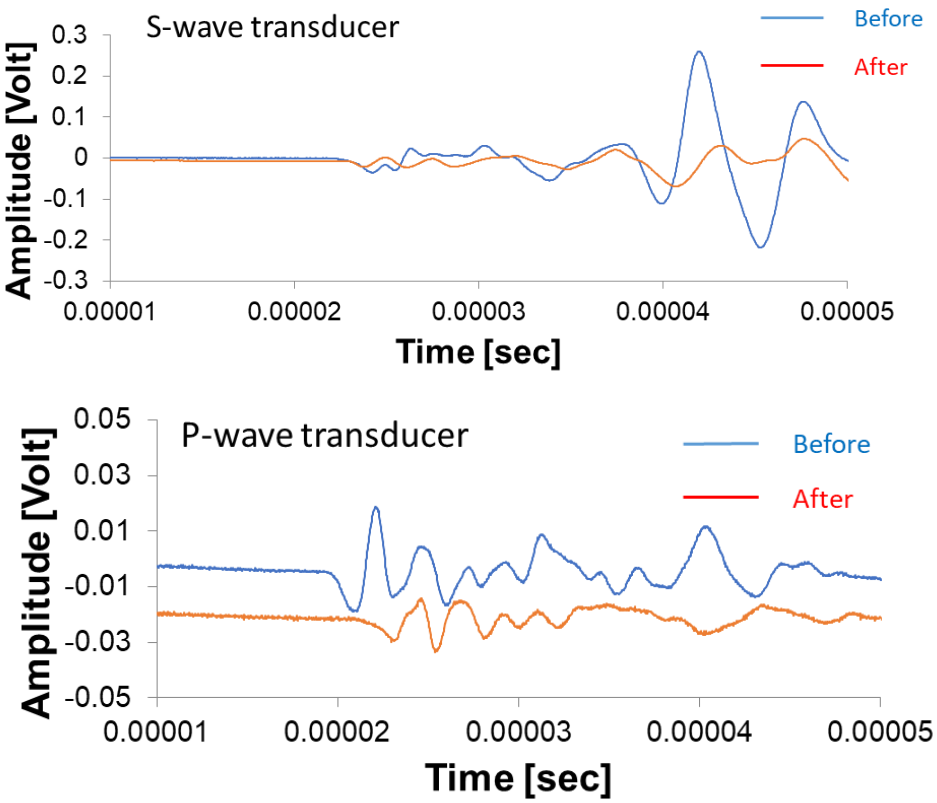

Figure 20: S- and P-wave signals near arrivals between top and bottom of Mancos 3 (dry) core before and after LN submersion.

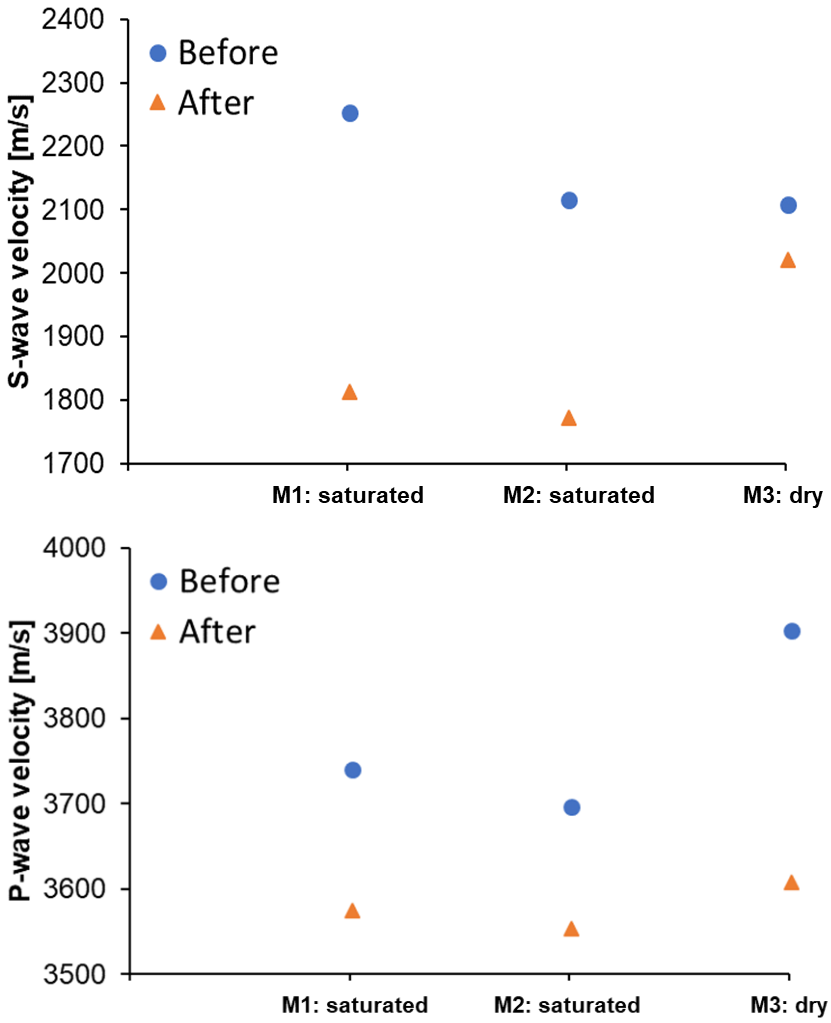

Figure 21: Changes in P- and S-wave velocities before and after LN submersion.

Micro-CT images of Mancos 1 (saturated) and Mancos 3 (dry) were taken to examine internal fracturing. Both the dry and the saturated specimens experienced internal fracturing parallel and perpendicular to the bedding plane. The yellow lines in Figure 22 and 23 represent the direction of the bedding planes for each specimen. Therefore, fractures parallel to the yellow line are formed along the bedding planes and fractures perpendicular to it are formed through the bedding planes. Neither specimen had a fracture that extended throughout the entire length of the cylinder shape. Instead, it seemed that the top and the bottom fractured on different planes. As the

specimen returned to room temperature, fractures tended to close. Therefore, no self-propping mechanisms were found in our laboratory-sized experiments.

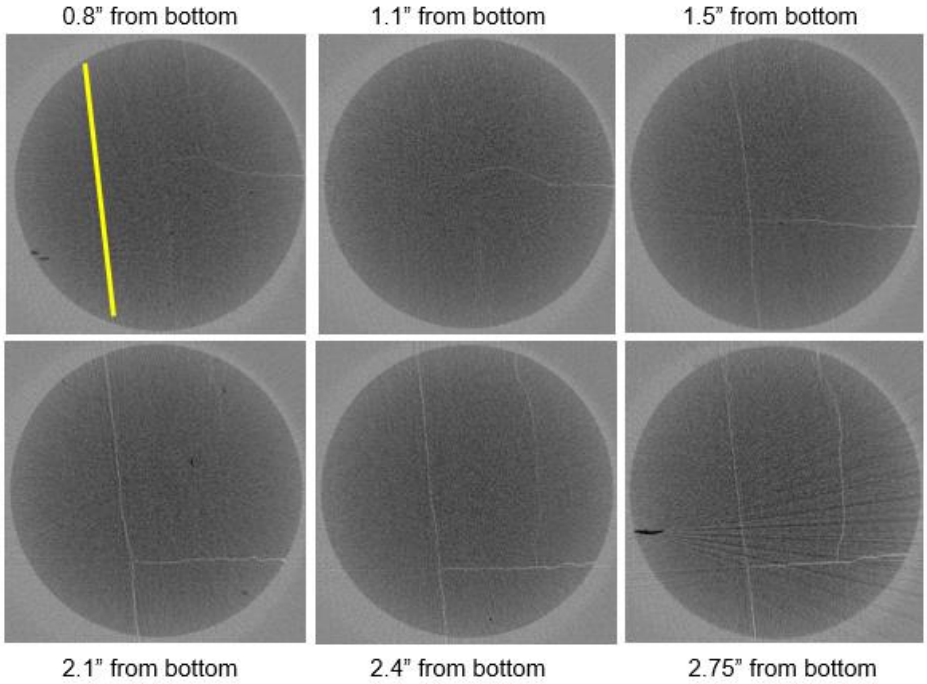

Figure 22: Micro-CT slices of Mancos 1 (saturated) core. White lines on photos are fractures. The added yellow line represents the direction of the bedding planes. Black areas represent higher density areas that reflect the beam light, causing scatter. Note: 23 micron resolution.

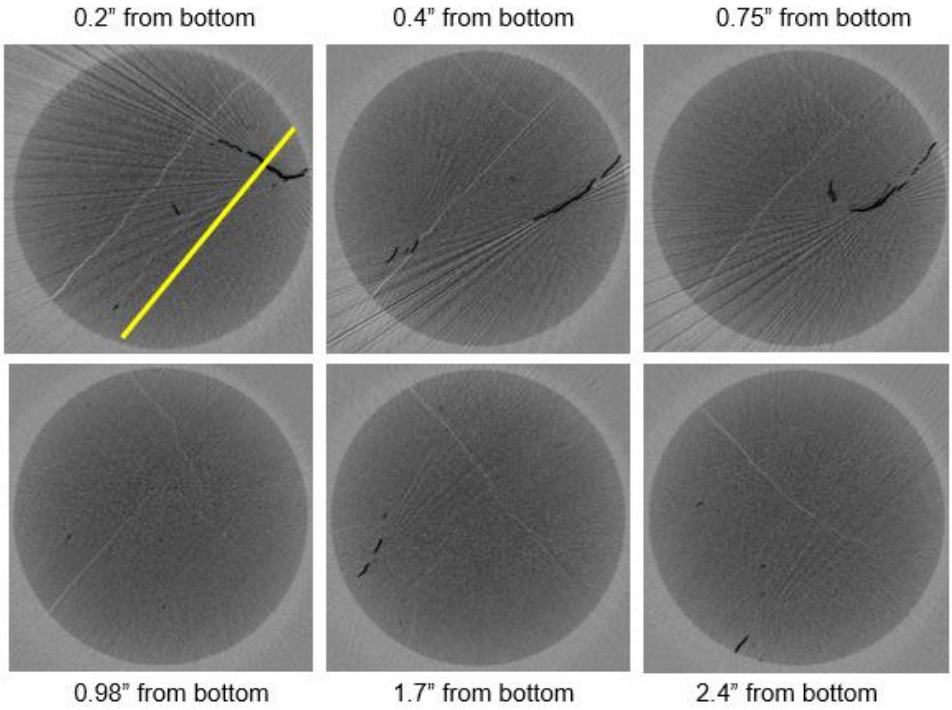

Figure 23: Micro-CT slices of Mancos 3 (dry) core. White lines on photos are fractures. The added yellow line represents the direction of the bedding planes. Black areas represent higher density areas that reflect the beam light, causing scatter. Note: 23 micron resolution.

2.3 Discussion

Effective thermal conductivity of dry sandstone specimens is estimated by $(1-n) \cdot k_Q + n \cdot k_a$, where n is porosity, k_Q is the thermal conductivity of quartz grains (because the sandstone specimen are 99% quartz), and k_a is thermal conductivity of air. On the other hand, effective thermal conductivity of saturated sandstone specimens is estimated by $(1-n) \cdot k_Q + n \cdot k_w$, where k_w is thermal conductivity of water. Effective specific heat (c_p). is calculated similarly. Effective thermal diffusivity is calculated using:

$$\mathbf{D} = \frac{\boldsymbol{k}}{\boldsymbol{\rho c_p}} \qquad \text{Equation 4}$$

where k is effective thermal conductivity [W/(m·K)], ρ is density [kg/m^3], and c_p is effective specific heat capacity [J/(kg·K)].

Notice that Bentheimer 2 (saturated) has a low value of effective thermal diffusivity; this denotes that B2 will take the longest time to reach a state of thermal equilibrium. On the other hand, Bentheimer 1 (dry) will take the least amount of time, followed by Colton 1 (dry) and then Colton 2 (saturated).

The effective linear thermal expansion coefficient (α) of saturated specimen is similarly calculated by (1-n) • α_Q + n • α_{ice}. The linear thermal expansion coefficient of ice is used for the void space because saturated specimens' void space becomes ice when fully submerged in liquid nitrogen.

$$\sigma_{max}^{\Delta T} = \frac{E}{1-\nu}\alpha \cdot \Delta T \qquad \text{Equation 5}$$

In this equation, ΔT is temperature difference, α is the effective linear thermal expansion coefficient [/K], E is static Young's modulus [GPa], and ν is Poisson's ratio. From the properties in Table 1 and $\Delta T = 200℃$, we obtain the values given in Table 6. The maximum thermal stress of Benthiemer 1 and 2, and Colton 1 and 2 are significantly larger than the materials' tensile strength (Table 4). This indicates that fractures will occur in these specimens under LN submersion. The saturated specimens' maximum thermal stress was higher than the dry specimens. Therefore, we should expect the saturated specimens to be stronger than the dry specimens. From Table 6, the specimens saturated with water are calculated to have a higher effective thermal conductivity than the dry specimens. However, the water-saturated specimens have a lower effective thermal diffusivity value than the dry specimens.

According to Levinthal et al. (2016), an XRD analysis of Mancos shale show that they are composed of ~65% Quartz + feldspar, ~30% Calcite + Dolomite, and ~5% clay. The effective thermal conductivity, effective specific heat, and effective linear thermal expansion coefficient were calculated using the same method as the sandstone cores, however, the mineral grains are accurately represented by the mineral composition of the Mancos shale. Saturated shale specimens were calculated to have higher values of effective thermal conductivity and effective thermal diffusivity. This means saturated specimens will reach thermal equilibrium higher than the dry specimen. They also have a higher value of effective linear expansion coefficient and maximum thermal stress, which means saturated specimens will be able to handle more tensile stress from changes in the temperature of the material than the dry specimen.

Table 6: Thermal properties of sandstone and shale specimens.

	Effective thermal conductivity [W/(m·K)]	Density [kg/m^3]	Effective c_p [J/(kg·K)]	Effective thermal diffusivity [m^2/s]	Effective α [/K]	$\sigma^{\Delta T}_{max}$ [MPa]
Bentheimer 1 (dry)	2.46	2035	860.6	1.4×10^{-6}	8.0×10^{-6}	36.8
Bentheimer 2 (saturated)	2.54	2224	1466.5	7.79×10^{-7}	1.6×10^{-5}	68.4
Colton 1 (dry)	2.73	2402	844.96	1.35×10^{-6}	8.0×10^{-6}	43.2
Colton 2 (saturated)	2.78	2425	1135.52	1.0×10^{-6}	1.2×10^{-5}	71.0
Mancos shale (dry)	3.44	2610	688.44	1.9×10^{-6}	1.3×10^{-5}	108.96
Mancos shale (saturated)	3.47	2610	879.24	1.5×10^{-6}	1.6×10^{-5}	127.5

2.3.1 Discussion: Sandstone submersions

When liquid nitrogen encounters rock, heat from the rock will quickly transfer to the liquid nitrogen at boiling point (-195.8°C or -320.4°F) and result in the rapid cooling of the rock. This will cause the surface of dry rock to contract. When the tensile stress due to contraction exceeds the tensile strength of the rock, fractures orthogonal to the interface of cryogen and rock begin to form. However, saturated rocks may experience ice expansion against the mineral matrix due to the ice formation, which is interconnected through pores. This may cause the outer layer to expand laterally and result in shear fractures parallel to the exposed surfaces (Kneafsey et al. 2011). The saturated specimens experienced surface fractures along the circumference of the core, while the dry specimens showed little sign of visible surface cracking. However, the P and S wave velocity of dry specimens decreased, which may indicate invisible micro-cracks. In the water-saturated specimens, the Bentheimer sandstone is damaged more severely than the Colton due to its greater pore space. More pore space in the Bentheimer specimens allows a higher volume expansion of pore water to occur.

To understand the competition between expansion of the ice matrix and contraction of the mineral network for saturated specimens of different porosity, simple calculations were done. The volumetric thermal expansion of quartz (because majority of Bentheimer and Colton sandstone was composed of quartz (Al-Yaseri et al. 2015 and Dickinson et al. 2015)), α_{VQ}, is 2.4×10^{-5}/K. Assuming α_{VQ} is constant throughout the temperature range, and ΔT = 200 K, the volume reduction due to a cryogenic temperature change would be:

$$\text{Mineral phase volume reduction (\%)} = \Delta T \cdot \alpha_{VQ} \cdot 100\ (\%) = 0.48 \qquad \text{Equation 6}$$

The volume of water increases by 9% upon phase change to ice. Using the values of porosity, n, for Bentheimer 2 and Colton 2 that we obtained from the core-flood test (19% and 9.1%, respectively), the overall resulting volume change becomes:

Overall volume change of ice (%) = 9%·n
Overall volume change of mineral phase = volume reduction·(1- n)

Overall volume change (%) = (9%·n) – (volume reduction·(1- n)) Equation 7

It is calculated that the Bentheimer sandstone has an overall volume expansion of 1.32%. This is a higher expansion compared to the Colton, which is calculated to be 0.38%. The high porosity in the Bentheimer 2 leads to more ice formation in the void space of the rock, causing more expansion of the ice matrix against the mineral network. This was reflected in the photos of the specimens after submersion, where Bentheimer 2 showed a large surface fracture along the circumference of the core.

2.3.2 Discussion: Shale submersions

When the thermal tensile stress in dry rock exceeds the rock tensile strength, the inter-grain cementation is broken and fractures orthogonal to the interface of cryogen and rock begin to form. Saturated rock may experience expansion against the mineral matrix due to the formation of ice, which may cause the outer layer to expand laterally and result in shear fractures parallel to the exposed surfaces (Kneafsey et al. 2011). The saturated shale formed surface fractures mostly along the bedding planes. From the micro-CT images, Mancos 1 (saturated) also formed fractures perpendicular to the bedding plane. After considering that the shale cores were drilled parallel to the bedding planes in a shale block, we realize that the fractures perpendicular to the bedding plane

are initiated from fractures that began along the bedding plane (Figure 24). Due to the bedding planes orientation on the cylinder, some fractures along the bedding plane propagate into the inside of the specimen, forming perpendicular fractures.

The saturated shale cores experienced more fracturing than the dry specimens. However, it is unclear whether this is due to the initial fractures on the saturated specimens caused by saturation in the vacuum chamber. From visual inspection, it was observed that ice formation in the saturated specimens expanded the initial fractures from submersion. The dry shale had fewer fractures than the saturated, however, it does form more new fractures than the saturated (the dry specimen did not have initial fractures before submersion).

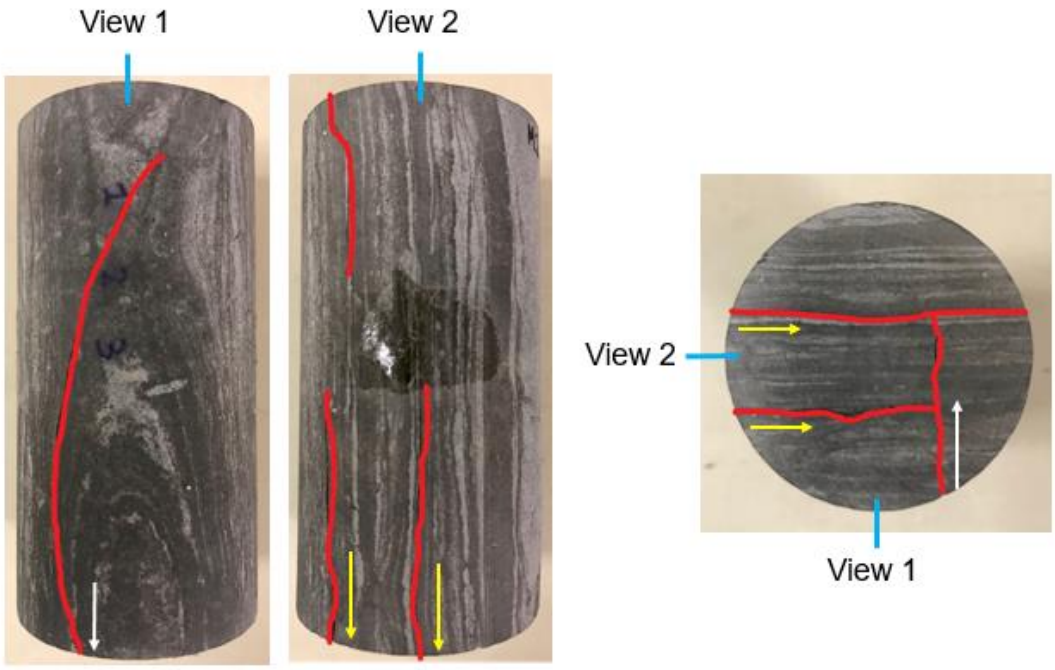

Figure 24: Orientation of the fractures along and perpendicular to bedding planes in Mancos 1 (saturated). The fracture from View 1 runs along bedding plane on the surface, but cuts into the specimen and creates fractures inside that cut through bedding planes. Note that yellow arrows represent fractures along bedding plane and white arrow represents the fractures that internally cut across bedding planes but cut along the bedding plane on the outside surface.

Volume reduction and the overall volume change was calculated to examine the competition between expansion of the ice matrix and contraction of the mineral network for saturated specimens. The volumetric thermal expansion of shale, α_{Vshale}, calculated earlier for thermal properties, is 4.68×10^{-5}/K. Assuming α_{Vshale} is constant throughout the temperature range, and ΔT = 200 K, the volume reduction of minerals due to a cryogenic temperature change would be 0.94%. The volume of water increases by 9% upon phase change to ice. In a high porous specimen whose pore space undergoes expansion, it would be a reasonable to assume the overall volume will expand. Using 6% porosity, n, for Mancos 1 from Table 3, the overall resulting volume change is -0.34% (reduction). Therefore, the saturated shale will experience contraction due to its very low porosity.

Micro-CT images show the fractures of Mancos 1 (saturated) and Mancos 3 (dry) formed orthogonal to the interface of cryogen. This indicates fractures formed due to the tensile stress exceeding the tensile strength of the rock. From micro-CT, we can also see fractures are most prominent at the top and bottom of the specimens and then diminish as they move towards the middle of the 3″ tall specimen. This indicates that fractures were initiated at the surface and then propagated inside.

2.4 Conclusions

Liquid nitrogen submersion tests was conducted for small-scale sandstone and shale cores. The ability of liquid nitrogen to create fractures in water-saturated specimens was tested in submersion tests, and fracture assessments were made by visual inspection, X-ray micro-CT, and acoustic signatures. The amplitudes and velocities of acoustic waves were sensitive to micro cracks, and

thus were able to identify changes in properties that were not visible. Micro-CT images identified spatial distribution of major cracks and allowed us to identify fracture patterns. Measurement of temperature history on the shale specimens allow us to to monitor the heat transfer.

2.4.1 Sandstone submersion

The submersion of sandstone cores in liquid nitrogen resulted in cracks in the rock blocks and altered rock properties. The fractures were created by generating a strong thermal gradient in sandstone cores submerged in LN. Visible fractures and invisible micro-cracks were easily picked up by the acoustic measurements. Liquid nitrogen cooling changed the pore structure of the rocks. The major changes we witness included an increase in the porosity and permeability and their volume (from the expansion of freezing water in pore space), and the generation of large surface fractures. For dry rocks, LN submersion resulted in few surface fractures but an increase in permeability and porosity. Between the dry Colton and Bentheimer cores, the lower permeability sandstone (Colton) experienced a larger increase in permeability. This may be because of residual water trapped in isolated micro-pores. For saturated rocks, LN submersion results in intense damage to the pore structure. For instance, large surface fractures, as well an increase in permeability and porosity were observed. Between the saturated Colton and Bentheimer cores, the lower permeability sandstone (Colton) experienced a larger increase in permeability. This may be due to the higher density of cemented grains; as the ice expands, this specimen will experience more internal micro-fractures. Based on the results, it is clear that the generation of fractures was highly dependent on material properties.

2.4.2 Shale submersion

The submersion of shale cores in liquid nitrogen resulted in cracks in the rock cores and altered rock properties. Visible fractures and invisible micro-cracks were easily picked up by the acoustic signals. Acoustic amplitudes and velocities decreased after submersion due to the presence of large fractures. Liquid nitrogen cooling increased the fracture distribution of the rock. In particular, it generated cracks along the bedding planes and also perpendicular to the bedding plane. In the saturated shale cores, existing fractures were widened and extended. Fractures in shale reservoirs are the main storage and seepage channels for hydrocarbons. Therefore, liquid nitrogen cooling may be effective in increasing shale reservoir stimulation during fracturing, as exposure to cryogenic temperatures initiated fracturing.

CHAPTER III

LIQUID NITROGEN SUBMERSION TESTS: 8 INCH CONCRETE CUBE

In the study by Cha et al. (2014), the submersion test with an 8″ cubic concrete block saturated with water resulted in cracks created near edges. The outer layer expanded laterally, causing shear fractures to occur parallel to the exposed surface. To study the geometry of cryogenic fracturing in water-saturated specimen and dry specimen, we will now investigate large-scale submersion tests. We will perform multiple tests on dry and saturated specimens to observe differences in their fracturing patterns. More specifically, we will investigate how water-saturation in specimens effect cryogenic fracturing.

Specimens were submerged in a container with liquid nitrogen until approximate thermal equilibrium is reached. Submersion stimulations took place for 3-7 hours with a constant supply of LN. Concrete blocks were used in this study as a surrogate for rocks as it is easy to mold to form desired shapes and temperature sensors can be embedded. Fractures are characterized by acoustic measurements, photographs, and CT images. Different temperature gradients in dry and saturated specimens are analyzed to compare the thermal properties of specimens. The effects of water in the pore space of the concrete blocks is discussed.

3.1 Experimental Methods

3.1.1 Specimens

The concrete specimens were prepared with a water to cement ratio of 0.55, and sand to cement ratio of 2.5. The cement was injected into an 8″×8″×8″ mold and sealed in a plastic bag. After 24 hours, the seal and mold were removed, and the concrete was either cured underwater for over 30

days or was open-air cured. A list of concrete specimens and their curing information can be found in Table 7. The concrete specimens that were cured underwater for over 30 days remained underwater until testing and had no visible cracks before stimulation. A few concrete specimens were cured with thermocouples embedded halfway into the 8″ concrete cube. For those specimens, the 8″×8″×8″ mold was first filled halfway (4 inches) with cement and seven thermocouples were inserted 1 inch deep. The cement was sealed in a plastic bag and left to harden for 6 hours before filling the remaining space in the mold. The mold was then sealed again and after 24 hours, was removed from the concrete and cured underwater for over 30 days.

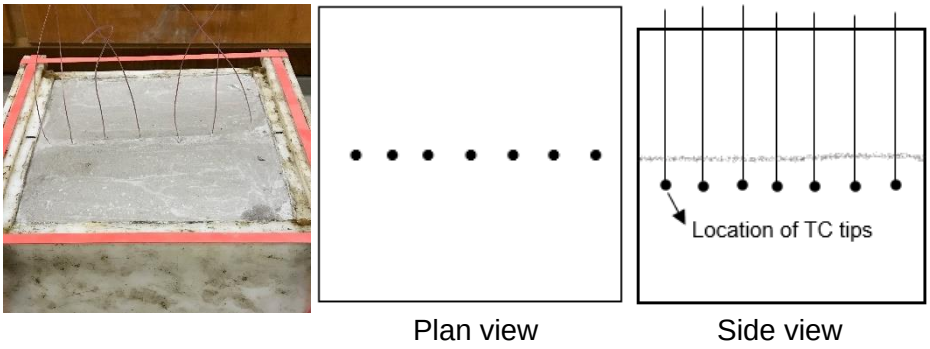

Figure 25: Embedded thermocouple placement in concrete block. Light grey line in the side view represents the weakness line from curing.

Table 7: Curing conditions of all tested concrete specimens. Specimens denoted with a "Y" were made in previous years.

Concrete specimens	Curing conditions	Temperature measurements
Con 1 – saturated	Underwater 45 days	-
Con 2 – saturated	Underwater 105 days	Surface
Con 5 – saturated	Underwater 46 days	Surface and embedded
Con 6 – saturated	Underwater 120 days	Surface and embedded
Con 7 – dry	Underwater 45 days; Open-air 14 days	Surface and embedded
Con Y-24 – dry	Open-air 21 months, 11 days	Surface
Con Y-29 – dry	Open-air 22 months, 10 days	Surface
Con Y-31 – dry	Open-air 20 months, 7 days	Surface

Note that specimens cured underwater will have higher strengths than open-air cured specimens.

3.1.2 Procedure

Both dry and saturated concrete block specimens were fully submerged in liquid nitrogen until approximate thermal equilibrium was reached. Approximate thermal equilibrium was reached when there was nearly no boiling of liquid nitrogen occurring at the interface between LN and the submerged block specimen surfaces. In the submersion tests, all blocks were fully submerged for approximately 3-7 hours.

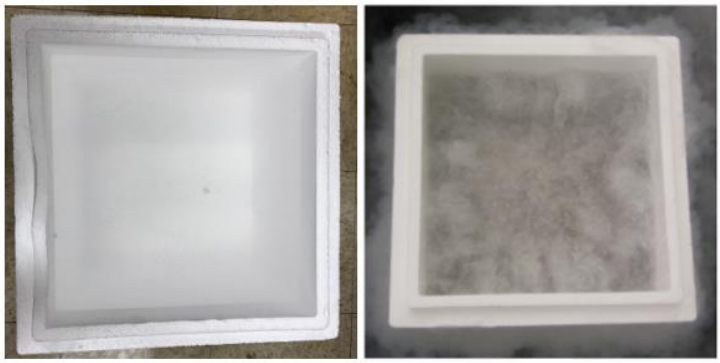

Figure 26: LN submersion test: (a) the liquid nitrogen filled inside a Styrofoam container and (b) violent LN film boiling at the interface between LN and the block surfaces.

Multiple tests were conducted due to inefficient supply of liquid nitrogen (the first two instances) and lack of full submersion on first contact with liquid nitrogen (the second two instances). The list of submersion tests and conditions applied on the concrete specimens is documented in Table 8.

Table 8: List of liquid nitrogen submersion experiments. Note that T represents temperature.

Specimen	Submersion method	Measurements	Liquid nitrogen	Duration (min)
Con 1 – saturated	Container is filled halfway with LN when specimen is placed inside	Acoustic (after)	54 Liter	150
Con 2 – saturated	Container is fully filled with LN when specimen is placed inside	Surface T, embedded T, acoustic (after)	70 Liter	310
Con 5 – saturated	Container is filled halfway with LN when specimen is placed inside	Surface T, acoustic (after)	70 Liter	365
Con 6 – saturated	Container is fully filled with LN when specimen is placed inside	Surface T, embedded T, acoustic (before, after)	42 Liter	156
Con 7 – dry	Container is fully filled with LN when specimen is placed inside	Surface T, embedded T, acoustic (before, after)	42 Liter	151
Con Y-24 – dry	Container is filled halfway with LN when specimen is placed inside	Surface T, acoustic (before, after)	70 Liter	409
Con Y-29 – dry	Container is fully filled with LN when specimen is placed inside	Surface T, acoustic (before, after)	70 Liter	381
Con Y-31 – dry	Container is filled halfway with LN when specimen is placed inside	Surface T, acoustic (before, after)	54 Liter	140

Temperature was measured using thermocouples (TC) at three faces of the specimens: two on opposing sides and one on the bottom of the specimen (Figure 27a). Thermocouples were attached to the faces using Epoxy or instant glue (Figure 27b). Specimens with embedded thermocouples had seven spaced an inch apart from each another, plus the three on the surfaces of the specimens.

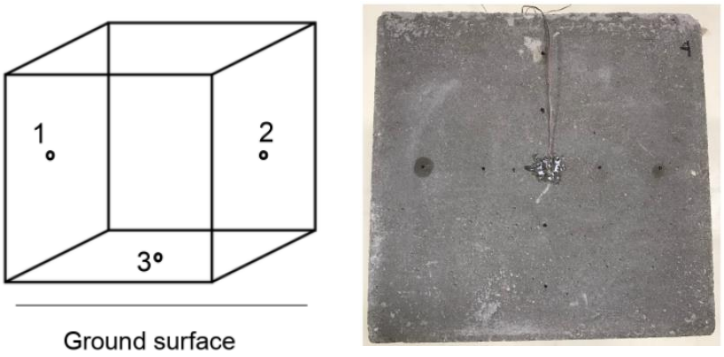

(a) (b)

Figure 27: (a) Locations of surface thermocouples. (b) Thermocouple attached with epoxy on a surface.

3.1.3 Fracture Characterization

Fracture development of all specimen are characterized using acoustic signatures and visual photos. Computed tomography (CT) scans were also done on selected specimen to further characterize fracture development using a Toshiba Medical CT Scanner.

The characteristics of acoustic waves propagating through a medium depend on the mechanical properties of the medium (Cha et al. 2009). The wave velocity in jointed rock masses is a function of the density of cracks, or joint spacing as modeled by:

$$V_s = \sqrt{\frac{G_{eq}}{\rho}} = \sqrt{\frac{1}{\rho}\left(\frac{k_S S G}{k_S S + G}\right)}$$

where V_S is shear wave velocity, k_S is shear joint stiffness, G is shear modulus of intact part, ρ is rock mass density, and S is joint spacing. When intact rock properties, density, and joint stiffness remain the same, the acoustic wave velocity can be used to characterize crack generation. Geomaterials allow acoustic waves to travel naturally due to inherent discontinuities such as granular discreteness and cracks. The high frequency content is filtered when acoustic waves propagate through cracked media (Cha et al. 2014). Acoustic measurements before and after tests

were taken on specimens using P and S ultrasonic transducers. The differences in the acoustic signatures before and after cryogenic stimulation were then investigated, focusing on P and S wave velocities and amplitudes.

3.2 Observations and Results

Upon placing concrete block specimens in the container filled with liquid nitrogen, LN began to violently boil at the interface between the block surface and LN. As time progressed, the rate of LN boiling at the specimen surfaces slowed, and the bubbles formed from boiling also began to shrink in size. This indicated the block was getting cooler and closer to reaching thermal equilibrium.

Before submersion, the only specimen to have small cracks on the surface was Con Y-29 on Face 5 (top face). No other concrete specimens had visible fractures on surfaces prior to LN submersion. After submersion of the dry specimens, there was minimal visible damage to the surface or extensions of existing fractures, as we see in Con Y-29 (Figure 28). Conversely, many large surface fractures and small cracks were generated and visible on the surface of saturated specimens (Figure 29). The curing process for Con 6 and Con 7 (embedded thermocouple specimens) created a weakness in concrete bonding. Because of this, a prominent fracture is created along this weakness line after LN stimulation (Figure 30).

(a)

(b)

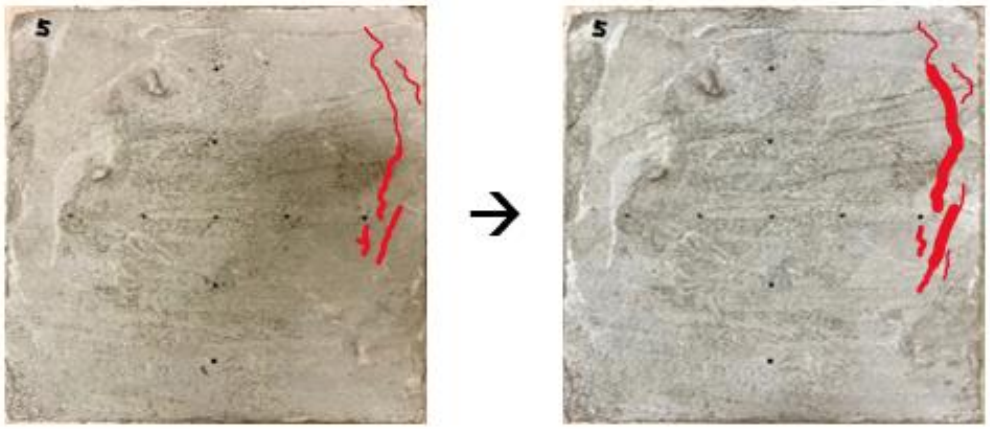

Figure 28: Dry blocks: (a) Con Y-24 specimen after thermal shock. (b) Face 5 of Con Y-29 specimen. Notice existing small fractures before stimulation (left) become wider after submersion (right).

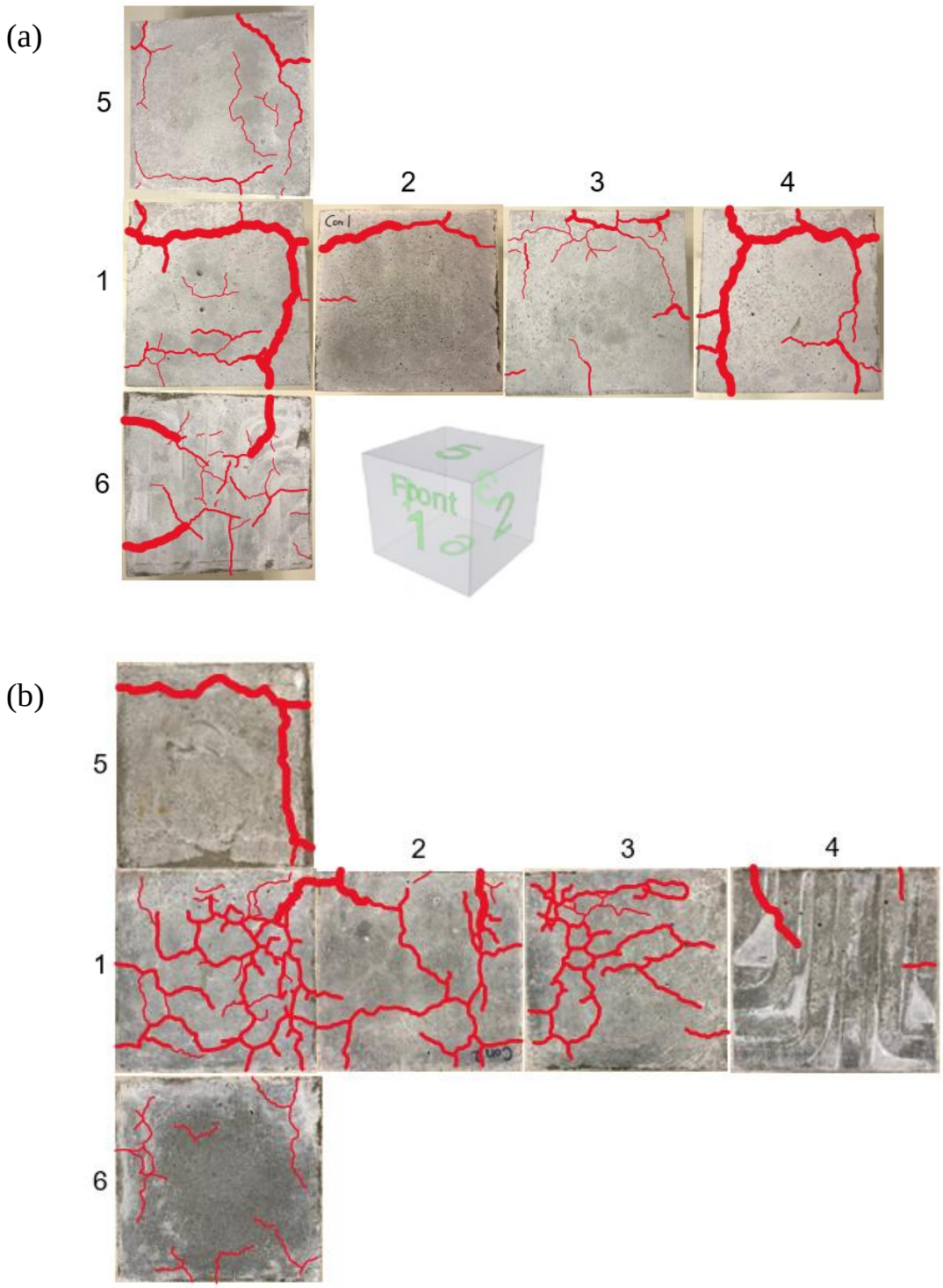

Figure 29: Saturated blocks: (a) Con 1 specimen after thermal shock. (b) Con 2 specimen after thermal shock - red lines are superimposed along the cracks to improve visibility. Line thickness reflects the thickness of fractures present.

(a)

(b)

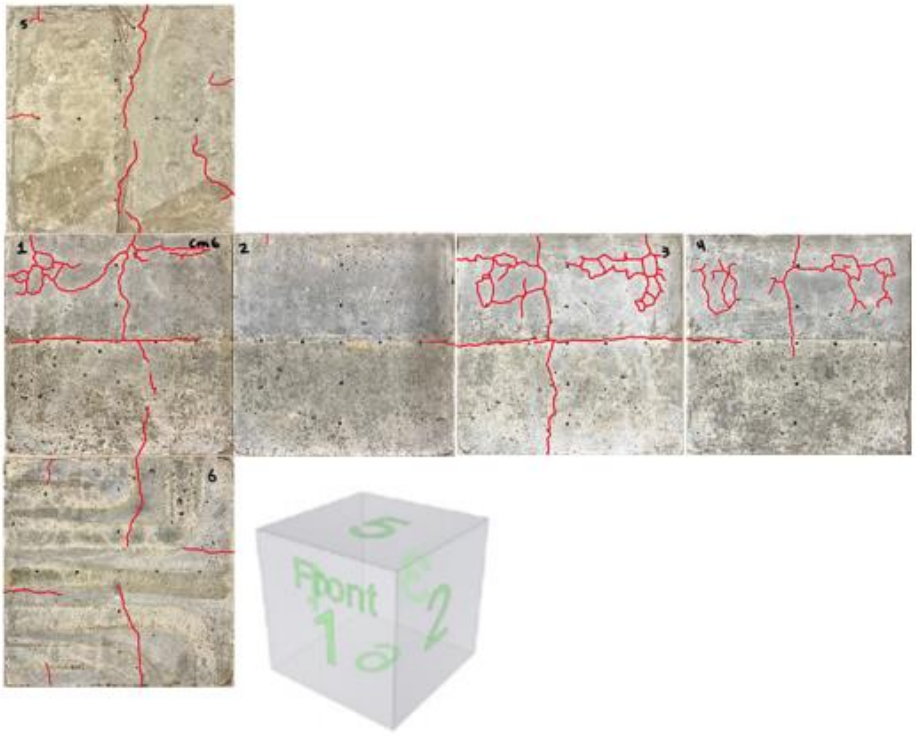

Figure 30: (a) Dry block: Con 7 and (b) Saturated block: Con 6 specimen after LN submersion. These specimens had embedded thermocouples, therefore had a weakness in the middle that fractured across Face 1, 2, 3, and 4.

Selected specimens were scanned using an X-ray CT (Toshiba Medical Scanner). The scanner has a resolution with a voxel size of 0.5 mm. Thus, the CT images can only be used to detect major fractures. The saturated specimens showed more features than the dry specimens. The CT images show that there are more fractures near the outer surfaces than the inside of the saturated specimens. X-ray slices, as seen in Figure 31 and 32, show that cracks distributed near the exposed surfaces diminish as they move toward the inside of the block. The CT slices of the dry specimen reveal fractures that begin from the faces and grow into the specimen towards the center of the block. As the specimens warmed to room temperature, the fractures created by cryogenic stimulation tended to close. Therefore, no apparent self-propping mechanisms were found in our laboratory-sized experiments.

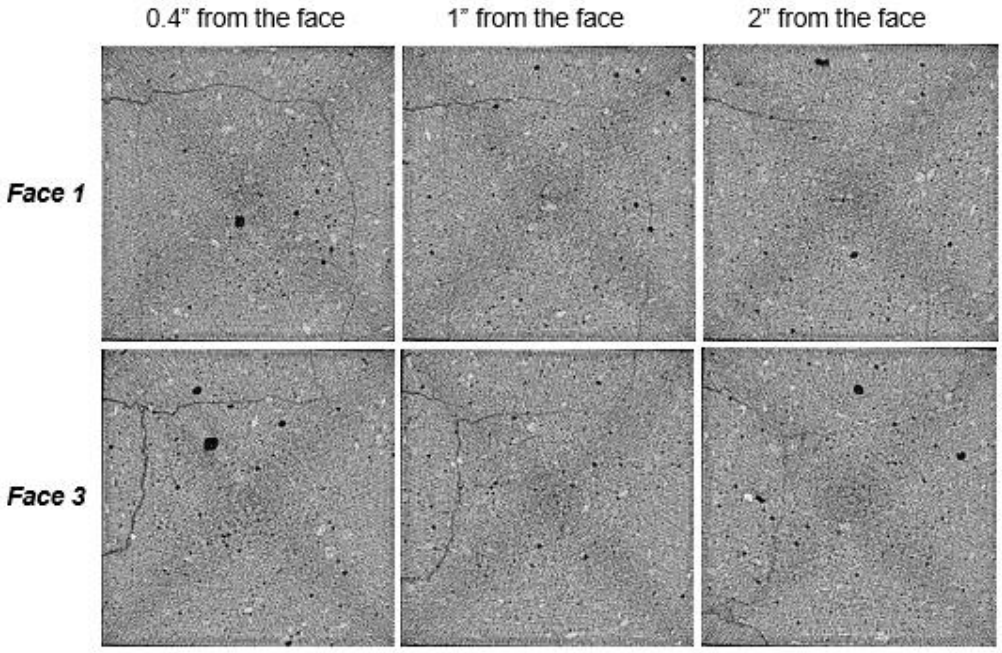

(a)

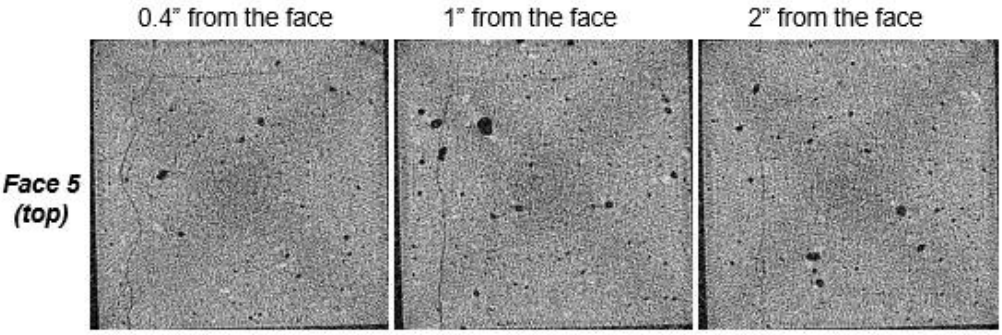

(b)

Figure 31: The CT slices of saturated (a) Con 1 and (b) Con 2 at 0.4", 1", and 2" away from Face 1 (vertical side) and Face 3 (vertical side). Cracks appear as darker features on the images.

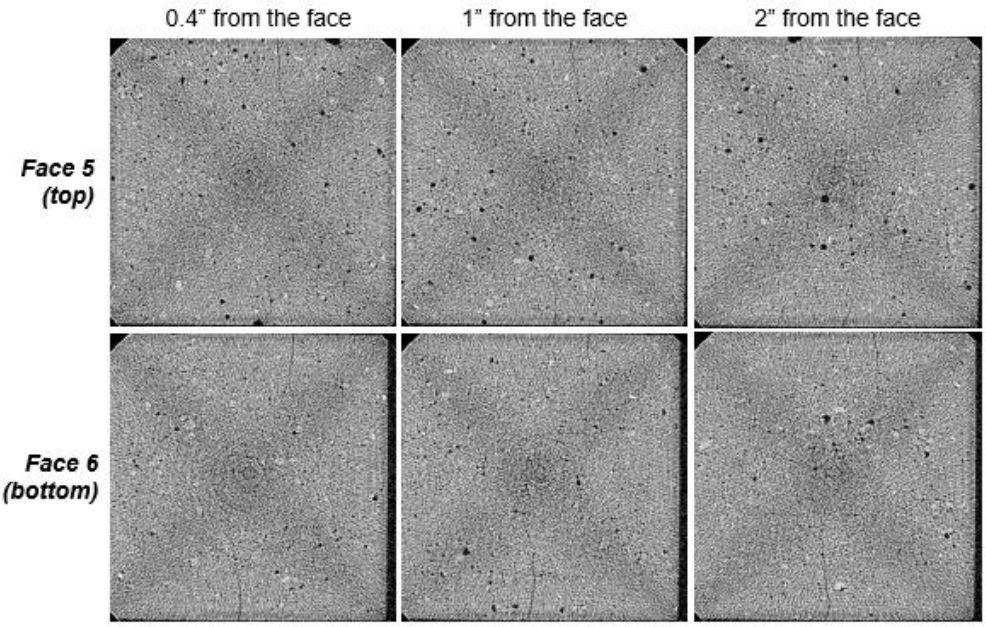

Figure 32: The CT slices of Con 7 (dry) at 0.4", 1", and 2" away from Face 5 (top) and Face 6 (bottom). Cracks appear as darker features on the images.

Acoustic measurements were taken before and after tests on specimen using P and S wave transducers. Saturated specimens that had acoustic measurements taken before testing were re-saturated to their initial weights before submerging in LN. The use of the vacuum pump and chamber was necessary for re-saturation. Acoustic signals were measured between Faces 1&3, Faces 2&4, and Faces 5&6 (faces opposite of each other). For each face set, the acoustic measurements were conducted at 9 locations (Figure 33). The differences in the acoustic measurements before and after cryogenic stimulation were examined, focusing on wave velocities and amplitudes. In Figure 34, the S-wave signals show acoustic signal arrival times for dry and saturated specimens. At most measurement locations, arrivals were delayed after cryogenic stimulation, which means that the wave velocity decreased as a result of the cryogenic stimulation. We can also see that wave amplitudes reduced significantly after the stimulation, which is typical of cracked material (except for Location 6 on Figure 34a.). The changes in S-wave velocities for

dry and saturated concrete specimens are represented in Figure 35. As mentioned earlier, the characteristic of acoustic signatures corresponds to the density of the surface cracks. The wave velocities of all specimens decreased after liquid nitrogen submersion. However, the saturated specimens' velocities proved to have higher percent reduction than the dry specimens, with 20-21% compared to 1.7-4.4%, respectively. This was expected, as the saturated specimens resulted in a greater amount of surface fractures from LN submersion than the dry specimens. We observed that acoustic velocities decreased significantly in areas where fractures were the most prominent. For example, the velocities at sensor locations #1, 2, 6, and 9 reduced significantly in Con 6 (Figure 35b). From Figure 30a., it can be seen that these sensor locations had prominent fractures. On the other hand, at the area below the weakness line that was the least cracked on Face 1 (sensor location #4 and 5) the acoustic velocity remained relatively unchanged. The acoustic velocity plot for Con 7 (dry) also follows this pattern, where larger decreases in velocity occurs at areas of fracturing (Figure 35a).

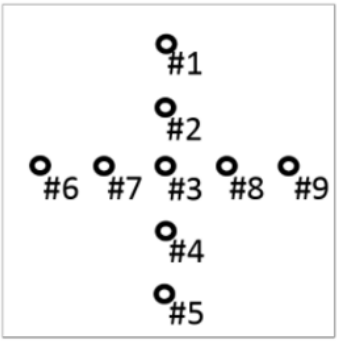

Figure 33: Location of acoustic measurement before and after LN submersion.

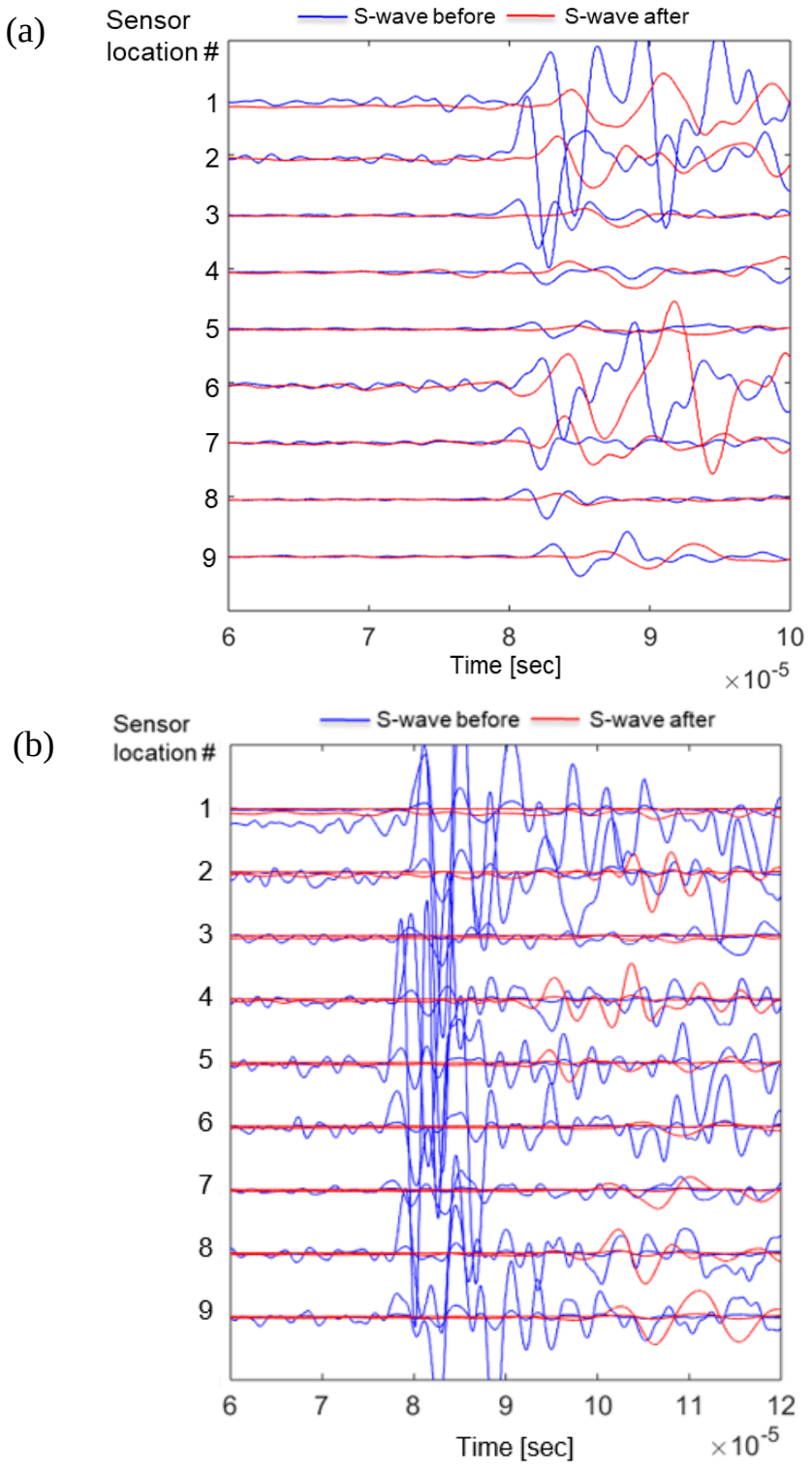

Figure 34: (a) Con Y-24 (dry) and (b) Con 6 (saturated) S-wave signals near arrivals between Faces 1 and 3 before and after thermal shock.

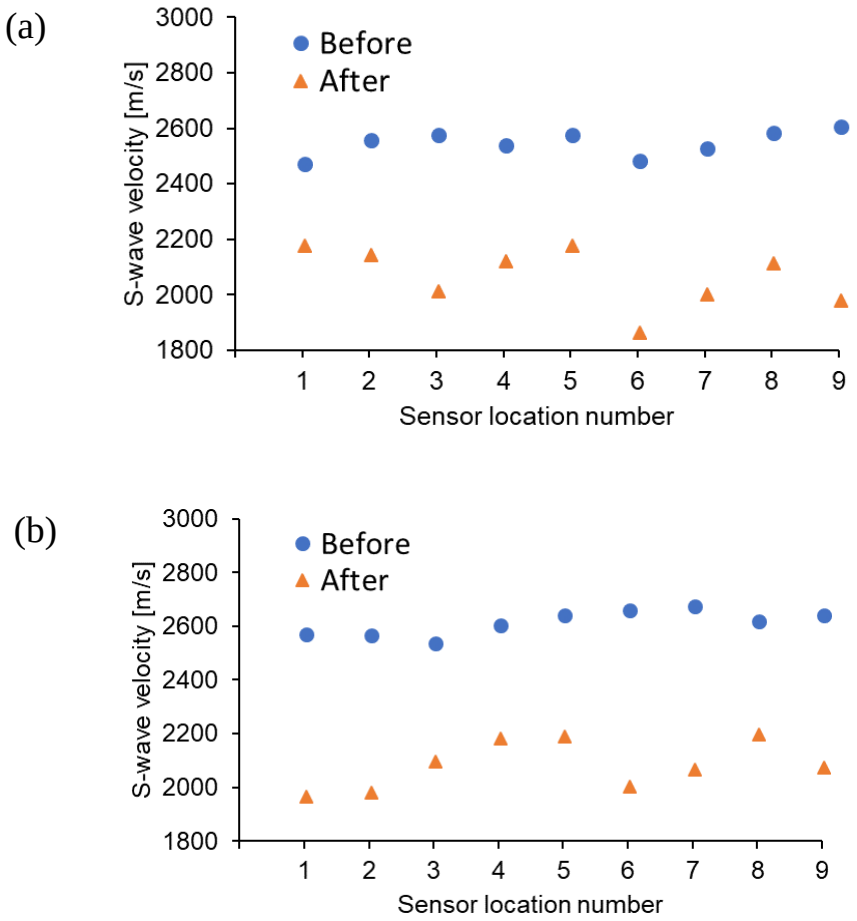

Figure 35: Changes in S-wave velocities before and after thermal shocks. (a) Dry specimen: Con 7, Face 1 and 3. (b) Saturated specimen: Con 6, Face 1 and 3.

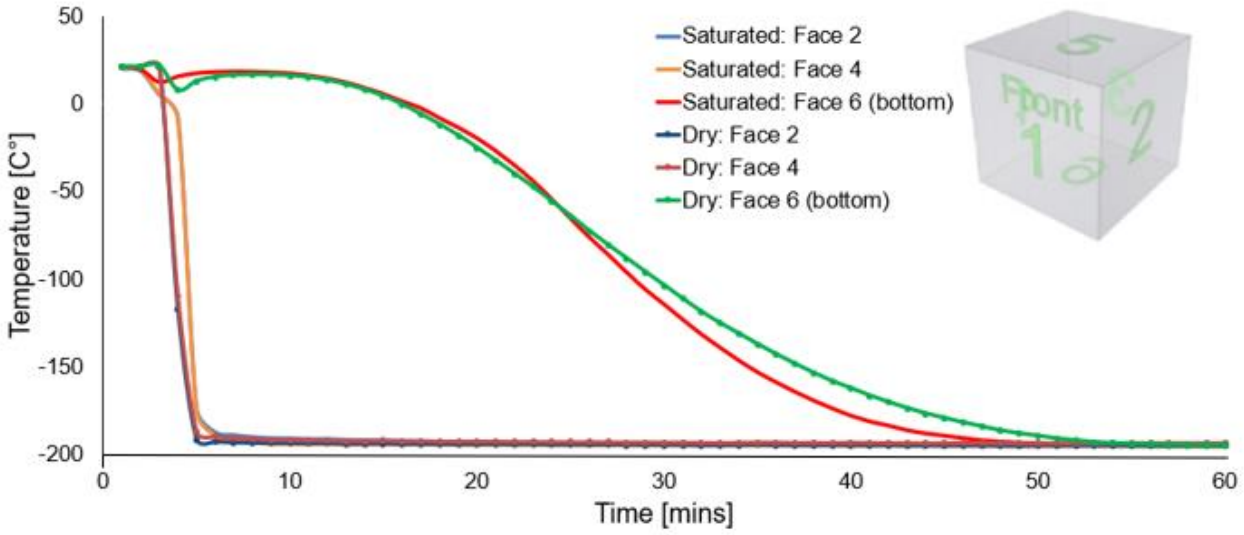

Figure 36: Surface temperature with time during submersion - Con 5 (saturated) and Con Y-29 (dry).

In Figure 36, the steep change of temperatures seen at ~5 minute mark is the moment when the specimen was placed in the container with LN. The saturated specimen and the dry specimen have similar surface temperatures over time. The temperature at the bottom of the specimen dropped at a slower rate compared to the sides because the bottom side was in direct contact with the Styrofoam container (Figure 36). This limited the LN access. We also compared temperature measurements between saturated and dry specimens with embedded thermocouples (Figure 37 and 38). The embedded thermocouples closest to the LN interface with the specimen edge (#2 and #8) dropped quicker in temperature compared to the TCs located near the middle of the specimen (#5). The embedded thermocouples allow us to visualize the thermal gradient of the specimens when they are submerged. The extremely low temperature is conducted through the surface to the inside of the block until the specimen reaches thermal equilibrium (-195.8 °C). It is observed that both reach thermal equilibrium at nearly the same time (Figure 39). However, the temperature change

of the saturated vs the dry specimens follow slightly different paths over time. For example, the saturated specimen initially drops in temperature faster than the dry specimen. This is likely due to instant ice formation when the saturated specimen encounters LN. After the saturated specimen reaches a certain point, the dry specimen begins to drop in temperature faster than the saturated until they both reach thermal equilibrium (Figure 39).

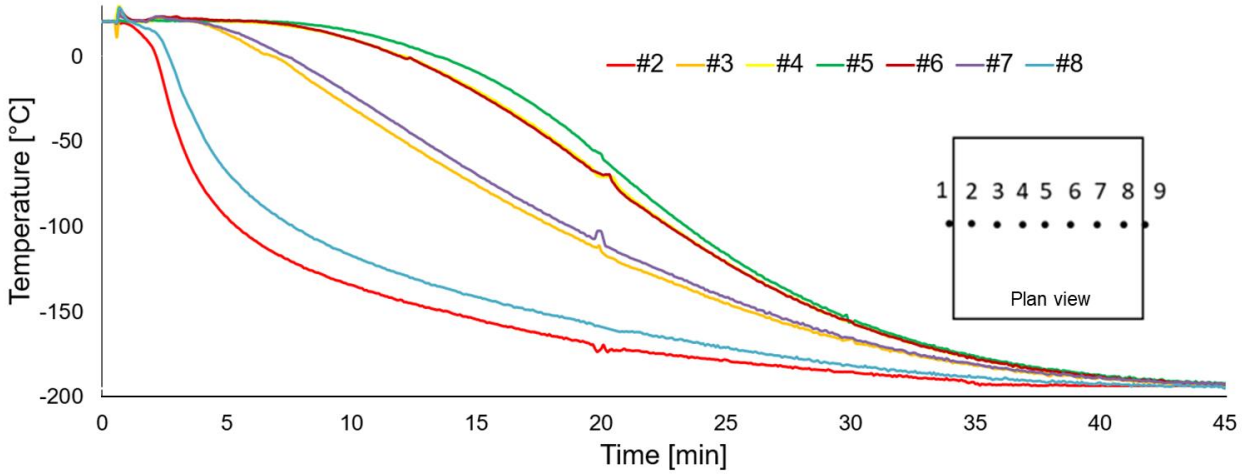

Figure 37: Temperature with time during submersion - Con 6 (saturated) - embedded thermocouples.

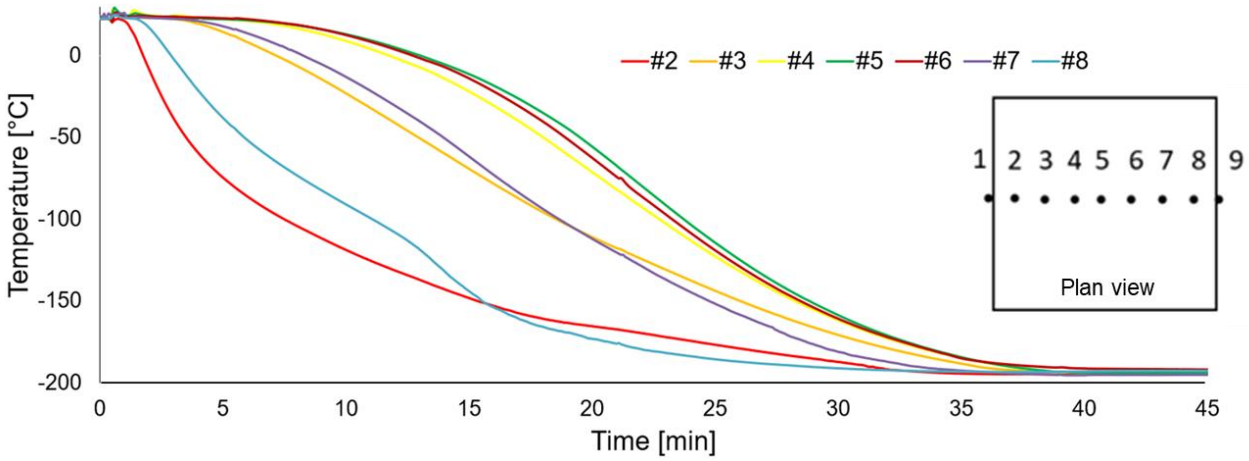

Figure 38: Temperature with time during submersion - Con 7 (dry) - embedded thermocouples.

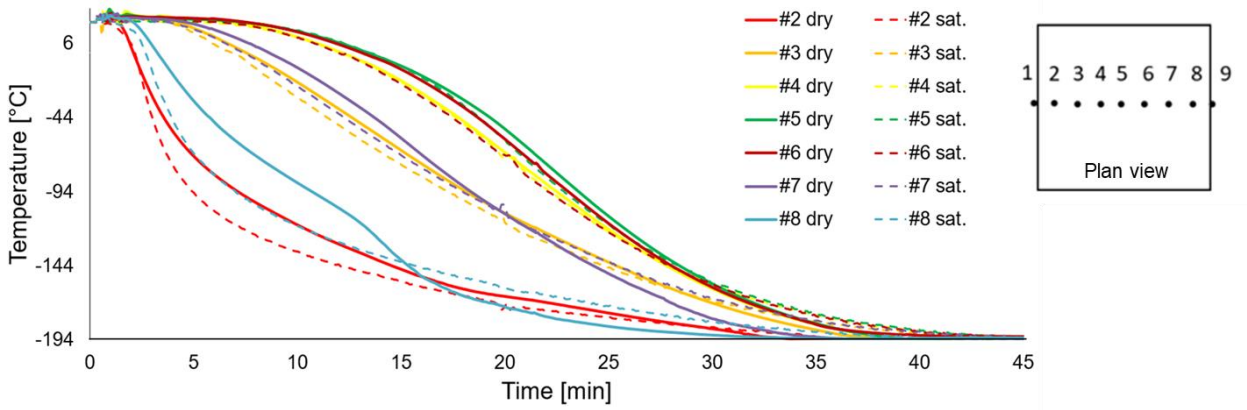

Figure 39: Temperature with time during submersion - comparison of Con 6 (saturated) and Con 7 (dry) - embedded thermocouples.

3.3 Discussion

The thermal calculations in Table 9 were obtained using the same equations for the sandstone cores in Chapter II. All concrete specimens were assumed to have a porosity of 20%. From this table, the specimens saturated with water are calculated to have a higher effective thermal conductivity than the dry specimens. However, the water-saturated specimens have a lower effective thermal diffusivity value than the dry specimens. On the other hand, the ice-saturated specimens are calculated to have a higher effective thermal conductivity and diffusivity value than the dry specimens. The ice-saturated specimens also have larger values of maximum thermal stress than the dry specimens. Therefore, the saturated specimens should be able to withstand the effects of thermal shock more than the dry specimens. However, in our experiments we find that this is not the case.

Table 9: Thermal properties of concrete specimens.

	Effective thermal conductivity [W/(m·K)]	Density [kg/m^3]	Effective c_p [J/(kg·K)]	Effective thermal diffusivity [m^2/s]	Effective α [/K]	$\sigma^{\Delta T}_{max}$ [MPa]
Dry concrete	0.24	2035	912.8	1.28×10^{-7}	1.3×10^{-5}	96.06
Saturated concrete (water)	0.35	2148	1548.8	1.05×10^{-7}		
Saturated concrete (ice)	0.67	2148	1122.8	2.8×10^{-7}	2.1×10^{-5}	152.2

The full submersion experiment was conducted with both dry and saturated 8″ cubic specimens. If a specimen is not saturated with water and does not have the effect of ice, fractures are located away from the edges and form perpendicular to the surfaces. In the saturated submersion tests, large fractures occurred near edges of the concrete, parallel to the exposed surface. The outer layer of the saturated specimens expanded laterally, causing shear fractures to occur parallel to the exposed surface. There are also many smaller cracks that seem to grow to the center of the surfaces from the edges and form a polygonal network. This is in qualitative agreement with previous recognition and observation of cryogenic fracture patterns (Grundmann et al. 1998).

The dry specimens had hardly any new visible crack formation, but the small cracks that did form were mostly on the top (Face 5) of the block. This may be because when concrete begins to set during curing, water rises to the top of the block, which causes the top of the block to have a higher porosity and areas of weakness. Con 7 (dry) specimen experienced the most surface damage out of all dry specimens due to the weakness line. From Figure 30b., Con 7 (dry; embedded

TC specimen) has a different fracture network from those of the normal saturated specimens. Major fractures were created and grew along the weakness line (the horizontal center) of Face 1, 2, 3, and 4. This creation of fractures along the center changed stress distribution and effected the fracturing geometry.

The specimens were scanned using an X-ray CT machine. CT images show that there are more fractures near the outer surfaces than the inside of the specimen. Cracks distributed near the exposed surfaces diminish as they move toward the inside of the specimen. Embedded TC measurements for saturated specimen Con 6, (Figure 37) show that the inside of the specimen requires more time to reach LN temperature (-195.8 °C); this drives fractures forming near the edges of the outer surface. Due to the nature of the submersion test, no fractures were initiated from inside. The effective thermal diffusivity value calculated for saturated specimens with ice was larger than the dry specimens. This is reflected in Figure 39 comparing the two specimens' embedded temperature measurements, where the saturated specimen initially drops in temperature faster than the dry specimen. As submersion continues there reaches a point where the dry specimen begins to drop in temperature faster than the saturated, caused by the outer layer of ice on the saturated specimen inhibiting nitrogen pressure into the specimen. This may explain why the saturated specimen does not have fractures propagating into the block as far as the dry specimen. However, we must keep in mind that the specimens with embedded thermocouples have a weakness line in the middle. One specimen having a wider weakness line than the other could also be the cause of the temperature pattern we see here.

In short, the dry specimen has more fractures that propagate away from the block edges towards the center of the block than the saturated specimens, whose large fractures were created near the edges. This is illustrated in the CT images in Figure 31 and 32. The outer layer of the

saturated specimen experienced lateral expansion, resulting in shear fractures parallel to the exposed surfaces (Figure 40) (Kneafsey et al. 2011). The dry specimen does not have ice, therefore it experienced tensile fractures due to contraction.

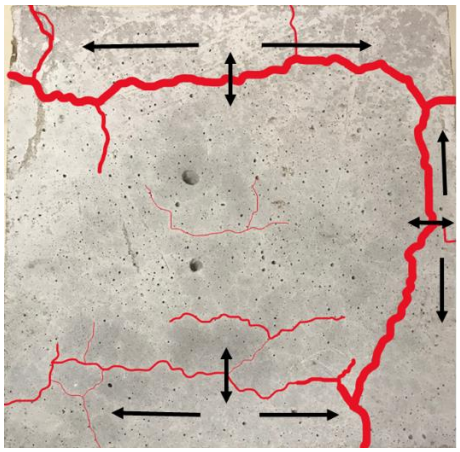

Figure 40: Fractures created by the expansion of ice matrix (Con 1, Face 4).

Simple calculations were done on the concrete blocks to investigate the overall volume change of saturated specimens. The volumetric thermal expansion of concrete, α_{Vcon}, is 36×10^{-6}/K. Assuming α_{Vcon} is constant throughout the temperature range, and ΔT = 200 K, the volume reduction due to a cryogenic temperature change would be:

Mineral phase volume reduction (%) = $\Delta T \cdot \alpha_Q \cdot 100$ (%) = 0.72

The volume of water increases by 9% upon phase change to ice. Assuming the porosity of concrete is 20%, the overall resulting volume change becomes:

Overall volume change of ice (%) = 9%·n
Overall volume change of mineral phase = volume reduction· (1- n)

Overall volume change (%) = (9%·n) – (volume reduction· (1- n))

At room temperature, the coefficient of thermal expansion (CTE) of concrete depends on the composition of the mixture and its moisture content at the time of the temperature change (Kogbara et al. 2013). It is known that the CTE of concrete is the resultant of the CTE of hydrated cement paste and the aggregate used. The linear CTE of hydrated cement paste is higher than the CTE of aggregates, such as sandstone (Table 10). This difference in CTE may have destructive effects on the concrete formation due to dramatic changes in temperature gradients. Dry and high water-content concrete is a complex composite consisting of aggregates, cement paste, pore liquid, interfaces, and ice. The different CTE of the various phases that are present during cryogenic fracturing may lead to the development of interfacial stresses, which may in turn cause cracking (Kogbara et al. 2013). However, there is inadequate information on this subject at cryogenic temperatures in the literature.

Table 10: Typical linear thermal expansion coefficient for common Portland cement concrete components at ambient temperature. Source: US FHWA (2011)

Concrete Components	Coefficient of linear thermal expansion (10^{-6} /°K)
Sandstone	11-12
Cement paste: water content 50%	18-20
Cement paste: water content 60%	18-20
Concrete	13

With the information above, it is assumed that the overall volume change of the saturated concrete block will not be uniform throughout the experiment. There might be other complicating factors such as movement of water molecules within and outside the block during submersion. However, the movement of water molecules within the block to the outside will be negligible because the surface water is immediately frozen upon LN submersion.

3.4 Conclusions

Liquid nitrogen submersion tests were performed using large 8″ cubic blocks of concrete. To test the ability of liquid nitrogen to create fractures, fracture assessments were made by visual inspection, X-ray CT, and acoustic signatures. The amplitudes and velocities of acoustic waves were sensitive to rock properties, and thus were able to identify changes in properties that were not visible. CT images identified spatial distribution of major cracks and allowed us to identify fracture patterns inside the concrete blocks. Measurement of temperature data on the surface and embedded in the specimens gave us opportunity to monitor the efficiency of the heat transfer process during submersion.

Con 6 (saturated) and Con 7 (dry) both contained embedded thermocouples. The temperature data obtained from these specimens concluded that saturated specimens drop in temperature quicker than dry specimens, due to the formation of ice. However, there is an uncertainty in how similar the weakness lines are between these two specimens. Further tests should be investigated to test the validity of this observation.

The cryogenic stimulations conducted in this study were able to create fractures in the rock block and alter rock properties. Fractures were created by creating a strong thermal gradient in a concrete block submerged in LN. Saturated specimens had a higher percent of fractures than the dry, even though the dry specimens were weaker from air-curing. This proves the mechanism of ice expansion significantly induced fracturing. CT images prove that fracturing occurs on the surface of the blocks and cracks diminishes towards the center. Due to the varying thermal expansion coefficient for saturated concrete specimens, both contraction and expansion of the rock property occurs resulting in different patterns of fractures. This includes both tensile fractures, seen in saturated Con 6 and shear fractures, seen in saturated Con 2. Both Con 6 and Con 2 also

produced smaller fractures that formed polygonal patterns which extended from major fractures. This is useful for the application of cryogenic fracturing for reservoir stimulation.

CHAPTER IV

LIQUID NITROGEN FLOW THROUGH BOREHOLE IN AN UNCONFINED SPECIMEN

Previous laboratory studies from Grundmann et al. (1998), Cha et al. (2018) and McDaniel, Grundmann et al. (1997) showed that cryogenic stimulation can create fractures in dry wellbore conditions. However, the effects of water in the pore space of rock formation has not been investigated for wellbores subjected to liquid nitrogen. In this chapter, we conducted laboratory experiments of cryogenic stimulation in saturated specimens to observe the effects of pore water on the physical phenomena associated with cryogenic fracturing in unconfined borehole.

Liquid nitrogen was flowed through boreholes in unconfined concrete and 8″ Berea Upper Grey sandstone cubes. Fracturing by thermal shock depends on thermal gradient around the borehole and the resulting tensile fracturing, therefore the thermal gradient was maximized by flowing LN continuously through the borehole. LN stimulation lasted for 45-50 minutes. Photographs and CT images of specimens were taken for fracture characterization. Acoustic measurements were taken before and after stimulation to characterize micro-fractures that were visible or not visible through images. We were also able to use a Seek Thermal Imager for Android to video record temperature changes throughout the specimen during stimulation.

4.1 Experimental Methods

4.1.1 Specimens

Concrete and sandstone blocks were tested in the unconfined state (no effective confining stress). The concrete specimens were prepared with a water to cement ratio of 0.55, and sand to cement ratio of 2.5. The cement was poured into an 8″ × 8″ × 8″ mold and sealed in a plastic bag. After

24 hours, the seal and mold were removed, and the concrete was either cured underwater for over 30 days or was open-air cured. A list of concrete specimens and their curing information is in Table 11.

Table 11: Curing conditions of tested concrete specimens (UW is underwater; OA is open-air). Specimen denoted with a "Y" were made in previous years.

Concrete specimens	Curing conditions
Con 8	Underwater 60 days
Con Y-9	UW 72 days, OA 23 months, UW 18 days
Con Y-10	UW 72 days, OA 23 months, UW 8 days

The Con. 8 specimen was cured with thermocouples embedded halfway into the 8″ concrete cube. In this case, the 8″ × 8″ × 8″ mold was first filled halfway (4 inches) with fresh mortar and seven thermocouples were inserted 0.5 inches deep (Figure 25, Chapter III). The cement was sealed in a plastic bag and left to harden for 6 hours before filling the remaining space in the mold. The mold was then sealed again and after 24 hours, was removed from the concrete and cured underwater for over 30 days. The concrete specimen that were cured underwater were only taken out to record acoustic measurements before LN stimulation and were re-saturated to their initial saturated weights by subjecting it in a vacuum chamber. For example, saturated Con. 8 was taken out of the water for borehole drilling and to record acoustic measurements. Afterwards, it was re-saturated to its initial saturated weight. Specimens that were open-air cured were placed in a vacuum chamber with water and pumped with vacuum until saturation was achieved by weight stabilization (Figure 41). Note that specimens cured underwater typically have a higher strength than open-air cured specimens.

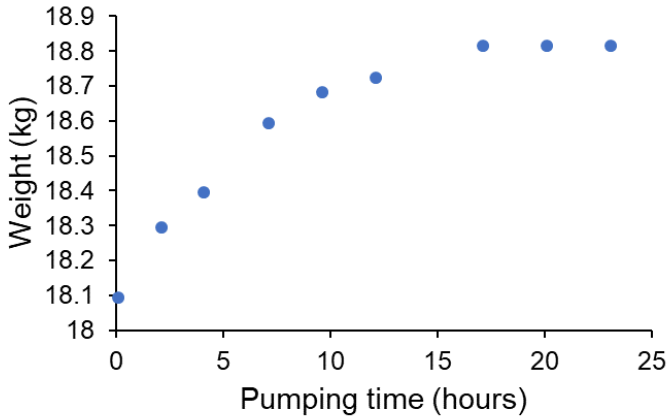

Figure 41: Weight stabilization of Con Y-10 during saturation process. After weight of specimen has reached a crest, it is considered saturated.

An array of thermocouples was embedded inside Con 8 to measure temperature propagation inside the specimen during thermal stimulation (Figure 44b). A boundary in the middle on Con 8 was visible where the mold was filled halfway (Figure 42).

Figure 42: Con 8 weakness line. Note the visible boundary where the concrete mold was filled halfway, and thermocouples were inserted.

The sandstone specimen was saturated by being submerged in 5 wt. % KCl brine water in the vacuum chamber until a constant weight was achieved. After it was saturated, we used Equation 1 to calculate the porosity of the Berea Upper Grey sandstone. Our results are shown in Table 12 below and compared with the values Kocurek Industries had provided.

Table 12: Permeability and porosity of Berea Upper Grey sandstone.

	Vendor's measurements	Our measurements
Permeability [k]	370-400 mD	
Porosity [ϕ]	20-22%	21.9%
P-wave velocity [m/s]		2204
S-wave velocity [m/s]		1498
Density [kg/m^3]		2182
Elastic modulus [GPa]		10.5
Shear modulus [GPa]		4.9
Constraint modulus [GPa]		10.6

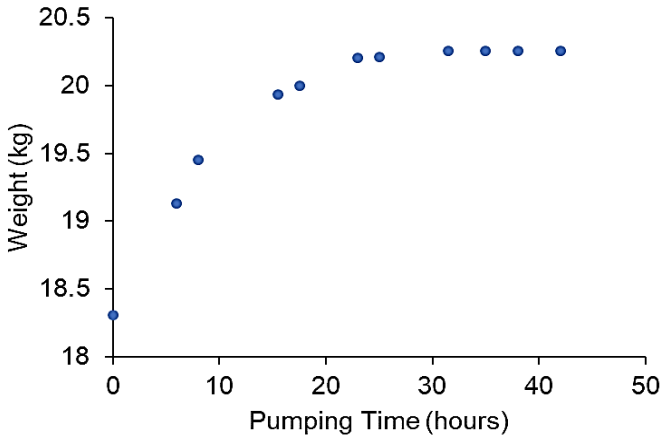

Figure 43: Weight stabilization of sandstone specimen using vacuum pump.

A 2.54-cm OD stainless steel tube used as a borehole casing was inserted 3.8 cm into the borehole (16.5 cm depth) and mounted to the borehole wall using J-B Weld steel reinforced epoxy to seal and resist fluid pressure. Before casing, thermocouple wires were inserted into borehole between casing and borehole walls (Figure 44a). The TC suspended in the borehole recorded temperature in borehole space and informed us of nitrogen phase state. The TC attached inside at the borehole wall measured the temperature at the borehole surface.

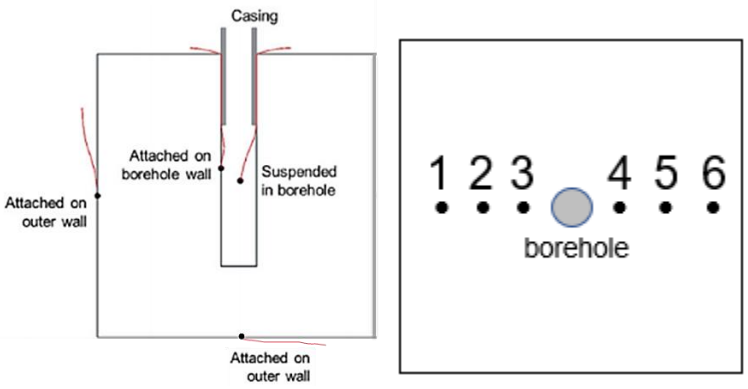

(a) (b)

Figure 44: (a) Locations of thermocouple tips on a test specimen. (b) Embedded thermocouple placement on Con 8.

4.1.2 Procedure

Fracturing by thermal shock depends on thermal gradient around the borehole and the resulting tensile stress. Cryogen needs to continuously flow through a borehole to quickly cool the borehole down and maximize the thermal gradient. Stagnant liquid nitrogen in the borehole would quickly boil and vaporize. Therefore, we cooled the borehole as rapidly as possible to maximize the thermal gradient by flowing liquid nitrogen continuously through the borehole.

From the liquid nitrogen dewar, LN was released by internal gas nitrogen pressure generated inside the dewar once an outlet was opened. The LN was transported through a cryogenic hose to the specimen and injected into the borehole through a stainless-steel casing mounted in the borehole and then directed to an outlet. Figure 46 shows the system where LN was flowed directly from the dewar to the specimen borehole and nitrogen gas flows out though an outlet.

The equipment used for borehole stimulation allows effective LN flow through a coaxial inlet and outlet, as seen in Figure 45. Cryogen enters the borehole through the central smaller-diameter inlet tubing (blue line and arrows in Figure 45), which passes through a larger cross-shaped fitting.

Nitrogen exits through the annulus between the inlet tubing and the casing, and then through the space in the cross fitting.

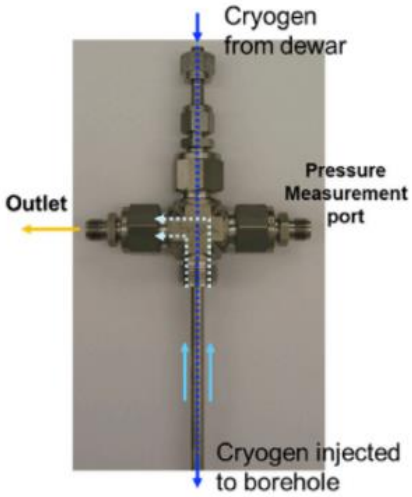

Figure 45: Apparatus that allowed coaxial cryogen flow through the borehole. Reprinted from Cha et al. 2014.

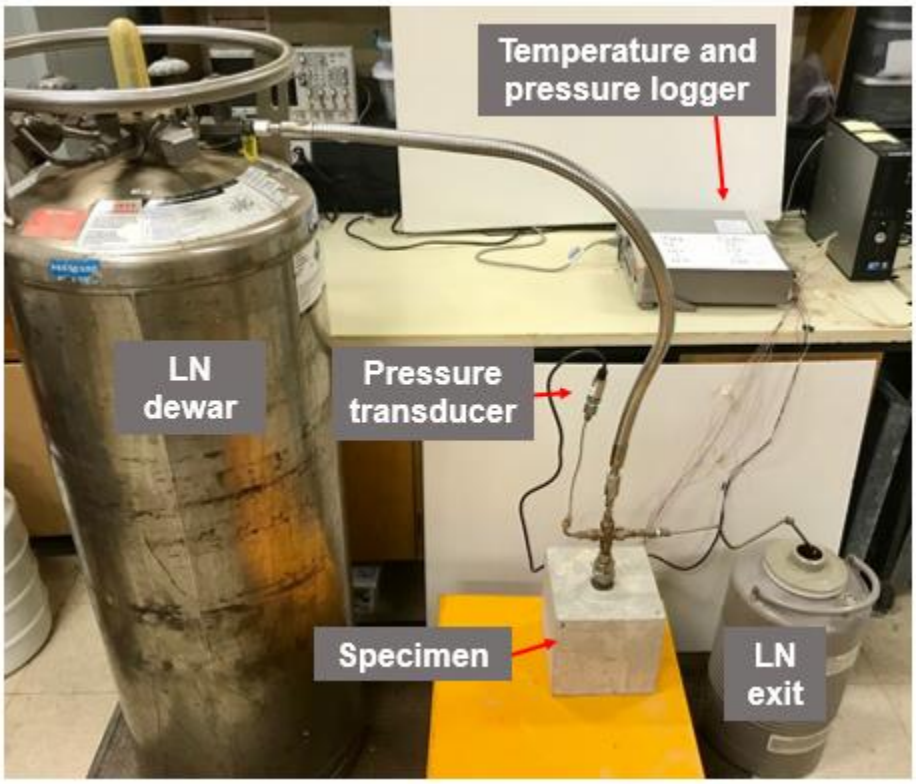

Figure 46: The experimental setup for borehole stimulation of unconfined specimens.

Fluid pressure in the borehole was measured throughout the experiment to monitor the system behavior to control flow rate and for safety. To measure borehole pressure, a regular 100 psi pressure transducer attached to the end of a vertical standoff pipe connected to the flow line (Figure 46). There is no flow in the standoff pipe, and a stagnant vapor cushion is created that prevents the cold temperature from affecting the sensor. The maximum pressure in the dewar is 22 psi or 0.15 MPa.

4.1.3 Fracture Characterization

Fracture development was characterized with photographs and X-ray CT inspection using a Toshiba Medical CT Scanner. The scanner has a coarse resolution with a voxel size of 0.5 mm. Thus, the CT images can only be used to detect major fracture aperture. A list of the specimens tested, and the measurements taken in each test is provided in Table 13.

The characteristics of acoustic waves propagating through a medium depend on the mechanical properties of the medium (Cha et al. 2009). The wave velocity in jointed rock masses is a function of the density of cracks, or joint spacing as modeled by:

$$V_s = \sqrt{\frac{G_{eq}}{\rho}} = \sqrt{\frac{1}{\rho}\left(\frac{k_S S G}{k_S S + G}\right)}$$

where V_S is shear wave velocity, k_S is shear joint stiffness, G is shear modulus of intact part, ρ is rock mass density, and S is joint spacing. When intact rock properties, density, and joint stiffness remain the same, the acoustic wave velocity can be used to characterize crack generation. The high frequency content is filtered when acoustic waves propagate through cracked media (Cha et al. 2014). Acoustic measurements before and after tests were taken on specimens using P and S

ultrasonic transducers. The differences in the acoustic signatures before and after cryogenic stimulation were then examined, focusing on P and S wave velocities and amplitudes.

Table 13: List of experiments for borehole cryogenic stimulation (thermal shock).

Saturated specimens	Curing conditions	Measurements	Cryogen in the container (amount)	Flow duration (min)
Con 8	Underwater 60 days	T, embedded T, P, acoustic (before, after)	~15 L	15
Con Y-9	UW 72 days, OA 23 months, UW 18 days	T, P, acoustic (before, after)	27 L	45
Con Y-10	UW 72 days, OA 23 months, UW 8 days	T, P, acoustic (before, after)	27 L	40
Sandstone		T, P, acoustic (before, after)	30 L	50

*T and P represent temperature and pressure, respectively.

4.2 Observations and Results

4.2.1 Unconfined borehole tests: Concrete

Before submersion, no specimens had visible surface cracks. After submersion of saturated concrete blocks, many large surface fractures and small cracks were generated and visible on the surface (Figure 47 and 48). The block surfaces started to form frost once the temperature of the surface fell below the water-freezing point. The frost is first noticed close to the steel borehole casing on the top (Face 5) about 25 minutes into the test. Stainless steel has a higher thermal diffusivity than concrete, so the temperature is transferred at a faster rate to the top of the specimen. The frost then formed on the sides as fractures were created on Faces 1-4.

(a)

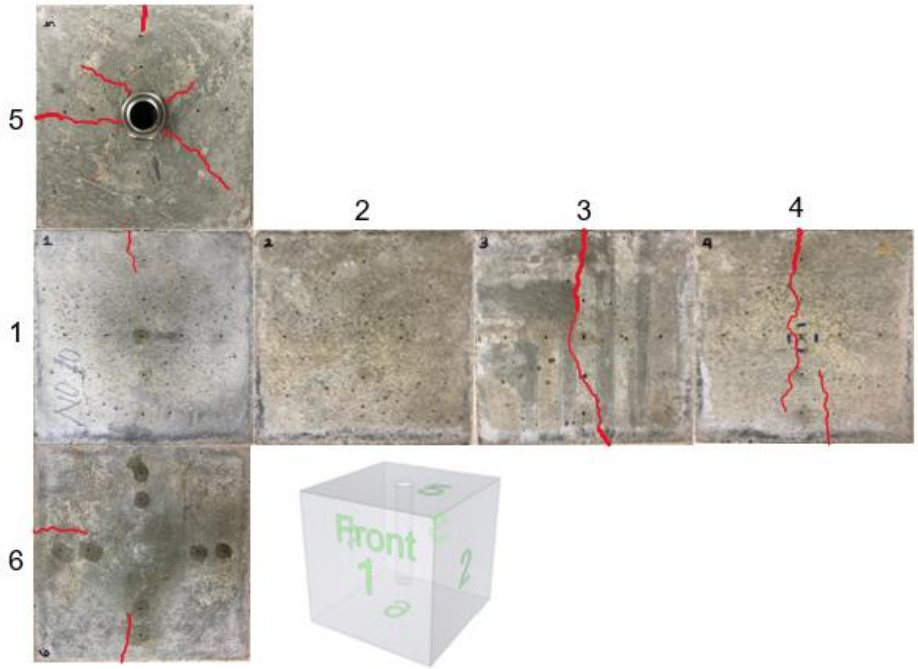

(b)

Figure 47: Con Y-10 specimen. Cracks observed after the thermal shock (a) on the surface and (b) at the bottom of the borehole.

(a)

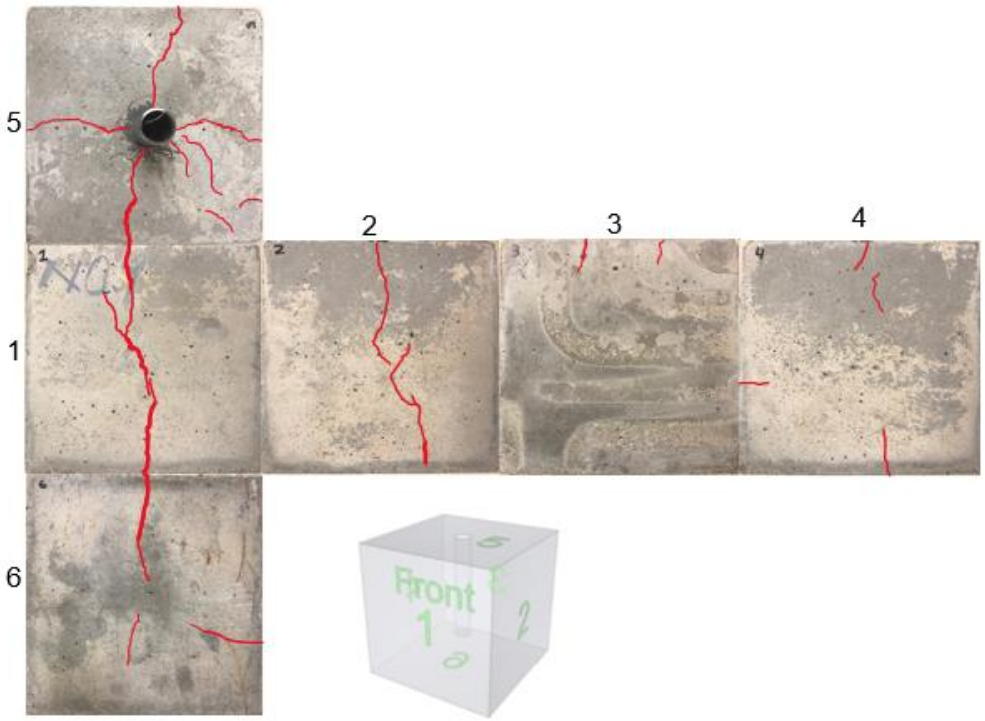

(b)

Figure 48: Con Y-9 specimen. Cracks observed after the thermal shock (a) on the surface and (b) at the bottom of the borehole.

Con 8 cracked in half through its curing boundary during testing. About 5 minutes into testing, a loud “pop” is heard and the specimen split in half through the horizontal. The top half is

seen detaching from the bottom (Figure 49). At this point, all the embedded thermocouples start to rapidly drop in temperature due to close contact with LN (Figure 51) and LN is observed pouring out from the weakness line. This splitting may have occurred due to the joint being weakened from our first attempts at testing when the coaxial was not working properly. However, we should note that our first attempt at LN stimulation only lasted 10-15 minutes and on our second attempt, it split in half in 5 minutes. That gives the impression that this specimen would not have remained solid for a 40-50-minute stimulation.

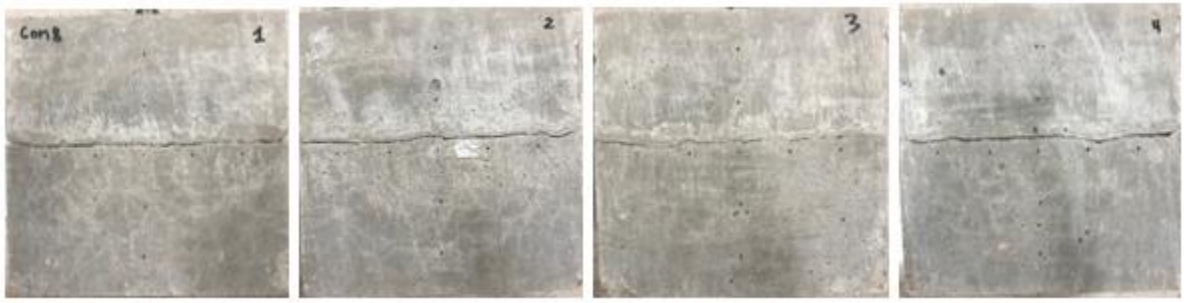

Figure 49: Major joint fracture is seen on Con 8 after stimulation. Notice the split is located at the curing boundary from molding. Blocks are held together by thermocouple wires but are in two separate pieces.

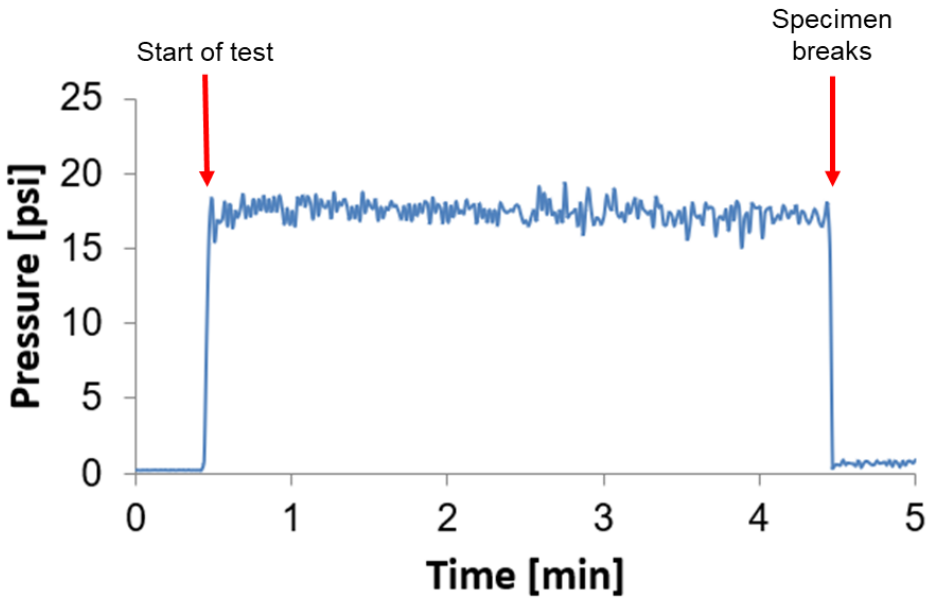

Figure 50: Pressure during LN stimulation in Con 8. Notice the dramatic drop in pressure when the specimen splits.

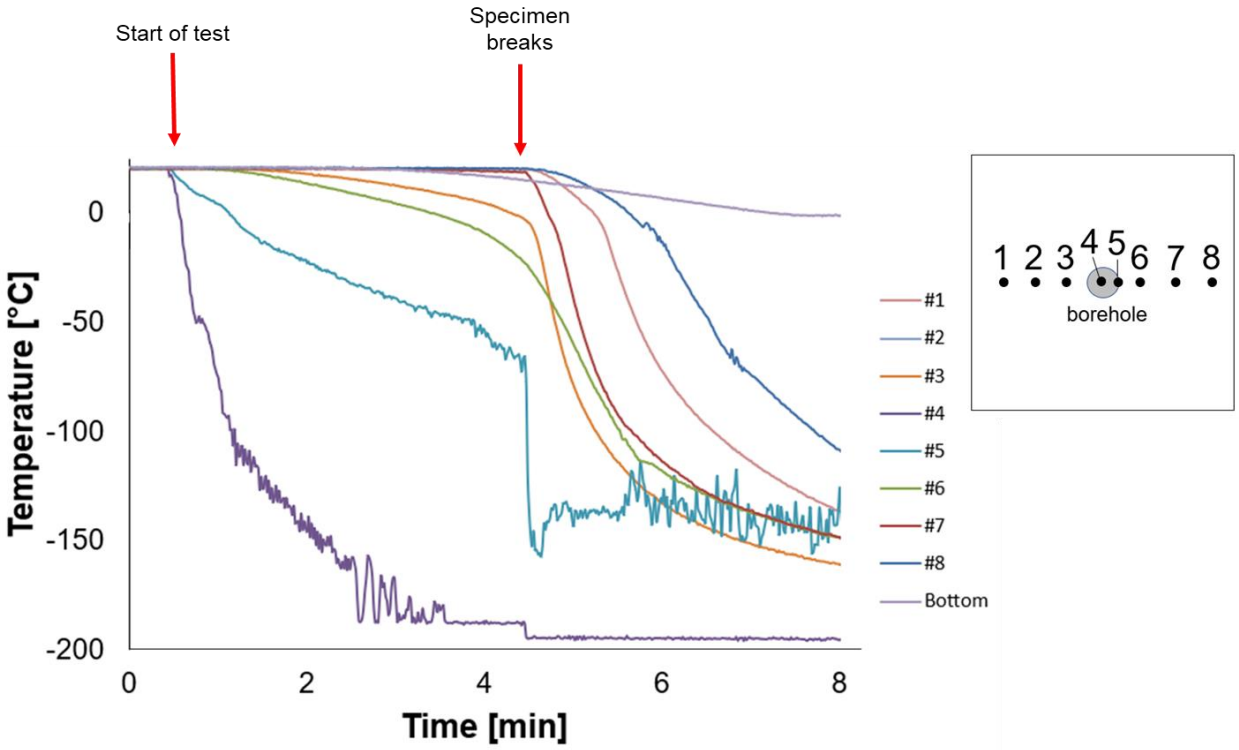

Figure 51: Temperature of Con 8. Notice the rapid drop in temperature of embedded thermocouples when the specimen split.

All specimens were scanned using an X-ray CT (Toshiba Medical Scanner). The scanner has a resolution with a voxel size of 0.5 mm. Thus, the CT images can only be used to detect major fracture aperture and cannot detect micro-fractures generated near the wellbore. The CT images show that there are more fractures near the outer surfaces than at the center of the saturated specimens. X-ray slices show that cracks distributed near the exposed surfaces diminish as they move toward the inside of the block (Figure 52 and 53).

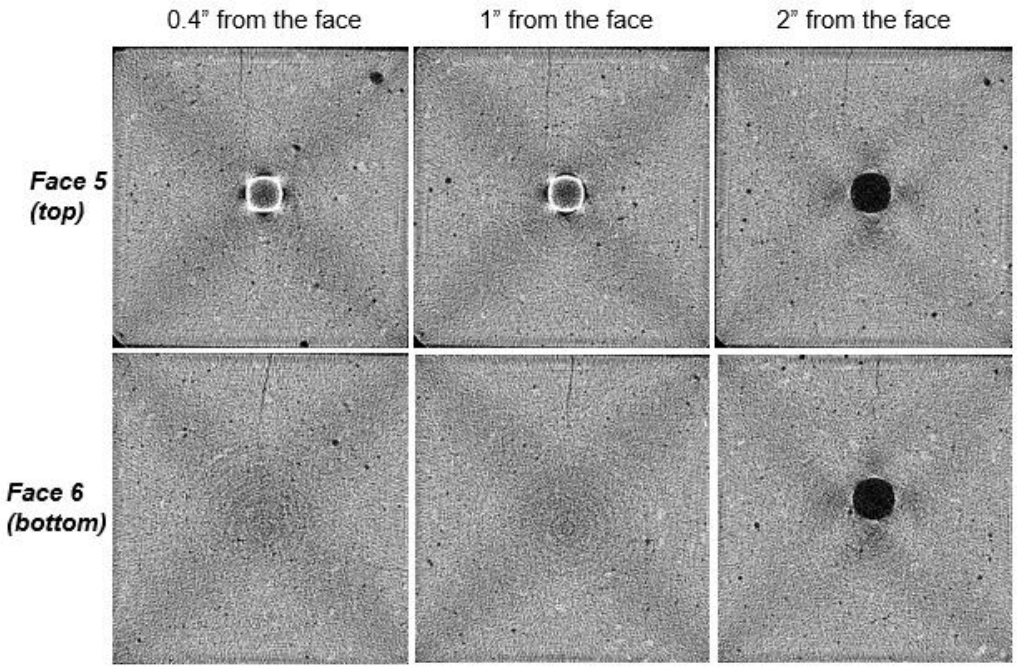

Figure 52: The CT slices of Con Y-9 after LN stimulation. Cracks appear as darker features on the images.

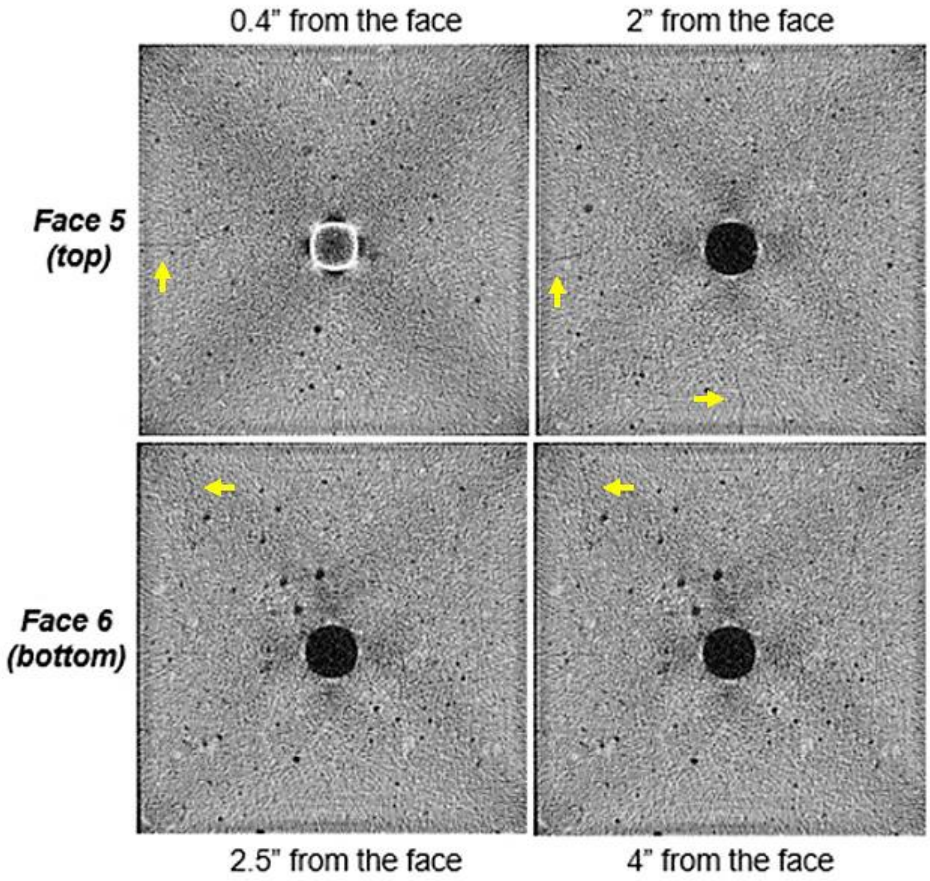

Figure 53: The CT slices of Con Y-10 after LN stimulation. Cracks appear as darker features on the images. White arrows are pointing to cracks.

Acoustic measurements before and after tests were taken on specimens using P and S wave transducers. Acoustic signals were measured between Faces 1&3, Faces 2&4, and Faces 5&6 (faces opposite of each other). For Face sets 1&3 and 2&4 (sides), the acoustic measurements were conducted at 9 locations; for Face set 5&6 (top and bottom), the acoustic measurements were conducted at 8 locations (Figure 54). The differences in the acoustic measurements before and after cryogenic stimulation were examined, focusing on P and S wave velocities and amplitudes. In Figure 55, the S-wave signals show arrival times. At most measurement locations, arrivals were delayed after cryogenic stimulation, which means that the wave velocity decreased as a result of the cryogenic stimulation. We can also see that wave amplitudes reduced significantly after

thermal shock (except for Location 5 and 9 on Con Y-10 on Figure 56a.). The exceptions of reduced amplitudes after thermal shock could be an effect of water saturation in the specimen during acoustic measurements. For example, Con Y-10 had acoustics measured when it was dry before stimulation and measured with some water saturation after stimulation. The changes in S-wave velocities for Con Y-10 and Y-9 are represented in Figure 56 and 57, respectively. The characteristic of acoustic signatures corresponds to the density of the surface cracks. The wave velocities of all specimens decreased after liquid nitrogen submersion. Larger decreases of wave velocities are observed in locations where waves were traveling perpendicular across surface fractures. From both Con Y-9 and Con Y-10, we see there is a pattern of location #4 and 5 on Face pairs 1-3, and 2-4 having the least reduction in acoustic velocity, and location #1, 2, and 3 having drastic reductions. From CT images, this is correlated to the pattern of fractures in the block, where there are more prominent fractures on the top half than the bottom half. The S-wave velocity of Con Y-9 decreased by 15%, and the P-wave velocity decreased by 9.5%. For Con Y-10, the S-wave velocity decreased by 7.8% and the P-wave velocity decreased by 1.1%. Con Y-10 experienced less fracturing; we expect that it had a stronger tensile strength.

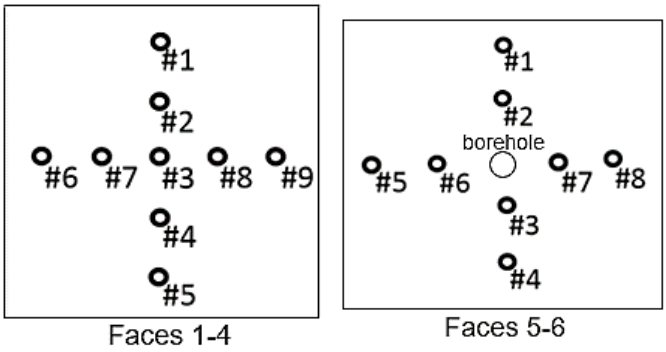

Figure 54: Acoustic measurement locations in specimens for unconfined borehole tests.

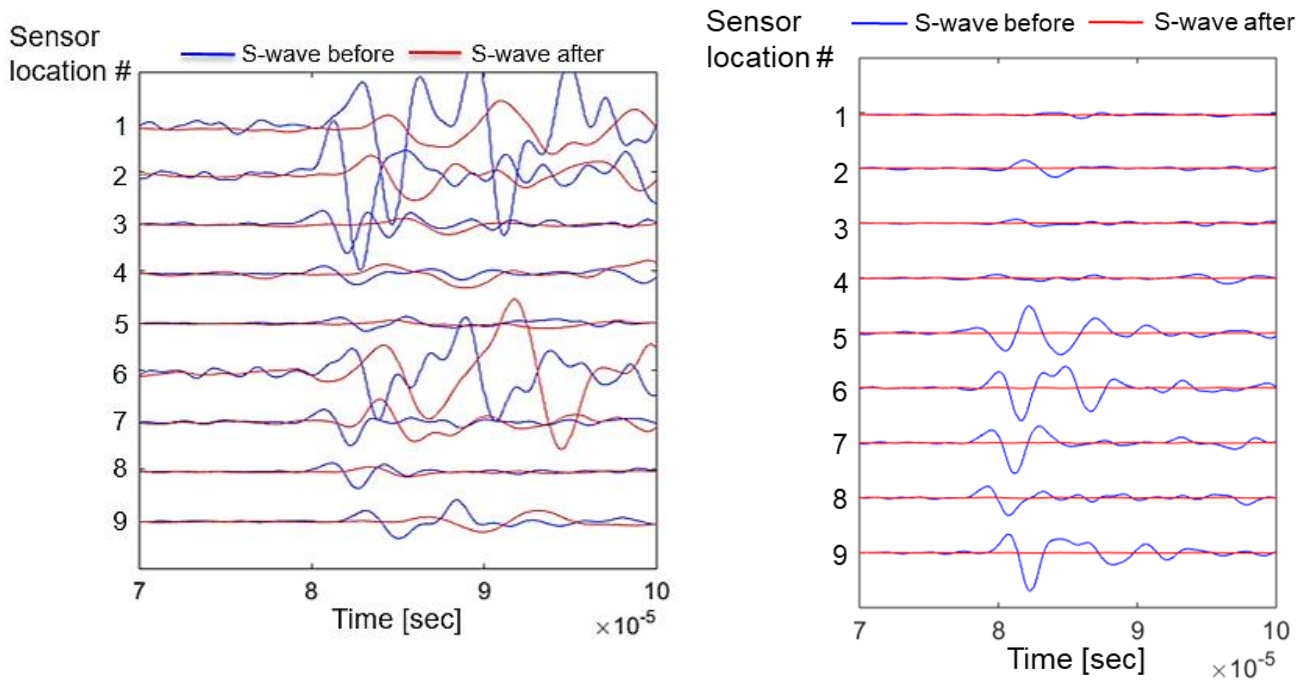

(a) (b)

Figure 55: (a) Con Y-10 S-wave signals near arrivals between Faces 2 and 4 before and after thermal shock. (b) Con Y-9 S-wave signals near arrivals between Faces 1 and 3 before and after thermal shock.

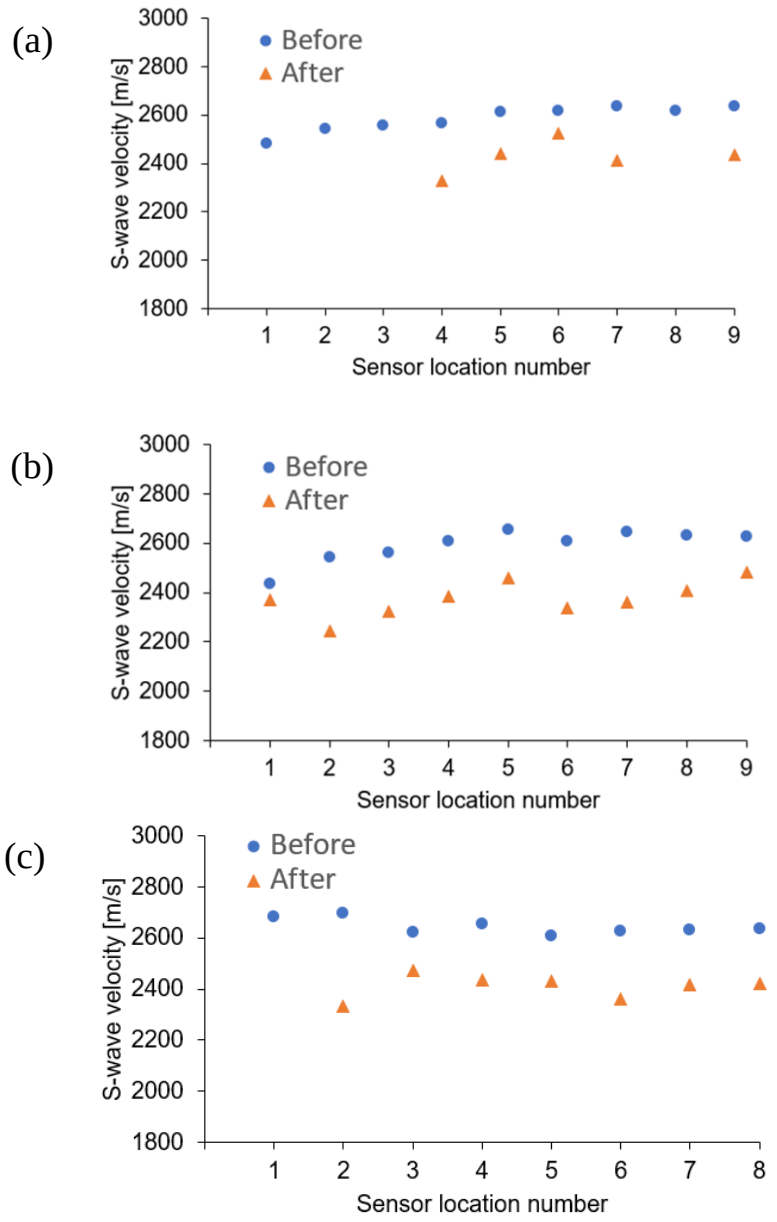

Figure 56: Changes in S-wave velocities before and after the thermal shocks for Con Y-10 concrete specimen. (a) Face 1-3, (b) Face 2-4, (c) Face 5-6.

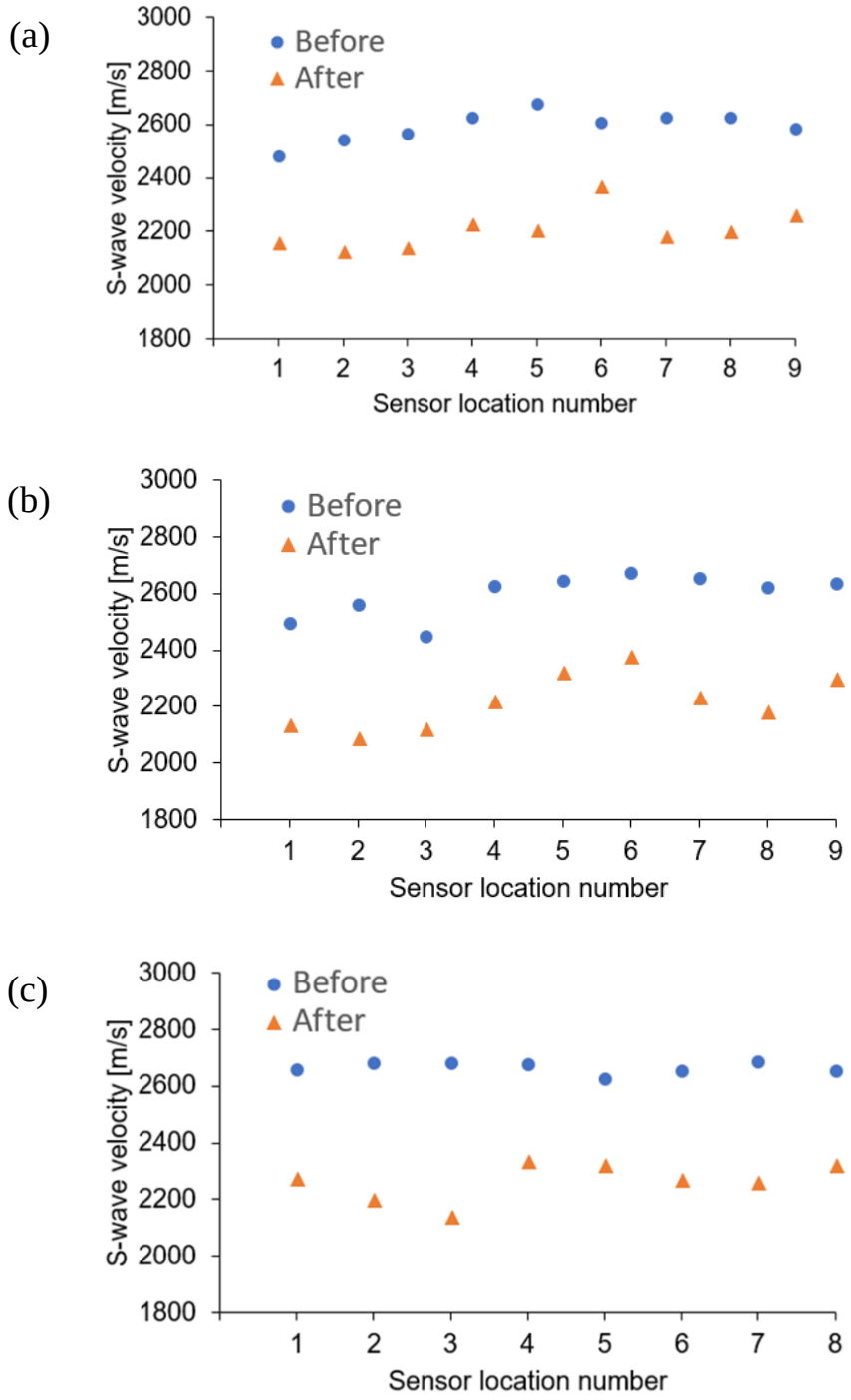

Figure 57: Changes in S-wave velocities before and after the thermal shocks for Con Y-9 concrete specimen. (a) Face 1-3, (b) Face 2-4, (c) Face 5-6.

The temperature measurements on Con Y-10 (Figure 58) shows that nitrogen was entering the borehole in the liquid phase for most of the time during LN flow. The inside of the borehole

wall reached -196.8 °C in about 2 minutes of stimulation. The cooling at the borehole wall was slower than the inside of the borehole due to the Leidenfrost effect. That is, due to a large temperature difference between the rock and the boiling point of the fluid, the LN immediately boils at near contact with the surface, creating a vapor cushion. The vapor cushion has a much lower thermal conductivity than the LN, and it delays the heat transfer to the rock surface. The bottom of the specimen drops in temperature faster than the side of the specimen because the bottom was closer in proximity (1.5 inches) to the borehole than the side of the specimen (3.5 inches).

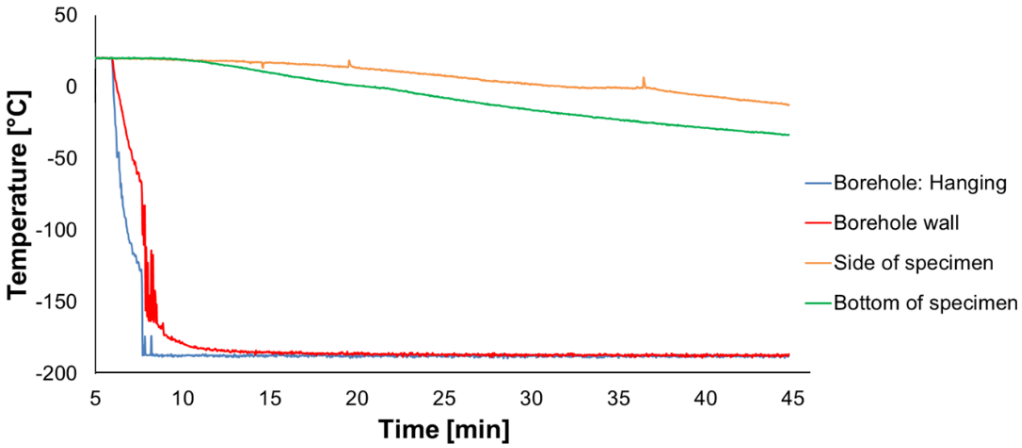

Figure 58: Con Y-10 temperature measurements during stimulation.

4.2.2 Unconfined borehole tests: Sandstone

Before testing, the sandstone specimen had no surface fractures. Once LN supply was turned on and transferred to the borehole, we observed that bubbling immediately started to occur on all faces of the specimen. Due to its high porosity, the injected nitrogen pressure began to build up

and pore water permeated to the surface of the block through the pores in the specimen (Figure 59).

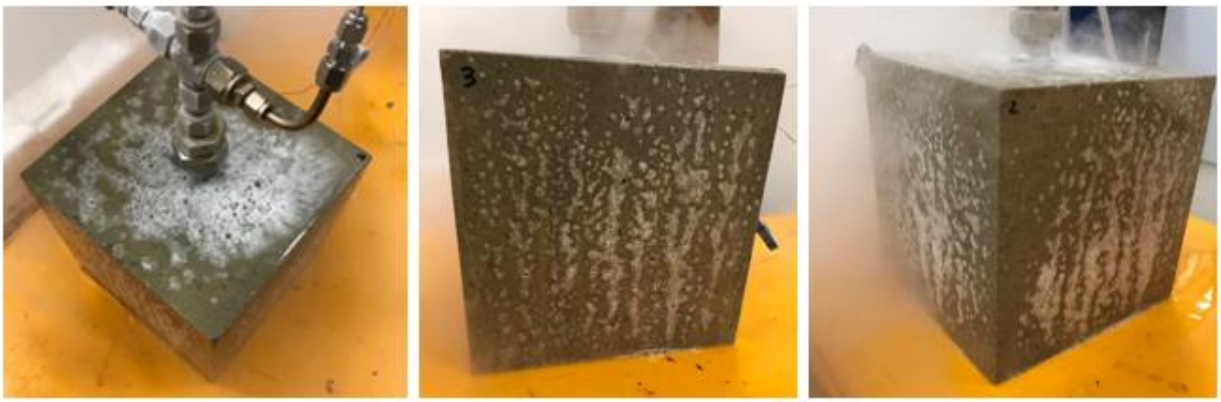

(a) (b) (c)

Figure 59: (a) Top (Face 5) and sides (b) Face 3, (c) Face 1 and 2 5 minutes into LN test. White bubbling on the surface represents areas of high permeability that allow water to be pushed out from LN injection.

After approximately 20 minutes of LN flow, frost begins to form on all faces of the specimen in the center. No fractures are seen forming during the test. As time proceeds, the frost begins to turn to ice on the surface and areas on the surface surrounding the ice formation are still observed to be bubbling (pushing water out). Following the formation pattern of the frost, ice formation begins in the center and moves towards the edges of all faces as time proceeds (Figure 60). This pattern may occur due to the faces being closer in proximity to the borehole than the edges are.

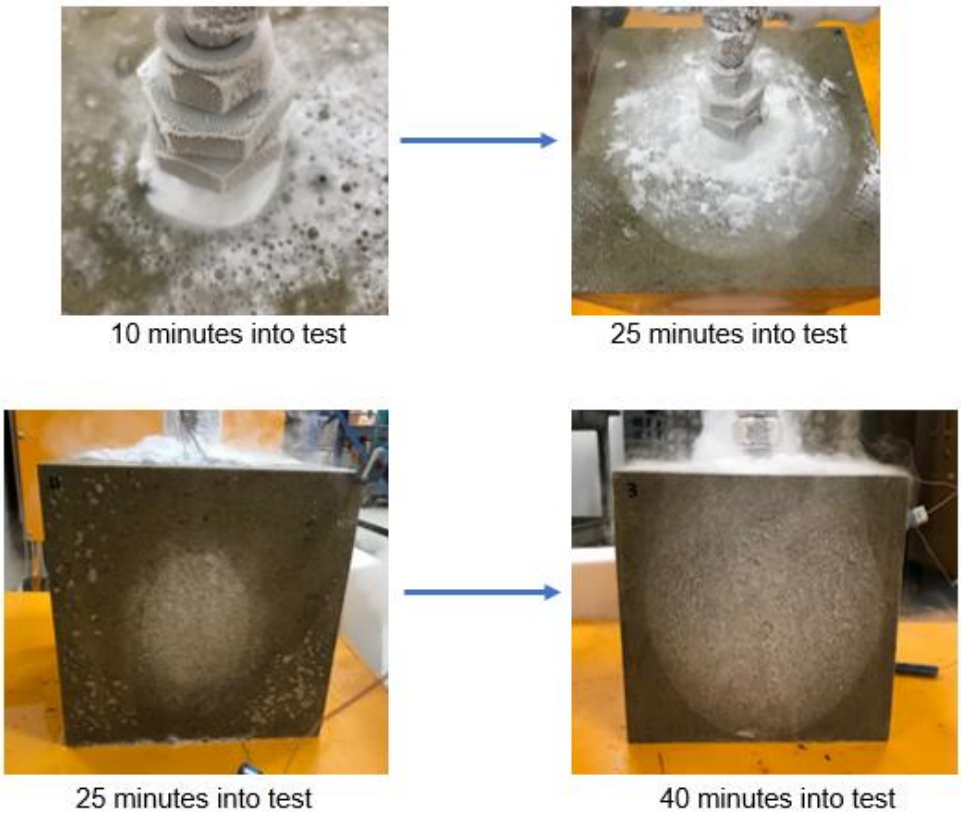

Figure 60: Ice formation expanding over time from the center of the Faces to the edges.

At 45 minutes into the stimulation, almost the entire surface area of the specimen was covered with ice. Yet, there were still no fractures seen on the surface. After 50 minutes, the test was stopped by turning LN supply off and then within 1 minute of the closure, we heard a loud "pop" and the specimen split in half vertically through Face 2 and 4 (Figure 61).

Figure 61: Sandstone block split in half after LN injection had stopped. The specimen was not moved before taking these photos.

From the temperature plot (Figure 62), the cooling at the borehole wall was slower than the inside of the borehole due the Leidenfrost effect. This is similarly seen in the unconfined concrete borehole tests. The bottom of the specimen initially decreased in temperature faster than the side of the specimen due to its proximity to the borehole. However, once the sides of the specimen (Face 1, 2, 3, and 4) began to have ice formation on their surfaces the TC measurements reflect a faster decrease in temperature on the side than the bottom surface. This is caused by the bottom not being able to form ice on its surface, as its interface with the metal plate base was too warm. The pressure inside the borehole fluctuated between about 14-18 psi in high frequency (Figure 63). Along with the temperature data (Figure 62), it may reflect complexities in phases and flow conditions through narrow flow path.

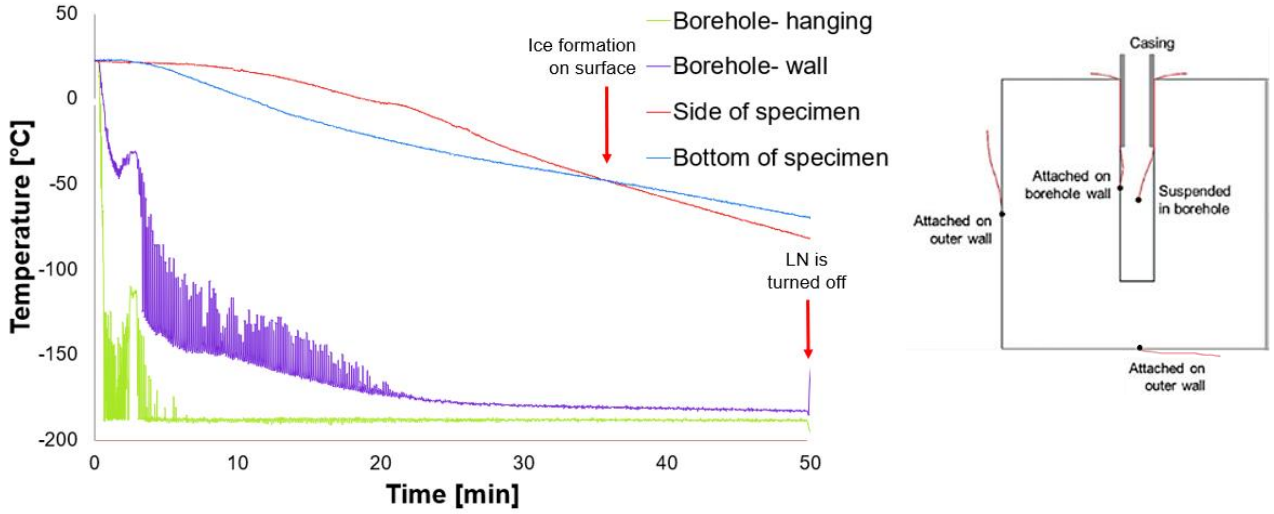

Figure 62: Temperature measurements during LN stimulation.

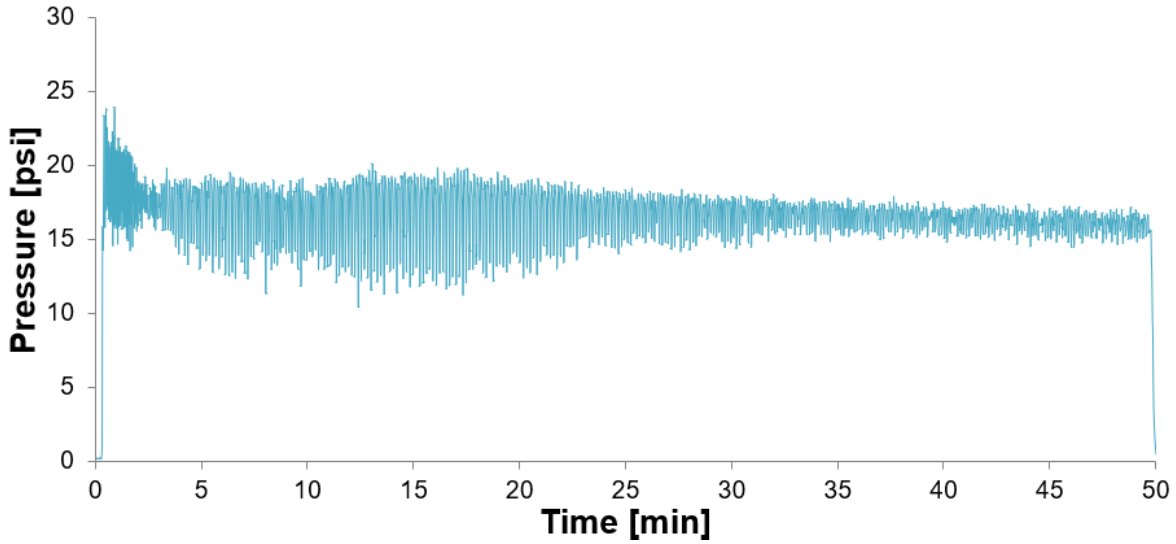

Figure 63: Pressure fluctuations inside borehole during LN flow through borehole. Less fluctuation towards the end of the test.

The specimen was scanned using an X-ray CT (Toshiba Medical Scanner). The scanner has a resolution with a voxel size of 0.5 mm, resulting in images that can only be used to detect major fractures. From Figure 64, the major fracture divides the specimen in half vertically from the top (Face 5) to the bottom (Face 6). A second fracture perpendicular from the fracture division

is also noticed from the bottom of the specimen in Figure 64. It becomes less prominent as we look further into the specimen.

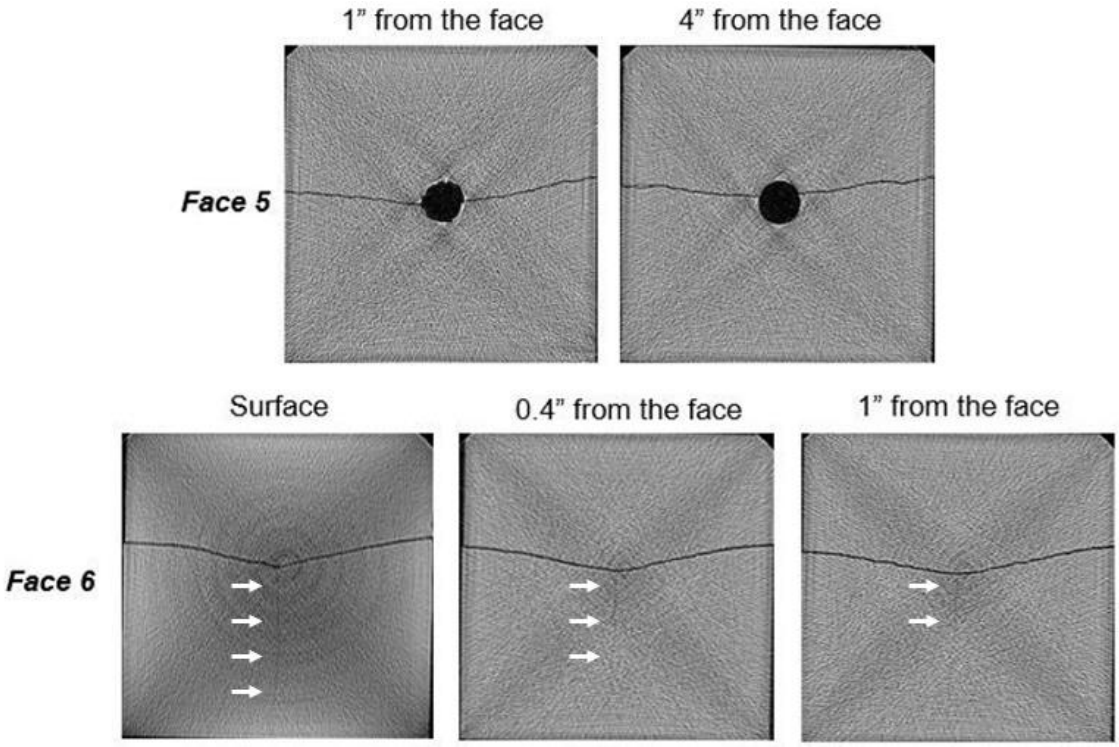

Figure 64: CT images of the sandstone specimen. Fractures appear as darker lines. Notice the fracture perpendicular to the large fracture that broke the specimen in half near the bottom (Face 6).

4.3 Discussion

4.3.1 Unconfined borehole tests: Concrete

Table 9 from Chapter III has the thermal properties of concrete specimens. All concrete specimens were assumed to have a porosity of 20%. From Table 9, the specimens saturated with water are calculated to have a higher effective thermal conductivity than the dry specimens. However, the water-saturated specimens have a lower effective thermal diffusivity value than the dry specimens. On the other hand, the ice-saturated specimens are calculated to have a higher effective thermal

conductivity and effective thermal diffusivity value than the dry specimens. The ice-saturated specimens also have larger values of maximum thermal stress than the dry specimens. Therefore, the saturated concrete should be able to withstand the effects of thermal shock more than the dry concrete. However, both dry and saturated concrete specimens have a tensile strength of 2.88 MPa (Table 2, Chapter II). The maximum thermal stress of the specimens is larger than their tensile strength, therefore fracturing was expected to occur in concrete specimens.

Pore water can influence rock damage through expansion when water changes to ice. If a majority of the pore space is filled with water, expansion of the water during freezing will generate stress. When the stress exceeds the tensile strength of the rock, cracking will occur. In our LN stimulation experiments, LN was injected into a borehole in saturated specimens. The inside of the specimen experiences the first effects of the thermal shock stimulation; this causes expansion inside the block. According to Figure 58, the borehole wall drops to -195.6 °C within 10 minutes, however, the outside faces of the specimen do not drastically drop in temperature. As the inside expands, the outside remains fairly warm and does not experience a quick transfer of thermal energy. Regardless, the tensile strength of the concrete cannot withstand the expansion from the center and we begin to observe fractures forming on the edge of the top (Face 5) and the side (Figure 65, left). The fracture begins to extend down Face 5 and a second fracture from the bottom begins to form and extend (Figure 65, middle). The two fractures extend from the edges of the Faces until they meet in the center (Figure 66, right). This “top-to-bottom” fracture pattern can be seen forming on the time-lapse below.

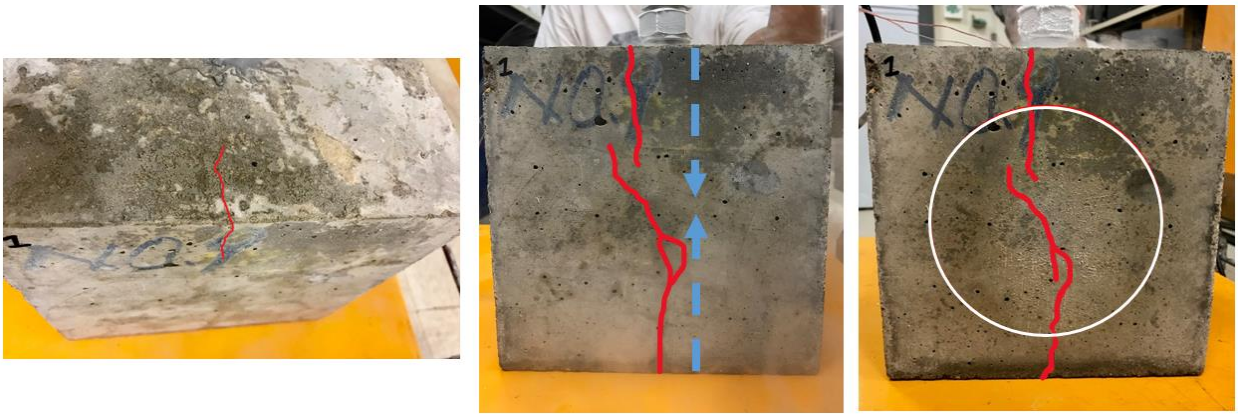

10 minutes into test 18 minutes into test 30 minutes into test

Figure 65: Fracture growth pattern from unconfined borehole test. Tensile fractures occur due to expansion inside the block. Frost growth on the surface is circled in red after 30 minutes of LN stimulation.

The surface of the specimen begins to form frost once the temperature of the surface drops below the water-freezing point. We notice that the frost first grows on the side Faces that have fractures running from the top to the bottom of the specimen (Figure 65, right). For example, Face 1 and 2 on Con Y-9 (Figure 48) or Face 3 and 4 on Con Y-10 (Figure 47). After one or two major fractures occurred on the side of the specimens, not much fracture growth continues on other Faces. This may be because after these first top-to-bottom fractures occur from the high tensile stress, enough tension is released to prevent further fracturing. One may then assume that the faces with top-to-bottom fractures have the weakest areas of tensile strength.

During the unconfined borehole test on Con Y-9, we used a thermal camera (Seek Thermal Imager) to video record temperature of the specimen. The camera revealed differences in temperature propagation for different sides of the specimen. The top of the specimen, for example, revealed lower temperatures at the borehole location. As time progressed, low temperature spread

wider over the top of the specimen (Figure 66). Note that the scale of color legend of the thermal camera changes as the temperature of objects in the camera's view changes.

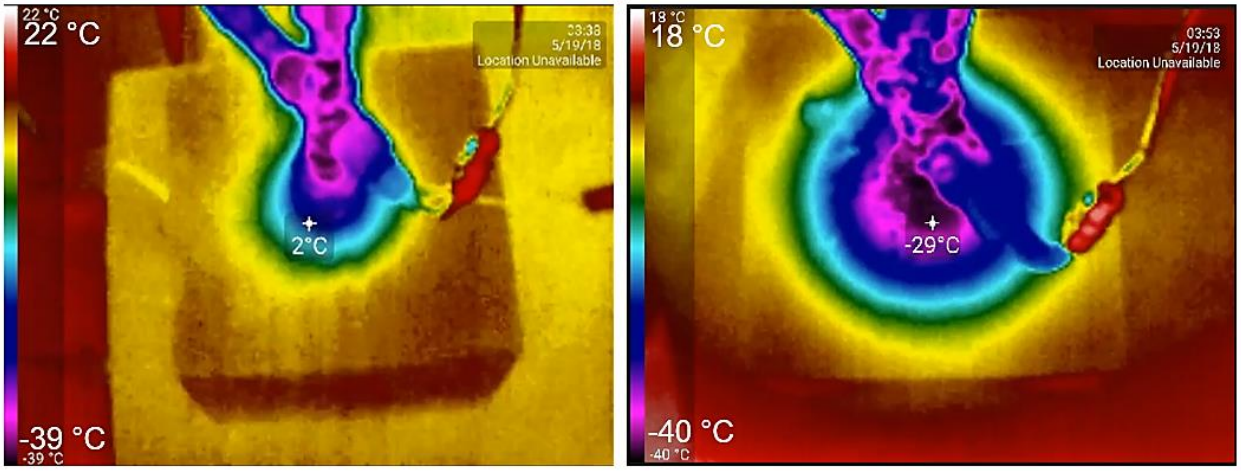

10 minutes into test 25 minutes into test

Figure 66: Thermal images of the top of Con Y-9. Color legend is on the left side of each image.

The thermal images also showed that fractures created might affect temperature throughout the specimen. In Figure 67 we compare thermal photos of Face 1, which experienced the growth of a top-to-bottom fracture, and Face 3, which experienced little fracturing on its surface.

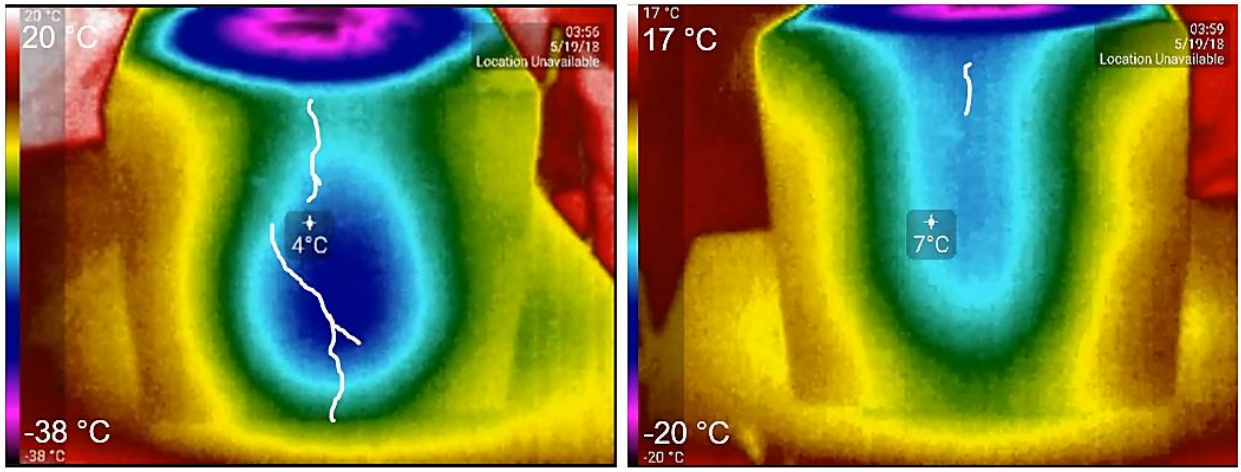

Face 1: 30 minutes into test Face 3: 30 minutes into test

Figure 67: Face 1 vs. Face 3 during stimulation. White lines are to denote the fractures on each Face. Note the scale bar for Face 1 is different from the scale bar for Face 3.

Recall from Figure 65 that 30 minutes into the test, Face 1 began to have frost accumulate on its surface in the center. The large tensile fracture on its surface might allow LN to permeate to the surface and form ice. The ice formation in the center of Face 1 also explains the circular pattern of the thermal image (Figure 68). On the other hand, Face 3 did not have frost on its surface due to the lack of fractures (Figure 69).

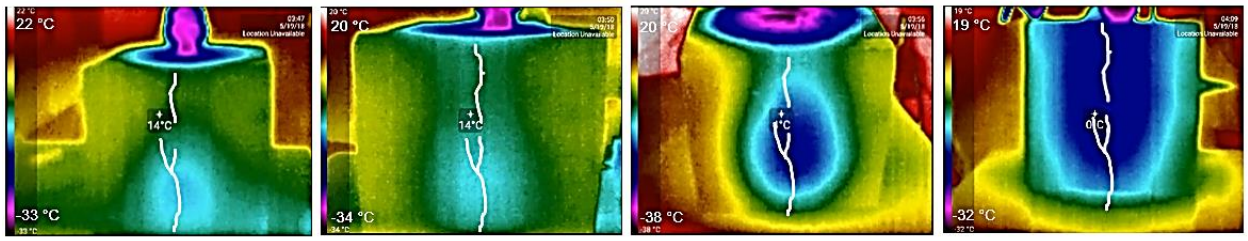

18 minutes into test 22 minutes into test 30 minutes into test 40 minutes into test

Figure 68: Con Y-9, Face 1 time-lapse of thermal images. White lines are fractures on the surface.

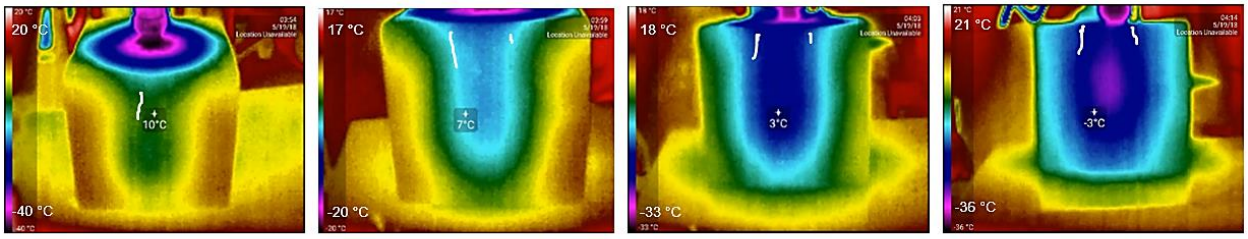

Figure 69: Con Y-9, Face 3 time-lapse of thermal images. White lines are fractures on the surface.

The presence of water in the specimen created tensile fractures on the outside of the specimen but did not produce fractures near the wellbore. The circumferential area around the borehole experienced water freezing. This inhibited gas nitrogen pressure into the formation and the inside of the specimen to expanded due to freezing, while the outside did not.

The freezing of the circumferential area surrounding the borehole led to more fractures forming on the outer surfaces of the block than inside the borehole, which is counter-intuitive to the goal of cryogenic fracturing in borehole conditions. A drawing of non-uniform expansion in unconfined saturated concrete blocks subjected to LN flow is provided in Figure 70a. Near-wellbores under high compressive forces may possibly cause breakouts depending on expansion and compression forces. A drawing of the in-field confining stresses is also provided in Figure 70b.

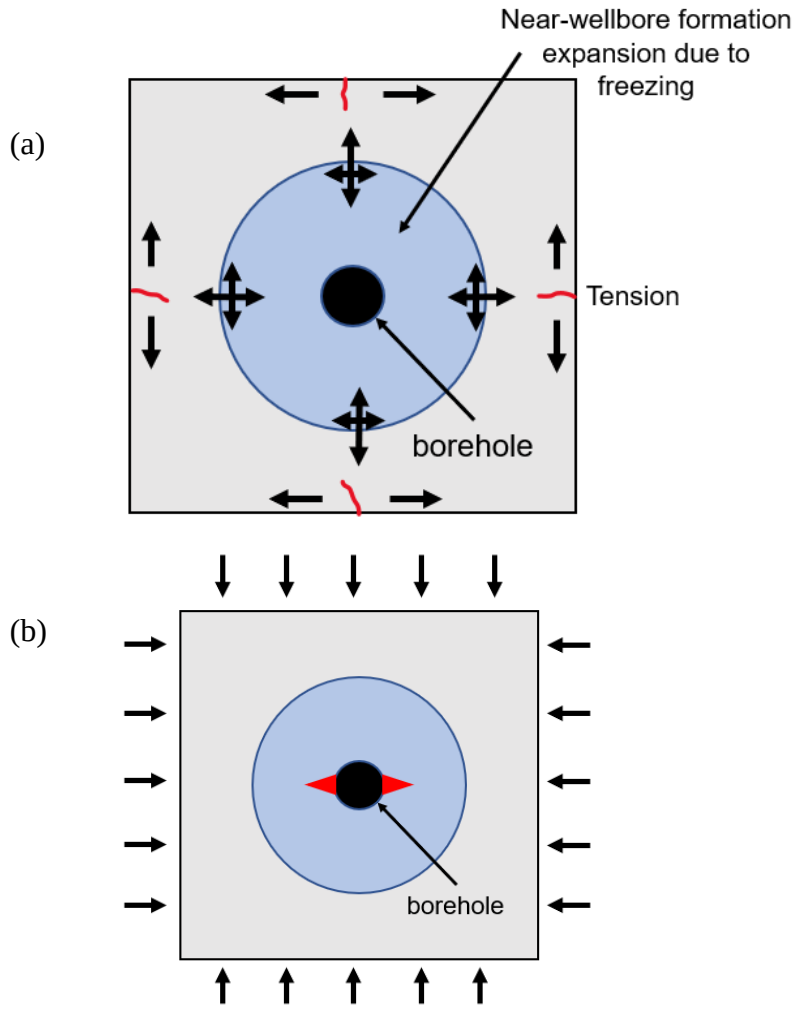

Figure 70: (a) Tensile fractures (red) created by ice expansion in unconfined specimen (this study) and (b) expected behavior in in-field or triaxial confining stresses.

4.3.2 Unconfined borehole test: Sandstone

With the value of porosity that we calculated, in Table 12, effective thermal properties of the specimen were calculated using the same procedure for concrete in Chapter III. Again, we used the thermal conductivity, specific heat, and linear thermal expansion coefficient of quartz to represent the sandstone grains because Berea Upper Grey is made up of a majority of quartz.

Table 14: Estimated thermal properties of saturated sandstone specimen.

	Effective thermal conductivity [W/(m·K)]	Density [kg/m^3]	Effective c_p [J/(kg·K)]	Effective thermal diffusivity [m^2/s]	Effective α [/K]	$\sigma^{\Delta T}_{max}$ [MPa]
Saturated sandstone (water)	2.47	2182	1563.65	7.3×10^{-7}		
Saturated sandstone (ice)	2.83	2182	1097.18	1.2×10^{-6}	1.7×10^{-5}	39.25

From Table 14, the effective thermal conductivity of ice-saturated sandstone is greater than that of water-saturated sandstone. The effective thermal diffusivity of the ice-saturated sandstone is also greater than the water-saturated sandstone, meaning that temperature will travel faster through a water frozen specimen than through a wet specimen. The maximum thermal stress of the ice-saturated specimen is 39.25 MPa. Since the splitting tensile strength of sandstone, from Table 2, is 4.51, the rock split in half after 50 minutes of LN stimulation.

In this section we will discuss differences found between saturated concrete and sandstone specimens under LN stimulation. The influence of rock damage when water changes to ice is investigated.

The circumferential area around the borehole of the specimen is first exposed to the dramatic drop in temperature; this causes expansion inside the block. Unlike the concrete specimens under stimulation, the sandstone specimen had a higher permeability. The high permeability of the sandstone allowed nitrogen pressure to cause water to flow freely through its pore space to the outside of the specimen. The specimen began to push the water in the saturated specimen out through permeation spots (or “leaking holes”). The permeation through the holes

was homogenous on each Face. It is observed that the temperature of the borehole wall did not drop to -195.6 °C until 20 minutes have passed. The temperature on the outside faces of the sandstone drop quicker than that of the concrete specimens.

Because there is not as large a temperature difference between the inside and the outside of the sandstone as that we saw in the concrete specimens, fractures were not seen forming on the surface during the entire duration of the test. We did not have a value for the tensile strength of the sandstone specimen, however, it is possible it is higher than that of concrete.

From the thermal images we obtained of Face 3 throughout the test, the center of the face began to drop in temperature first (Figure 71). This makes sense, as the center of the face is closer in proximity to the borehole than the edges. These images also reveal that temperature propagated through the sandstone specimen much faster than it did in the concrete specimens. Again, this is due to the high permeability of the sandstone allowing nitrogen pressure to easily push pore water to the outside surfaces. The fast propagation of temperature supports our hypothesis earlier about the lack of fracture formation due to a smaller temperature difference between the inside and the outside. After 49 minutes, almost the entire specimen has reached the same low temperature. From our observations, at this point a majority of the pore space in the specimen containes ice and the surfaces of the specimen are completely frozen. Nitrogen pressure is not able to push pore water through to the surface and after the test is stopped, the specimen splits in half vertically. It is believed this split was caused by the expansion of the ice matrix in the pore space leading to a volume/strain incompatibility.

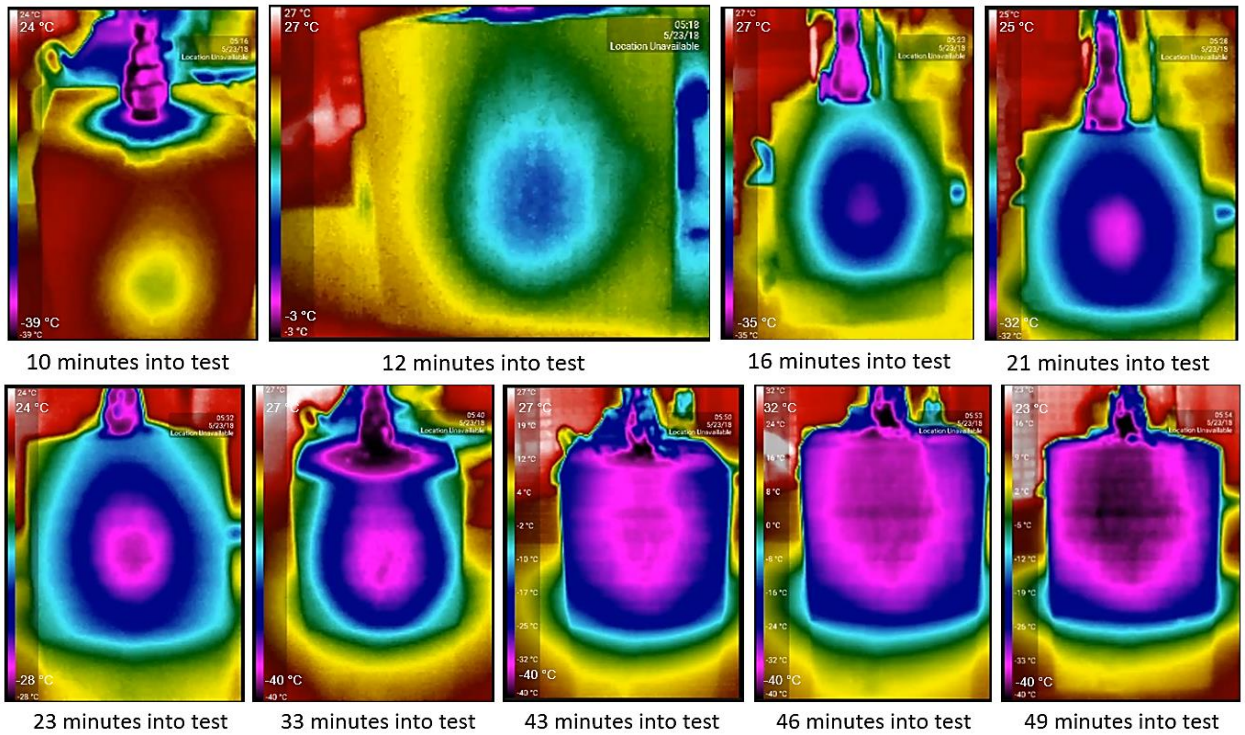

Figure 71: Thermal images of Face 3 of sandstone specimen during LN stimulation.

From the CT images in Figure 64, the fractures on the specimen may have initiated at the surface and then propagated inside. The bottom view of the specimen reveals two fractures: the split fracture and a less visible fracture perpendicular to the split fracture (white arrows on Figure 64). Both extend from the middle of the outside faces to the center of the block, leading us to believe they are tensile fractures resulting from the expansion inside of the specimen.

The presence of water in the specimen created tensile fractures on the outside of the specimen but did not produce any visible micro-fractures near the wellbore. The high permeability of the specimen allowed nitrogen pressure to permeate and push pore water into the formation which led to quicker cooling throughout the specimen. Nevertheless, the circumferential area surrounding the borehole experienced expansion before the outside, which resulted in tensile fractures forming from outside and splitting the rock. More tests will need to be done to investigate

the effects of water in rock formation on unconfined borehole tests subjected to supercooled temperatures with liquid nitrogen.

4.4 Conclusions

Liquid nitrogen fracturing was investigated as a well stimulation approach. We designed experimental setups and procedures for cryogenic thermal shock in unconfined borehole specimens. Fracture assessments were made by visual inspection, X-ray CT, thermal imaging, and acoustic signatures. The amplitudes and velocities of acoustic waves were sensitive to rock properties and cracks, and thus were able to identify rock damages that were not visible. CT images identified spatial distribution of major cracks and allowed us to identify fracture patterns inside the specimens. Temperature data in the borehole and on the surface monitored the state of the nitrogen and evaluate the efficiency of the heat transfer process during submersion.

4.4.1 Unconfined borehole tests: concrete

Experiments were performed to study the development and fractures generated by a cryogenic thermal shock in an unconfined borehole. A distinct pattern in the fracture development was observed in the concrete specimens. Large tensile fractures would extend from the top to the bottom of the specimen on 1-2 of its side faces. This was due to ice expansion in the center of the saturated blocks causing large tensile stress on the outside of the specimen. After one or two of the faces grew fractures, and they grew larger, the number of fractures created after these growth events tended to decrease. This may be because the first large fractures to form release enough tension to stop prevent further fracturing. Further studies should be done to investigate the effect of this phenomenon on cryogenic fracturing patterns in unconfined borehole tests.

Faces with the large tensile fractures propagated temperature quicker than faces without. The circumferential area surrounding the borehole did not experience any fracturing. The freezing of water surrounding the borehole played a competing role with contraction of the rock, and it also created a barrier for nitrogen pressure through the block. Thus, the fractures only occurred on the outside surface of the specimen. In downhole wellbore conditions in the field, this would create large compressive stress in the wellbore that may lead to breakouts. Confined borehole tests at wellbore conditions under true-triaxial loading should be performed to better understand the effects of water on cryogenic fracturing in the field.

4.4.2 Unconfined borehole tests: sandstone

For the sandstone block, no visible fractures were detected during the entirety of the unconfined borehole LN flow test. Due to its high porosity and permeability, the nitrogen pressure permeated through the specimen and pushed the pore water to the outside of the specimen. This led to a low temperature gradient inside the specimen, as seen in the time-lapse of the thermal images.

Once the whole specimen was covered in ice it split in half. This may be due to ice formation reaching its maximum in the sandstone's pore space and causing a volume/strain incompatibility. Unfortunately, in this test we had stopped LN injection and the data logger for the temperature and pressure measurements before the specimen split. More tests should be done to investigate if this splitting would occur again if the test had lasted a few minutes longer.

Several other topics that require further studies have been identified in this laboratory study. The effects of the sandstone material properties on cryogenic fracturing behavior, particularly with water, should be investigated. Unconfined borehole tests in sandstone specimens

of lower porosity, and the added effect of stress level and stress anisotropy on the characteristics of cryogenic fracturing can be investigated by using a triaxial loading system.

CHAPTER V

CONCLUSIONS

The presence of pore water in formations complicates the behaviors of cryogenic fracturing because freezing pore water will expand and possibly compete with contracting mineral solids. In previous studies, it was hypothesized that the presence of water will weaken the driving force of cryogenically induced tensile fractures. This thesis reports a laboratory study of cryogenic fracturing to investigate the effects of formation water on cryogenic fracturing patterns. We designed experimental setups and procedures for cryogenic stimulations for submersion tests and unconfined borehole tests. The ability of liquid nitrogen to create fractures in saturated specimens was tested, and fracture assessments were made by visual inspection, X-ray CT, thermal imaging, and acoustic signatures. Temperature data in all experiments allowed us to assess the efficiency of the heat transfer process. The pressure data in Chapter IV for liquid nitrogen flow through unconfined borehole tests also allowed us to monitor the state of the stimulating fluid.

5.1 Submersion of cores

The cryogenic stimulations conducted in our experiments with saturated specimens were able to create cracks in the rock and alter rock properties. Fractures were created by generating a strong thermal gradient by submerging sandstone and shale cores into LN until approximate thermal equilibrium was reached. The saturated sandstone core specimens had more cracks than the dry core specimens, due to ice expansion. The same was observed for the saturated shale core specimens vs. the dry shale specimens. Further, the higher porosity sandstone cores had more fracture growth than the low porosity cores. The higher pore space of the Bentheimer sandstone allowed for more ice expansion and creates fractures in the mineral skeleton. However, acoustic

signatures and an increase in permeability after submersion revealed that the saturated lower porosity, Colton, sandstone did experience some invisible micro-fracturing. Micro-CT images did not reveal internal fractures in the Colton sandstone, but changes in velocities and amplitudes of acoustic waves were able to detect changes in rock properties that were not visible.

5.2 Submersion of concrete specimens

Submersion of dry and saturated concrete specimens revealed that the saturated blocks underwent more surface fracturing than the dry. While the dry specimens experienced none or few tensile fractures, the saturated specimens generated large tensile and shear fractures in different experiments. The saturated specimens also generated smaller fractures that formed a polygon network on the surface. Only the large tensile and shear fractures were observed in the CT images to penetrate through the surface, however no fractures reached the center of the block.

5.3 Unconfined borehole tests in concrete and sandstone

The thermal shock in the concrete blocks with boreholes generated visible fractures, the signatures of which were easily picked up by acoustic measurements. The pore space around the concrete borehole became frozen with ice and inhibited nitrogen pressure permeation throughout the specimen. As the circumferential area around the borehole experienced ice expansion, tensile stress was built up on the outer surface of the block. Due to this, all fractures in the concrete specimens were created on the outside of the specimen. This fracture pattern and the barrier to nitrogen pressure permeation around the borehole is counterintuitive to the practice of cryogenic fracturing. Nevertheless, it is important to remember that concrete and natural rocks are different in their physical and thermal properties.

The saturated sandstone block, after 50 minutes of liquid nitrogen treatment to produce thermal shock, had no visible fractures. After the LN supply was turned off, the specimen immediately invsplit in half. The formation of ice throughout the highly porous sandstone caused the specimen to experience a volume/strain incompatibility. Once the specimen's pore space was fully filled with ice, the mineral matrix could not continue to expand without experiencing large tensile strain and splitting in half.

From the saturated unconfined borehole tests, it is clear that the generation and geometry of fractures is highly dependent on material properties. For example, nitrogen pressure is inhibited in low permeability specimens (concrete) but flows freely through high permeability specimens such as sandstone, which can reduce the effects of thermal shock.

5.4 Field implications

The effect of water in formations can have implications in the effectiveness of cryogenic fracturing for enhanced oil recovery techniques. If cryogenic fracturing is performed at formations that are water saturated, or at formations that have been exposed to previous drilling and completion fluids, the integrity of the cracks will be questioned. From our experiments, we have found that natural rocks exposed to LN that contain fluid in its pores become frozen and the mineral skeleton expands, damaging the pore structure. From our shale submersion tests, we can conclude that the damage of the pore structure can enhance permeability of the specimens. The ability of the dry and saturated shale specimens to generate cracks along the bedding planes and perpendicular to the bedding plane leads us to believe cryogenic fracturing in shale reservoirs would be an effective practice for a waterless enhanced oil recovery technique. However, this test was not performed with downhole conditions. Further investigations in the laboratory, such as cryogenic fracturing at

reservoir stress levels by thermal shock using a triaxial loading system, will need to be done to test the validity of cryogenic fracturing with LN in shale reservoirs.

Field experiments of cryogenic fracturing by McDaniel et al. 1997 and Grundmann et al. 1998 were performed in wells with steel-cased boreholes. Although the wells were cased, there were perforations throughout the borehole to prevent wellbore failure. Performing cryogenic fracturing in wellbores without casing may enhance the fracturing potential of the technology. Field studies will have to be done to test this theory.

It should also be noted that no propping agents were used in our laboratory experiments. As a result, fractures began to close when the specimens returned to room temperature. This may be something to consider in future investigations for cryogenic fracturing.

5.5 Future work

Several other topics that require further studies have been identified in this laboratory study. In the future, permeability enhancement assessed by comparing pressure decay tests before and after cryogenic stimulation of saturated specimens would be useful data to investigate. Also, the effects of the sandstone material properties on cryogenic fracturing behavior, particularly with water, should be further investigated (as we were only able to test one). Unconfined borehole tests in saturated sandstone specimens of lower porosity would be beneficial to consider the effects of various material properties on the characteristics of cryogenic fracturing. Finally, the added effect of stress level and stress anisotropy on the characteristics of cryogenic fracturing in saturated specimens should be investigated by using a triaxial loading system. This way cryogenic fracturing at reservoir stress levels by thermal shock can be investigated.

REFERENCES

Al-Yaseri, A. Z., et al. (2015). "Pore-scale analysis of formation damage in Bentheimer sandstone with in-situ NMR and micro-computed tomography experiments." Journal of Petroleum Science and Engineering **129**: 48-57.

Alqahtani, N. B. (2015). Experimental Study and Finite Element Modeling of Cryogenic Fracturing in Unconventional Reservoirs. Department of Petroleum Engineering, Colorado School of Mines. **PhD**.

Alqatahni, N. B., et al. (2016). Experimental Investigation of Cryogenic Fracturing of Rock Specimens Under True Triaxial Confining Stresses. SPE Europec featured at 78th EAGE Conference and Exhibition. Vienna, Austria, Society of Petroleum Engineers.

Cai, C., et al. (2014). "Experimental study of the effect of liquid nitrogen cooling on rock pore structure." Journal of Natural Gas Science and Engineering **21**: 507-517.

Cha, M., et al. (2016). "Studying Cryogenic fracturing process using transparent specimens." The 1st International Conference on Energy Geotechnics: 211-216.

Cha, M., et al. (2018). "Cryogenic Fracturing of Wellbores Under True Triaxial-Confining Stresses: Experimental Investigation."

Cha, M., et al. (2017). "Laboratory system for studying cryogenic thermal rock fracturing for well stimulation." Journal of Petroleum Science and Engineering **156**: 780-789.

Cha, M., et al. (2009). "Long-wavelength P-wave and S-wave propagation in jointed rock masses." Geophysics **74**(5): E205-E214.

Cha, M., et al. (2014). "Cryogenic fracturing for reservoir stimulation – Laboratory studies." Journal of Petroleum Science and Engineering **124**: 436-450.

Chen, T. C., et al. (2004). "Effect of water saturation on deterioration of welded tuff due to freeze-thaw action." Cold Regions Science and Technology **38**(2-3): 127-136.

Dahmani, L., et al. (2007). "Behavior of the reinforced concrete at cryogenic temperatures." Cryogenics **47**(9): 517-525.

Dickinson, W., et al. (2012). "Provenance of the Paleogene Colton Formation (Uinta Basin) and Cretaceous–Paleogene provenance evolution in the Utah foreland: Evidence from U-Pb ages of detrital zircons, paleocurrent trends, and sandstone petrofacies." Geosphere **8**(4): 854.

Ewy, R. T. (2015). "Shale/claystone response to air and liquid exposure, and implications for handling, sampling and testing." International Journal of Rock Mechanics and Mining Sciences **80**: 388-401.

Ferrari, A., et al. (2014). "Experimental analysis of the water retention behaviour of shales." International Journal of Rock Mechanics and Mining Sciences **72**: 61-70.

FHWA, U. (2011). Portland Cement Concrete Pavements Research, Report of the US Department of Transportation Federal Highway Administration.

Grundmann, S., et al. (1998). "Cryogenic nitrogen as a hydraulic fracturing fluid in the Devonian Shale " Society of Petroleum Engineers.

Kalteyer, R. (2017). Nanopetrophysics Characterization of the Mancos Shale Formation in the San Juan Basin of Northwestern New Mexico, U.S.A. Faculty of the Graduate School of The University of Texas at Arlington, University of Texas at Arlington. **Master of Science:** 115.

Kneafsey, T. J., et al. (2011). "Examination of core samples from the Mount Elbert Gas Hydrate Stratigraphic Test Well, Alaska North Slope: Effects of retrieval and preservation." Marine and Petroleum Geology **28**(2): 381-393.

Kogbara, R. B., et al. (2013). "A review of concrete properties at cryogenic temperatures: Towards direct LNG containment." Construction and Building Materials **47**: 760-770.

Kogbara, R. B., et al. (2014). "Relating damage evolution of concrete cooled to cryogenic temperatures to permeability." Cryogenics **64**: 21-28.

Kondash, A. and A. Vengosh (2015). "Water Footprint of Hydraulic Fracturing." Environmental Science & Technology Letters **2**(10): 276-280.

Krstulovic-Opara, N. (2007). "Liquefied Natural Gas Storage: Material Behavior of Concrete at Cryogenic Temperatures." ACI Materials Journal **104**(3): 297-306.

Landis, E. N. and D. T. Keane (2010). "X-ray microtomography." Materials Characterization **61**(12): 1305-1316.

Levinthal, J. D. (2016). Mineralogical and Chemical Composition of Shale at Multiple Scales. Department of Civil and Environmental Engineering, The University of Utah. **M.S.**

Li, Z., et al. (2016). "Liquid nitrogen gasification fracturing technology for shale gas development." Journal of Petroleum Science and Engineering **138**: 253-256.

Liu, Z. and J. Zhao (2015). "An Experimental Study of Velocity-Saturation Relationships in Volcanic Rocks." The Open Petroleum Engineering Journal **11**(8): 142-152.

Mallamace, F., et al. (2007). "The anomalous behavior of the density of water in the range 30 K < T < 373 K." Proc Natl Acad Sci U S A **104**(47): 18387-18391.

Marshall, A. L. (1982). "Cryogenic concrete." Cryogenics **22**(11): 555-565.

McDaniel, B. W., et al. (1997). "Field applications of cryogenic nitrogen as a hydraulic fracturing fluid " Society of Petroleum Engineers.

Montgomery, C. (2013). "Fracturing Fluids."

Mrdjen, I. and J. Lee (2016). "High volume hydraulic fracturing operations: potential impacts on surface water and human health." Int J Environ Health Res **26**(4): 361-380.

Norris, J. Q., et al. (2016). "Fracking in Tight Shales: What Is It, What Does It Accomplish, and What Are Its Consequences?" Annual Review of Earth and Planetary Sciences **44**(1): 321-351.

Rempel, A. W. (2007). "Formation of ice lenses and frost heave." Journal of Geophysical Research **112**(F2).

Rostásy, F. S., et al. (1979). "Behaviour of mortar and concrete at extremely low temperatures." Cement and Concrete Research **9**(3): 365-376.

Saruya, T., et al. (2014). "Hydrodynamic transitions with changing particle size that control ice lens growth." J Phys Chem B **118**(47): 13420-13426.

Thomas, H. R., et al. (2009). "Modelling of cryogenic processes in permafrost and seasonally frozen soils." Géotechnique **59**(3): 173-184.

Wang, L., et al. (2016). "Waterless fracturing technologies for unconventional reservoirs-opportunities for liquid nitrogen." Journal of Natural Gas Science and Engineering **35**: 160-174.

Yang, G. S., et al. (2004). Study on the damage propagation characteristics of rock under the frost and thaw condition.

Zhang, D., et al. (2017). "Influence of Water Saturation on the Mechanical Behaviour of Low-Permeability Reservoir Rocks." Energies **10**(2): 236.